THE JOURNAL OF ACOUSTICAL SOCIETY OF INDIA

The Journal of Acoustical Society of India

The Refereed Journal of the Acoustical Society of India (JASI)

The Journal of Acoustical Society of India is a refereed journal of the Acoustical Society of India **(ASI)**. The **ASI** is a non-profit national society founded in 31st July, 1971. The primary objective of the society is to advance the science of acoustics by creating an organization that is responsive to the needs of scientists and engineers concerned with acoustics problems all around the world.

Manuscripts of articles, technical notes and letter to the editor should be submitted to the Chief Editor. Copies of articles on specific topics listed above should also be submitted to the respective Associate Scientific Editor. Manuscripts are refereed by at least two referees and are reviewed by Publication Committee (all editors) before acceptance. On acceptance, revised articles with the text and figures scanned as separate files on a diskette should be submitted to the Editor by express mail. Manuscripts of articles must be prepared in strict accordance with the author instructions.

All information concerning subscription, new books, journals, conferences, etc. should be submitted to Chief Editor:

B. Chakraborty, CSIR - National Institute of Oceanography, Dona Paula, Goa-403 004,
Tel: +91.832.2450.318, Fax: +91.832.2450.602, e-mail: bishwajit@nio.org

Annual subscription price including mail postage is Rs. 2500/= for institutions, companies and libraries and Rs. 2500/= for individuals who are not **ASI** members. The Journal of Acoustical Society of India will be sent to **ASI** members free of any extra charge. Requests for specimen copies and claims for missing issues as well as address changes should be sent to the Editorial Office:

ASI Secretariat, C/o Acoustics, Ultrasonics & Vibration Section, CSIR-National Physical Laboratory, Dr. KS Krishnan Road, New Delhi 110 012, Tel: +91.11.4560.8317, Fax: +91.11.4560.9310, e-mail: asisecretariat.india@gmail.com

The Journal of Acoustical Society of India

A quarterly publication of the Acoustical Society of India

Volume 45, Number 1, January 2018

ARTICLES

INFORMATION

Acoustic source localization accuracy using network of sonobuoys of omni-directional hydrophones and acoustic vector sensors

Bipin Kumar, Arun Kumar and Rajendar Bahl
Centre for Applied Research in Electronics
Indian Institute of Technology, Delhi-110016, India
crz148292@iitd.ac.in

ABSTRACT

We have done simulation studies to compare the localization accuracy of an underwater radiating acoustic source using omni-directional hydrophone based sonobuoys and acoustic vector sensor(AVS) based sonobuoys, without and with an interference source for the same number of sonobuoys of either type. We use Time Difference of Arrival (TDOA) method for hydrophone sonobuoys and Direction of Arrival (DOA) based method for AVS sonobuoys to localize the target. The analysis is shown for isotropic colored Gaussian noise for sea-state3. The performance has been evaluated in terms of Root Mean Square Error. We have done the simulation study for sonobuoy placement in circular and L-shape geometries, by varying the inter-element spacing and SNR of the target. Also, the effects of placing the sonobuoys close or far apart and influence of interference sources on localization accuracy are studied and inferences are drawn. It is shown that the AVS based sonobuoys offer advantages in terms of improved localization accuracy compared to omni-directional hydrophone based sonobuoys.

1. INTRODUCTION

An Acoustic Vector Sensor (AVS) is a sensor that measures acoustic pressure as well as the components of acoustic particle velocity at a collocated point. An AVS, in most general form, comprises of three orthogonally oriented particle velocity sensors and an optional hydrophone, all spatially collocated in a point like geometry. Each velocity sensor has an intrinsic directional response to the incident sound field. A single point measurement using a conventional hydrophone yields only the scalar information on the sound field, viz. the pressure amplitude. On the other hand, the particle velocity measurements in an AVS provide additional information about the acoustic field, which is not available in the case of a single hydrophone. This gives the AVS many advantages over hydrophones such as compactness, better and unambiguous localization for underwater acoustic sensing applications and flexibility of sensor spacing [1].

Acoustic source localization is done mainly by using DOA, Time of Arrival (TOA), Intensity or Time Difference of Arrival (TDOA) information. Using DOA, we can localize the target by taking each DOA obtained from sensors, and drawing a line of bearing (LOB) [2] from the source to the receiver. The intersection of at least two LOBs will give the source location. This scheme does not require clock synchronization. Intensity-based [3, 4] source localization is motivated by a simple observation that the

sound level decreases when the distance between the sound source and the listener increases. By modeling the relation between sound level (energy) and distance from the sound source, one may estimate the source location using multiple energy readings at different known sensor locations. An implicit advantage of this method is its simplicity: only acoustic energy measured during a specific period is needed. However, this simplicity also implies many practical difficulties that need to be mitigated. In particular, the sensor gain calibration and SNR estimation are two key factors that affect the accuracy of this method. TOA based position estimation is a method which uses time information i.e., the time required for a source signal to the sensors [5]-[7]. Here, multiple spatially separated sensors localize a source by the method of triangulation [8]. The three-dimensional position of a source can be estimated by using three spheres, and each measurement corresponds to the equation of a sphere. The position is estimated by the intersection of these three spheres using TOA measurements [5]-[7]. But in general, direct TOA results in two problems. First, TOA requires that all sources and sensors in the system have precisely synchronized clocks [7]. Second, the source signal must be labeled with a timestamp to allow the sensor to determine the time at which the signal was initiated from the source [7]. This additional time stamp either increases the complexity of the source signal or may not be present in practical scenarios, and may lead to an additional source of error. By using hydrophones we can localize the source by the TDOA based on the intersection of hyperbolic curves [9,10,11]. In TDOA based estimation, a number of spatially separated hydrophones receive the signal transmitted by the source, which needs to be localized.

This paper presents various simulation studies on localization accuracy comparison using AVS and hydrophone based sonobuoys deployed in equal numbers. Section 2 of the paper presents the signal propagation model, section 3 of the paper discusses the methodology used in the determination of position using AVS and hydrophone based sonobuoys. Section 4 discusses the simulation setup and presents the results of various simulation experiments done in the respective sub-sections. Section 5 concludes the study with a summary of the comparison study between hydrophone and AVS based sonobuoys.

2. SIGNAL PROPOGATION MODEL

Let $s(t)$ be the signal and SL be the power of signal in $dBre1\mu Pa$ radiated by the target. PR is the power received in $dBre1\mu Pa$. Also, the power received in Watts is denoted by P_R after including Transmission Loss (TL) at a distance of r m from the source is obtained assuming spherical spreading. The power received is given as:

$$PR = SL - TL$$
$$PR = 171.5 + 20 \log P_R$$
$$PR = 10^{\frac{PR-1715}{20}} W$$

(1)

The radiated signal is assumed to be of low frequency so we have not considered absorption loss which is negligible as compared to geometrical spreading loss. The signal received at the ith sensor can thus be expressed as,

$$u_i(t) = \sqrt{(P_R)} * s(t) + n_i(t)$$

(2)

Where $n_i(t) \sim N(0, \sigma_i)$ is colored Gaussian noise.

3. METHODOLOGY

In this section, we present the method to find the TDOA and DOA and using them to localize the target.

3.1. Localization by using Time Difference of Arrival (TDOA)

Source localization using TDOA is a two-step process. First, we determine the TDOA of the target between pairs of hydrophones, and then using the TDOA information we localize the target. The sub-section below describes the two-step process.

3.1.1. TDOA estimation using GCC-PHAT

Knapp and Carter [11] provide a description of generalized cross-correlation (GCC) based TDOA estimation method. In particular, the GCC-Phase Transform (GCC-PHAT) method of TDOA does not suffer the spreading of correlation function that other estimation techniques do and hence can provide good performance under reasonable noise conditions. The required mathematical formulation for the GCC-PHAT technique is presented below.

Consider a signal $s_1(t)$ emanating from a source, received under noise at two spatially separated hydrophones as,

$$u_i(t) = s_1(t) + n_1(t)$$
$$u_2(t) = as_1(t+D) + n_2(t)$$

(3)

Where $s_1(t)$, $n_1(t)$ and $n_2(t)$ are real, jointly stationary random processes, and α is a scaling constant. The signal $s_1(t)$ is assumed to be uncorrelated with noise $n_1(t)$ and $n_2(t)$. Our aim is to estimate the TDOA between the two signals, D. One common method of determining the time delay D is to compute the cross-correlation (CC) function as,

$$R_{u_1 u_2}(\tau) = E(u_1(t)u_2(t-\tau)]$$

(4)

Where $E[.]$ stands for expectation operator. The argument τ that maximizes (4) provides an estimate of the delay D. In case of low SNR at the receiver this method fails to estimate the accurate time delay D due to the presence of multiple peaks. GCC is a generalized form of cross-correlation which has received considerable attention due to its ability to avoid spreading of the correlation peak. GCC-PHAT can be mathematically expressed as:

$$GPHAT = \frac{G_{u_1 u_2}(f)}{|G_{u_1 u_2}(f)|} = e^{j\theta(f)} = e^{j2\pi fD}$$

(5)

Where $G_{u1u2}(f)$ is the cross power spectral density of u_1 and u_2. Taking the inverse transform of the above equation,

$$R_{y_1 y_2}^{(p)}(\tau) = \delta(t - D) = F^{-1}(GPHAT)$$

(6)

Once the TDOAs are estimated, the next step is to estimate the position of the source using the TDOAs. In the subsequent section, we describe a non-iterative approach to estimate the position of a source using TDOAs [12].

3.1.2. Position estimation using TDOA

In this sub-section, we explain the technique used for estimating the source position using TDOAs [12]. Assume there are M sensors distributed arbitrarily in a 2D-plane as shown in fig.1.
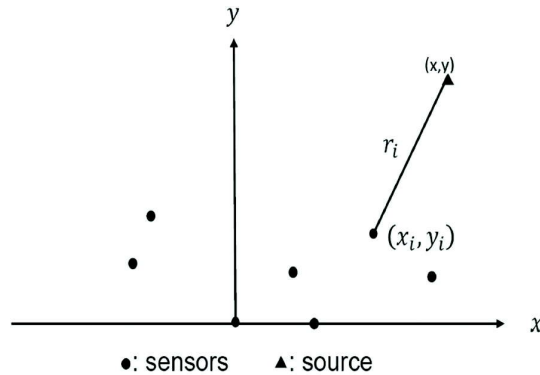

Fig. 1. Localization in 2-D plane.

Now consider the signal $u_i(t)$ received from the source at the ith hydrophone,

$$u_i(t) = s(t - t_i) + n_i(t), \ i = 1, 2, ..., M \tag{7}$$

where, $s(t)$ is the signal radiating from the source, t_i is the time delay associated with receiver i and $n_i(t)$ is the additive noise at receiver i. The signal and noise are assumed to be mutually independent, zero mean stationary random processes. In order to localize the source, first estimate the TDOA of the signal received at hydrophones i and j using GCC-PHAT. We estimate the TDOA of the signals received at all the sensors with respect to the first sensor $i.e.$, at $i = 1$. TDOAs with respect to the first sensor can be written as,

$$t_{i,1} = t_i - t_1, \ i = 2, 3, ..., M \tag{8}$$

Let $t_d = [t_{2,1}, t_{3,1}, ..., t_{M,1}]^T$ be the estimated TDOA vector. As shown in fig. 1, the unknown source position is (x, y) and the known sensor positions are (x_i, y_i). The squared distance between the source and sensor i is

$$r_i^2 = (x_i - x)^2 + (y_i - y)^2$$
$$K_i - 2x_i x - 2y_i y + x^2 + y^2, \ i = 1, 2, ..., M \tag{9}$$

where, $K_i = x_i^2 + y_i^2$. If   is the propagation speed of the signal, then,

$$r_{i,1} = c t_{i,1} = r_i - r_1, \ i = 1, ..., M \tag{10}$$

define a set of nonlinear simultaneous equations whose solution gives (x, y). First, transform these equations into another set of equations. From (10), $r_i^2 = (r_{i,1} + r_1)^2$ so that (9) can be rewritten as,

$$r_{i,1}^2 + 2r_{i,1} r_1 + r_1^2 = K_i - 2x_i x - 2y_i y + x^2 + y^2 \tag{11}$$

Subtracting (9) at $i = 1$ from (11), we obtain

$$r_{i,1}^2 + 2r_{i,1} = -2x_{i,1} x - 2y_{i,1} y + K_i - K_1 \tag{12}$$

where the symbols $x_{i,1}$ and $y_{i,1}$ stand for $x_i - x_1$ and $y_i - y_1$ respectively. It is important to note that the set of equations in (12) is still a nonlinear set of simultaneous equations with unknowns x, y and r_1. To solve for x, y, eliminate r_1 from (14) and produce (M-2) linear equations in x and y. The source position is then estimated using least squares (LS).

Now, we describe a technique proposed in [12] to solve these equations when the number of sensors $M \geq 4$. In this particular case, the system of equations is over-determined as the number of measurements are greater than the number of unknowns. Let $z_a = [z_p^T, r_1]^T$ be the unknown vector, where $z_p = [x, y]^T$. Usually, in the presence of noise, the set of nonlinear equations in (14) will not meet at the same point. Thus, the error vector derived from (14) is,

$$\Psi = h - G_a z_a^0 \tag{13}$$

where

$$h = \frac{1}{2} \begin{bmatrix} r_{2,1}^2 & - K_2 & + K_1 \\ r_{3,1}^2 & - K_2 & + K_1 \\ & ... & \\ r_{M,1}^2 & - K_M & + K_1 \end{bmatrix}$$

$$G_a = - \begin{bmatrix} x_{2,1} & y_{2,1} & r_{2,1} \\ x_{3,1} & y_{3,1} & r_{3,1} \\ . & . & . \\ x_{M,1} & y_{M,1} & r_{M,1} \end{bmatrix} \tag{14}$$

As in presence of noise, there will be an error in TDOAs *i.e.* $t_{i,1} = t_{i,1}^0 + n_{i,1}$, where $n_{i,1}$ is the error in TDOA, and $\{*\}^0$ denotes the noise free value of $\{*\}$. Then, (10) can be used to express the estimated range as,

$$r_{i,1} = r_{i,1}^0 + cn_{i,1} \tag{15}$$

Noting from (10) that $r_i^0 = r_{i,1}^0 + r_1^0$, ψ is found to be

$$\psi = cBn + 0.5c^2 n \odot n$$
$$B = diag\left\{r_2^0, r_3^0, ..., r_M^0\right\} \tag{16}$$

where $\odot$ represents the Schur product (element-by-element product). In practice, the condition $cn_{i,1} << r_1^0$ is usually satisfied. Ignoring the second term on the right of (13), ψ becomes a Gaussian random vector with covariance matrix given by,

$$\psi = E[\psi\psi^T] = c^2 BQB \tag{17}$$

The elements of z_a in (13) are related through $K_i = x_i^2 + y_i^2$, which means that (13) is still a set of nonlinear simultaneous equations in two variables *x* and *y*. The approach to solve this problem is to first assume that there is no relationship among *x, y* and r_1. They can then be solved by the (LS) method. The final solution is obtained by imposing the known relationship $K_i = x_i^2 + y_i^2$ to the computed result via another LS computation. This two-step procedure is an approximation of a true ML estimator for source location. By considering the elements of z_a to be independent, the ML estimate of z_a can be obtained as,

$$z_a = \arg\min\{(h - G_a z_a)^T \psi^{-1}(h - G_a z_a)\}$$
$$= (G_a^T \psi^{-1} Ga)^{-1} G_a^T \psi^{-1} h \tag{18}$$

This is readily recognized as the generalized LS solution of (13). The covariance matrix ψ is not known in practice, as the matrix *B* contains the true distances between source and sensors. Thus, further approximation is necessary in order to make the problem solvable. When the source is far from the array, each r_i^0 is close to r^0 so that $B \approx r^0 I$, where r^0 designates the range and *I* is an identity matrix of size *M*–1. Since, scaling ψ does not affect the answer, an approximation of (18) is,

$$z_a \approx (G_a^T Q^{-1} G_a)^{-1} G_a^T Q^{-1} h \tag{19}$$

If on the other hand source is close, we can first use (19) to obtain an initial solution to estimate *B*. The final answer is then computed using (18). However, (18) can be iterated to provide an even better answer.

3.2. Localization using Direction of Arrival

Localization using DOA is a two-step process. First we determine the DOA of the target and then using DOA information we localize the target. In the sub-section below, we describe the two-step process one by one.

3.2.1. DOA Estimation using Arc Tangent

Let the signal intercepted by the omnidirectional sensors be $u_0(t)$ and the components of the received signal received by two orthogonally placed directional sensors be designated as $u_s(t)$ and $u_c(t)$ where, the subscripts *o, s* and *c*, represent the omni, cosine and sine components respectively[13,14].

$$\begin{bmatrix} u_0(t) \\ u_c(t) \\ u_s(t) \end{bmatrix} = \begin{bmatrix} 1 \\ \cos(\theta) \\ \sin(\theta) \end{bmatrix} * s(t) + \begin{bmatrix} n_0(t) \\ n_c(t) \\ n_s(t) \end{bmatrix} \tag{20}$$

where *s(t)* in (20) is the radiated signal, θ is the incidence angle and $n_0(t)$, $n_s(t)$, $n_c(t)$ are zero mean colored Gaussian noise. Taking the Fourier transform of the above equation,

$$\begin{bmatrix} u_0 \\ u_c \\ u_s \end{bmatrix} = \begin{bmatrix} 1 \\ \cos(\theta) \\ \sin(\theta) \end{bmatrix} * S + \begin{bmatrix} N_0 \\ N_c \\ N_s \end{bmatrix} \tag{21}$$

The bearing estimate $\hat{\theta}$ is expressed as:

$$\hat{\theta} = arctan\left(\frac{\hat{s}}{\hat{c}}\right) \tag{22}$$

where $\hat{S}$ and $\hat{C}$ are defined as

$$\hat{S} = \text{Re}(U_s * U_0^*)$$
$$\hat{C} = \text{Re}(U_c * U_0^*) \tag{23}$$

3.2.2. Position estimation using DOA

A grid-based (GB) method is analyzed as given in [15,16], to solve the single source localization problem. This method is an alternative formulation of the non-linear LS (NLS) estimator, which tries to alleviate the major weaknesses of that approach, namely the need for a good initial point to ensure the estimator does not converge to any local minimum, and the computational burden of the minimization procedure. Our approach is based on making the search space discrete by constructing a grid of N points over the area of interest, and then finding the grid point whose DOAs most closely match the estimated DOA. This approach is much more computationally efficient without losing any accuracy, particularly in the multiple source case. A matrix of MxN is formed as follows,

$$\psi = \begin{bmatrix} \psi_{1,1} & \psi_{1,2} & \cdots & \psi_{1,n} & \psi_{1,N} \\ \psi_{2,1} & \psi_{2,2} & \cdots & \psi_{2,n} & \psi_{2,N} \\ \vdots & \vdots & \cdots & \vdots & \vdots \\ \psi_{1,1} & \psi_{1,2} & \cdots & \psi_{1,n} & \psi_{1,N} \\ \vdots & \vdots & \cdots & \vdots & \vdots \\ \psi_{M,1} & \psi_{M,2} & \cdots & \psi_{M,n} & \psi_{M,N} \end{bmatrix} \tag{24}$$

Where $\psi_{m,n}$ in (24) is the DOA from the mth sensor to the nth grid point. The nth column of ψ is formed from the M DOAs to the nth grid point. The index of the grid point whose DOAs best match the estimated DOAs is evaluated as

$$n^* = argmin_n \sum_{n=1}^{N} \left| A(\hat{\theta}_n, \psi_{m,n}) \right|^2) \tag{25}$$

Where $A(X, Y)$ is the angular distance function defined in [14]. The source position is given as the coordinates of then* grid point.
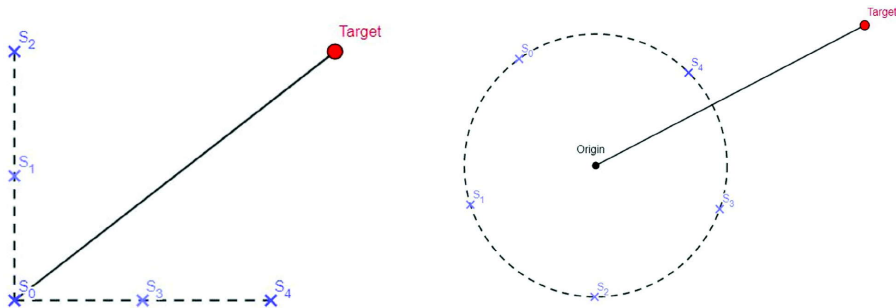
Fig. 2. Sonobuoy placement in L-shape and circular shape.

4. SIMULATION METHOD

The source and sonobuoy placements are shown in Figure 2. Each sonobuoy is equipped with either an omni-directional hydrophone or an AVS. The sonobuoys are deployed in L-shape or circular geometry in this study. The transmitted signal is taken as a narrowband tonal signal of 1second duration which suffers from transmission loss and addition of colored Gaussian noise. We have done the localization comparison using deployment of sonobuoys of AVSs or hydrophones by using the simulation parameters shown in Table 1.

Table 1. Simulation parameters used

S.No	Simulation parameter	Value/Type
1	Radiated signal power level	170 dBre1microPa
2	Sea-state	3
3	Range	1000 and 2000 (m)
4	Geometry	L and Circular shape
5	No. of Sonobuoys	5, 7
6	Transmitting signal frequency	1000 Hz
7	Sampling frequency	44100 Hz
8	Interference signal frequency	1200 Hz
9	Interference signal power level	140 dBre1microPa
10	Method used for Localization using Hydrophone	TDOA
11	Method used for Localization using AVS	DOA
12	Number of Monte Carlo Simulations	100

5. RESULTS AND DISCUSSION

The comparison of localization accuracy between hydrophone and AVS based sonobuoy deployments have been done in the following sub-sections.

5.1. Varying the distance and direction of radiated source with respect to the origin coordinate of sonobuoys for a single source for circular and L-shape for 5 sonobuoys.

In this sub-section, we study the localization performance in terms of RMSE for hydrophone based sonobuoys and AVS based sonobuoys deployed in either circular or L-shape geometry, for the case of 5 sonobuoys of

Fig. 3. RMSE of location estimation with respect to bearing for range of 1000 and 2000 meters for L-shape using hydrophone or AVS based sonobuoys.

either type. The source range from the origin of the coordinate system as measured from the sonobuoy deployment geometries is varied, as also the direction of the source with respect to the x-axis.

From Figures 3 and 4, we observe that AVS based sonobuoys gives more accurate location estimation of the source as compared to hydrophone based sonobuoys except at few angles for both L shape and circular geometries of deployment. Also, by comparing figures 3 and 4, it is seen that the circular geometry provides significantly larger improvement in localization accuracy as compared to L-shape geometry.
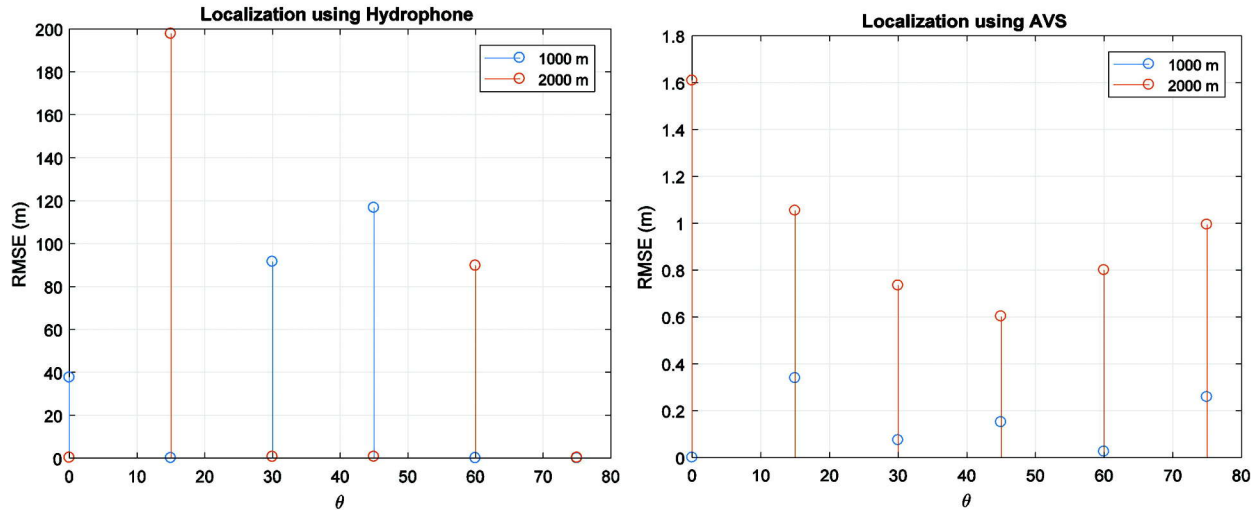
Fig. 4. RMSE of location estimation with respect to bearing angle for range of 1000 and 2000 meters for circular shape geometry using hydrophone or AVS based sonobuoys.

5.2. Varying the distance and direction of radiated source with respect to the origin coordinate of sonobuoys for a single source for circular and L-shape for 7 sonobuoys.

Similar to the observations for 5 sensor geometries in the previous sub-section, it can be observed from Figures 5 and 6, that AVS based sonobuoys gives more accurate location estimation of the source as compared to hydrophone based sonobuoys except at few angles for both L-shape and circular geometries of sonobuoy
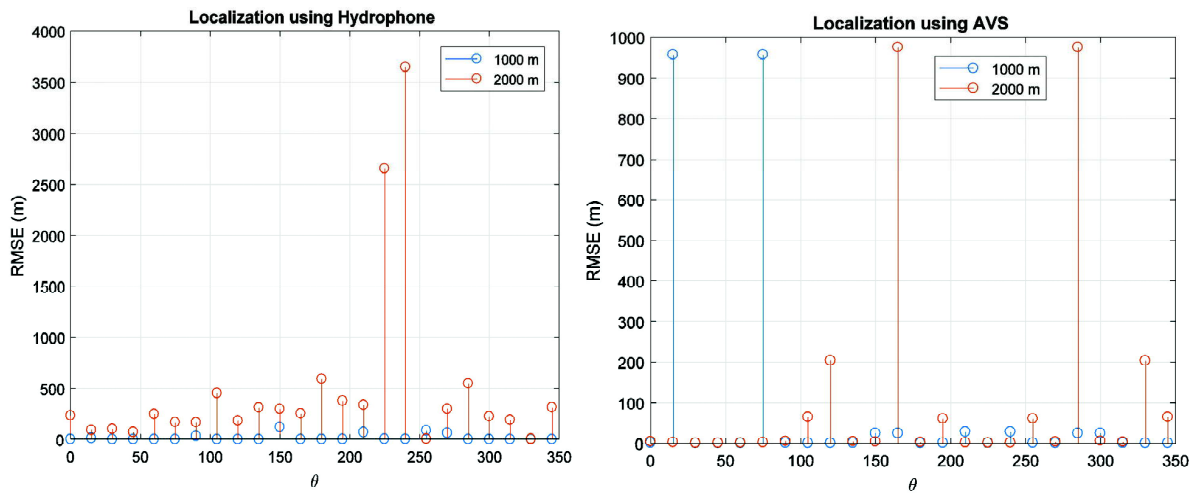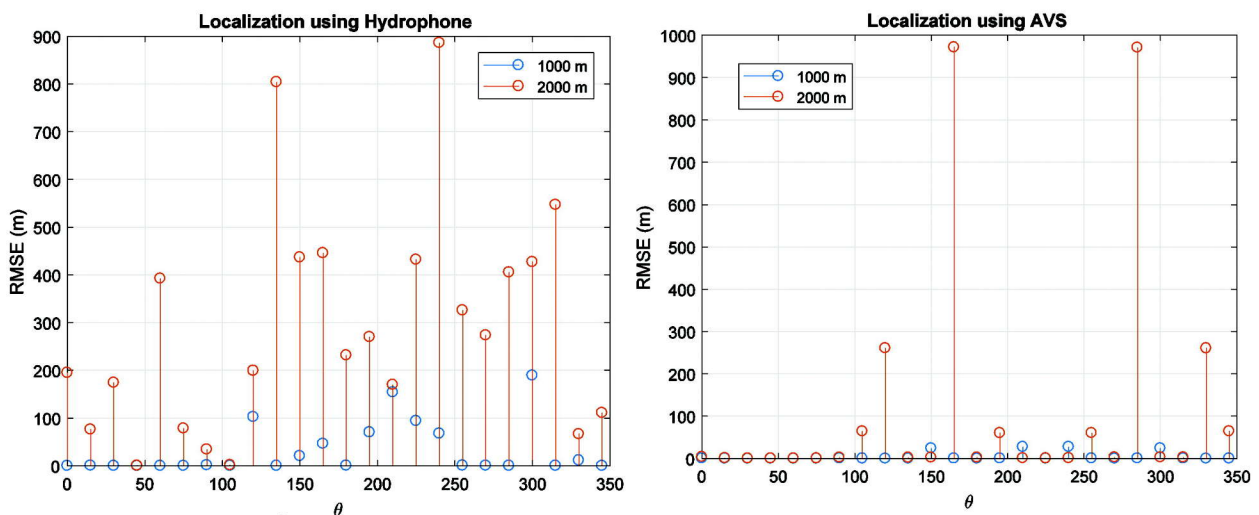

Fig. 5. RMSE of location estimation with respect to bearing for range of 1000 and 2000 meters for L-shape using hydrophone or AVS based sonobuoys.
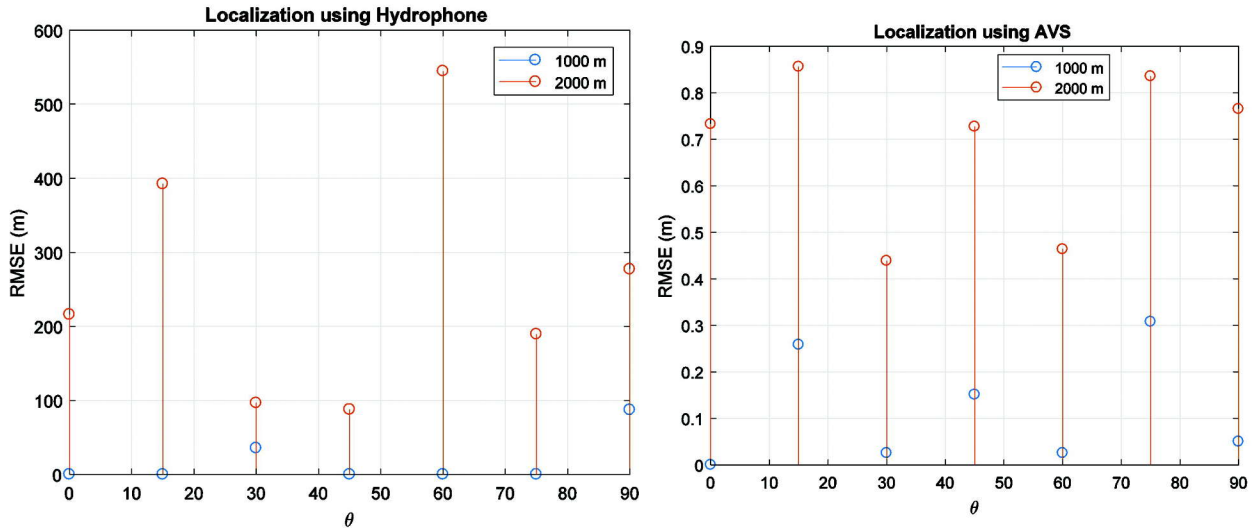
Fig. 6. RMSE of location estimation with respect to bearing for range of 1000 and 2000 meters for circular shape using hydrophone or AVS based sonobuoys.

system deployment. Also, by increasing the number of sonobuoys from 5 to 7 for both hydrophone and AVS based systems, the localization accuracy is improved.

5.3. Varying the distance between sonobuoys in addition to varying the distance between radiated source with respect to the origin coordinate of sonobuoys for L-shape geometry of deployment

In this sub-section, we report the simulation study on the deployment distance between the sonobuoys, for both AVS and hydrophone types. In Figure 7, we can observe that the RMSE decreases on increasing the distance between sonobuoys from 100 m to 400 m. Also, AVS based sonobuoys gives more accuracy as compared to hydrophone based sonobuoys. In Figure 8, we can see that as the mean distance between the sonobuoys and target increases with increase in the number of sonobuoys, there is an increase in the RMSE. Hence, it can be inferred from this study that the mean distance between sonobuoys and target directly affects the RMSE.
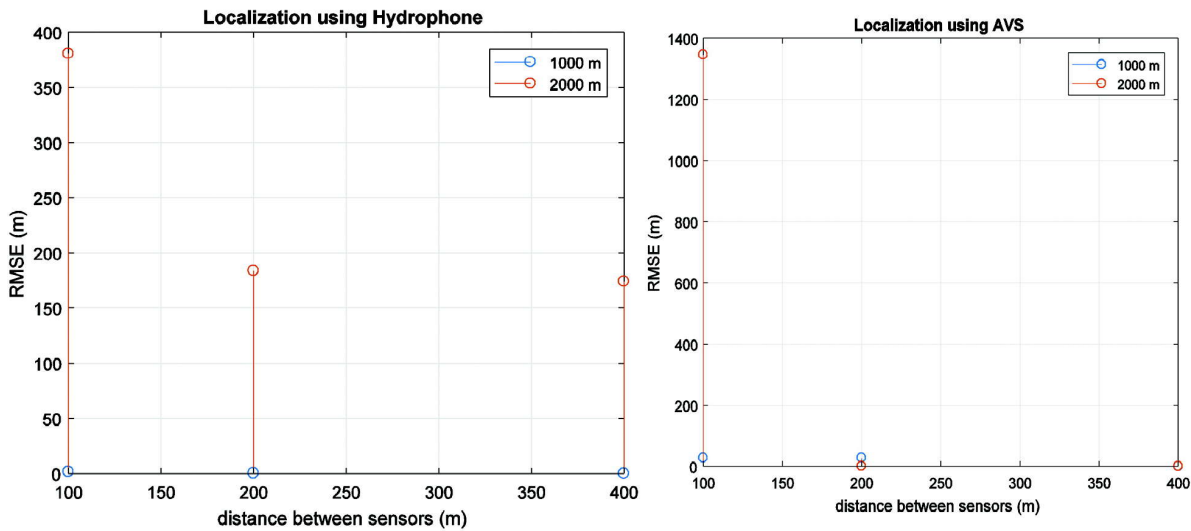
Fig. 7. RMSE of location estimation with respect to distance between sonobuoys, for range of 1000 and 2000 meters for L-shape using hydrophone or AVS based sonobuoys.
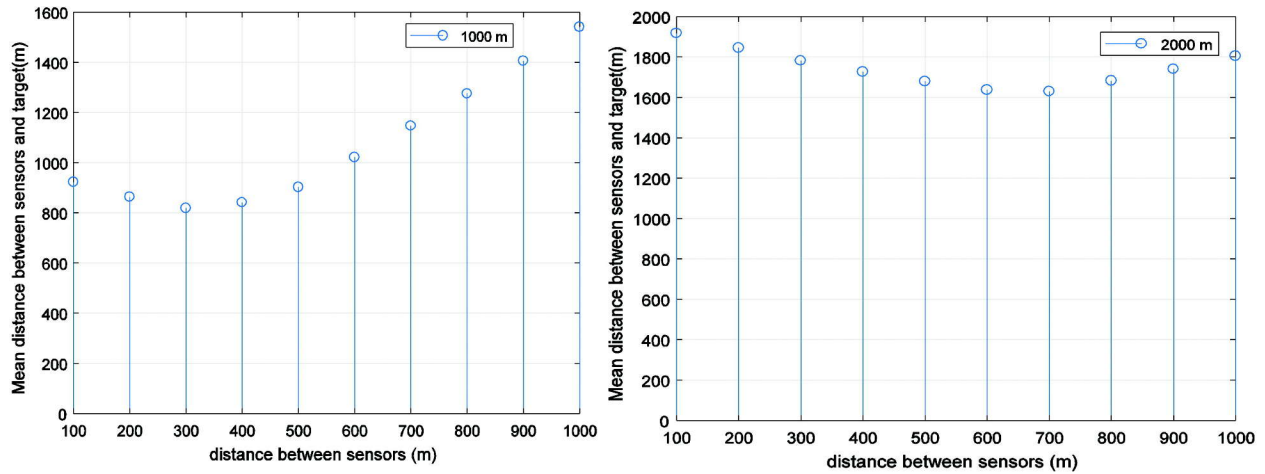
Fig. 8. Mean distance between sonobuoys and target
when the target is at (i) 1000 m, and
(ii) 2000 m from the origin coordinate of the sonobuoys.

5.4. Varying the SNR of single source with respect to the origin coordinate of sonobuoys for circular and L-shape deployment geometries with 5 sensors.

In this sub-section, we consider the performance as a function of the SNR of the source that is measured with respect to the origin coordinate of the sonobuoys. From Figures 9 and 10, we can see that RMSE of localization using either hydrophones or AVS based sonobuoys decreases with increase in SNR except at SNR =20 dB using hydrophone for L-shape geometry due to increase in mean distance. It is also seen that L-shape and circular geometry provide about the same RMSE.
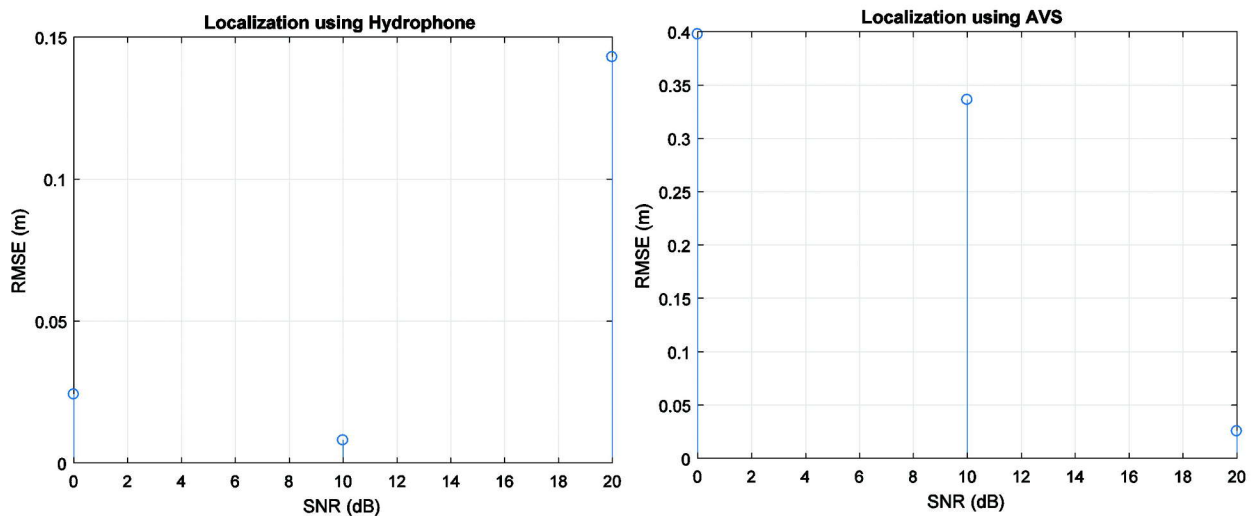
Fig. 9. RMSE with respect to SNR for sea-state 3 and
L-shape using hydrophone or AVS based sonobuoys.
Target is located at 30 degrees to the x-axis.
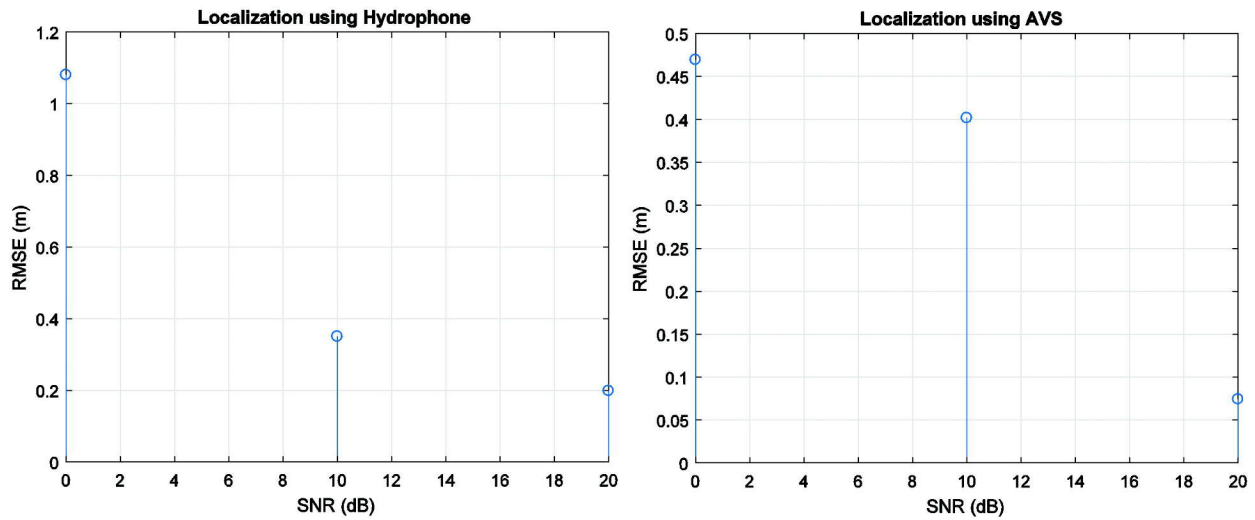
Fig. 10. RMSE with respect to SNR for sea-state 3 and circular shape using hydrophone or AVS based sonobuoys. Target is located at 30 degrees to the x-axis.

5.5. Varying the SNR of single source with respect to the origin coordinate of sonobuoys of a single source for circular and L-shape with 7 sensors.

Here, we show the analysis of RMSE performance as a function of the SNR of the source signal as measured at the origin of the deployed sonobuoy system. From Figures 11 and 12, it is seen that RMSE of localization using either hydrophone or AVS based sonobuoys both decrease with increase in SNR, except at SNR = 20 dB SNR for L-shape hydrophone sonobuoy system deployment. On increasing the number of sonobuoys from 5 to 7, both the geometries provide similar values of RMSE.
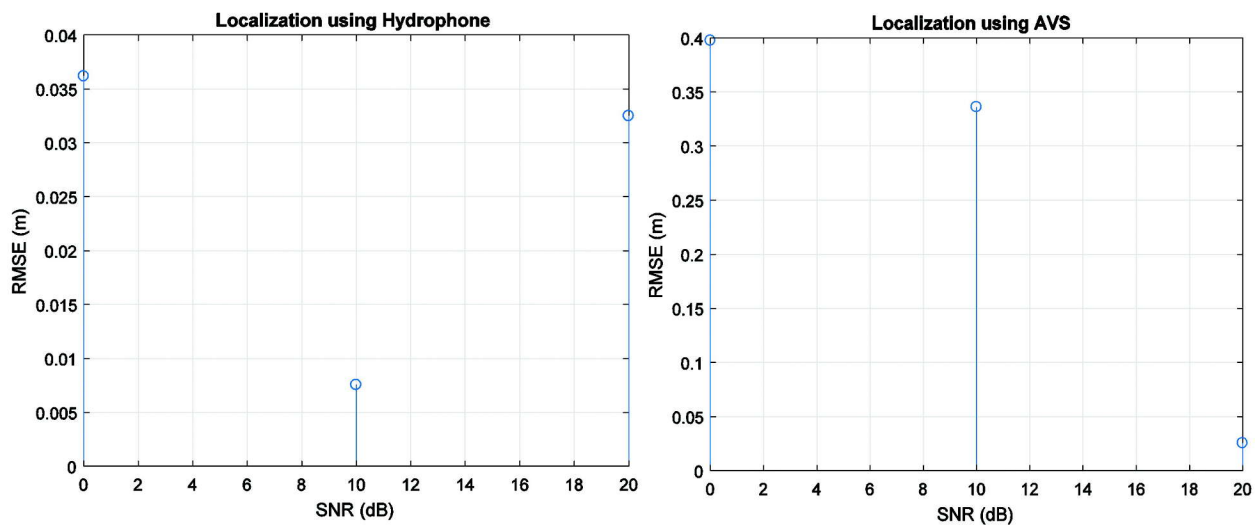
Fig. 11. RMSE with respect to SNR for sea-state 3 and L- shape using hydrophone and AVS based sonobuoys.
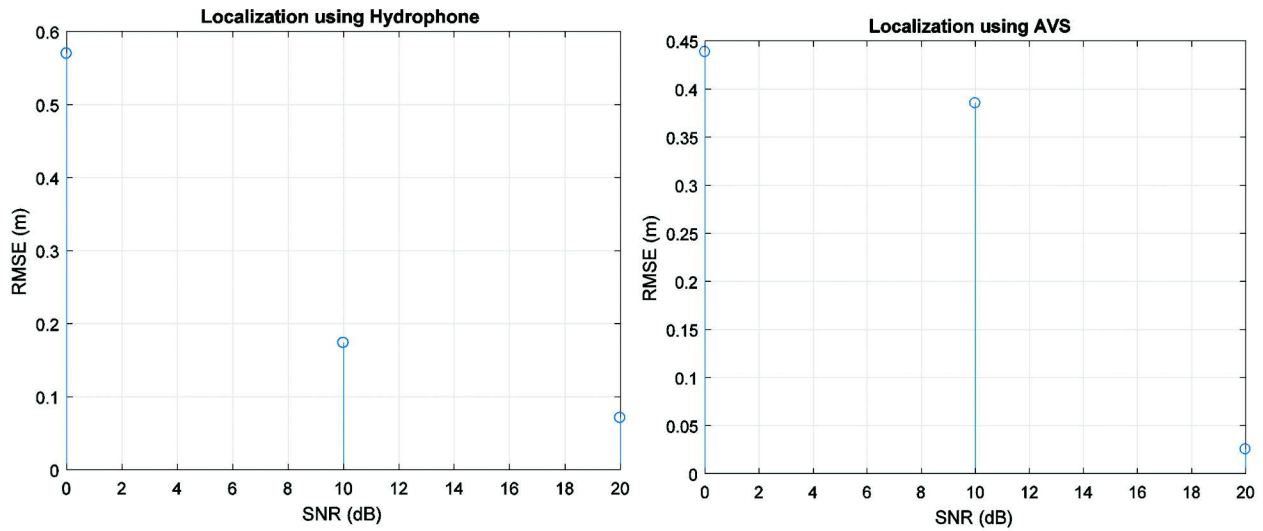
Fig. 12. RMSE with respect to SNR for sea-state 3 and circular shape using
hydrophone and AVS based sonobuoys.

5.6. Varying the distance and direction of radiated source with respect to the origin coordinate of sonobuoys in the presence of multiple sources for 7 sensors.

In this study, we have varied the interference source angle with respect to x-axis and have kept the target position fixed at (i) 1000 m and (ii) 2000 m, with an angle of 30 degrees from the x-axis. From Figures 13 and 14 we can observe that the AVS based sonobuoys gives much better accuracy as compared to hydrophone based sonobuoys. Also, it can be observed that the circular geometry does not provide significant improvement in localization accuracy as compared to L-shape geometry in the presence of interference source.

Fig. 13. RMSE of source localization with respect to bearing angle for sea-state
3 and L-shape using hydrophone and AVS based sonobuoys in the
presence of interference source.
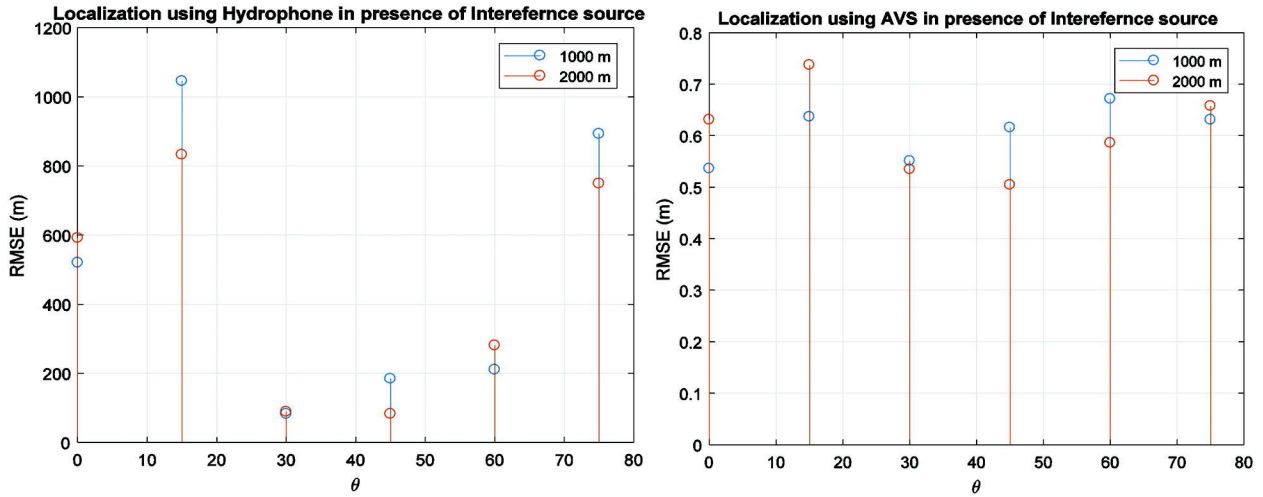
Fig. 14. RMSE of source localization with respect to bearing angle for sea-state 3and circular shape using hydrophone and AVS in presence of interference source.

5.7. Varying the distance and direction of single source with respect to the origin coordinate of sonobuoys in the presence of random drift of 50 m.

In this sub-section, we study the localization performance in terms of RMSE for hydrophone based sonobuoys and AVS based sonobuoys deployed in either circular or L-shape geometry in addition to random drift in sensors with standard deviation of 50 m, for the case of 7 sonobuoys of either type. The source range from the origin of the coordinate system as measured from the sonobuoy deployment geometries is varied, as also the direction of the source with respect to the x-axis.
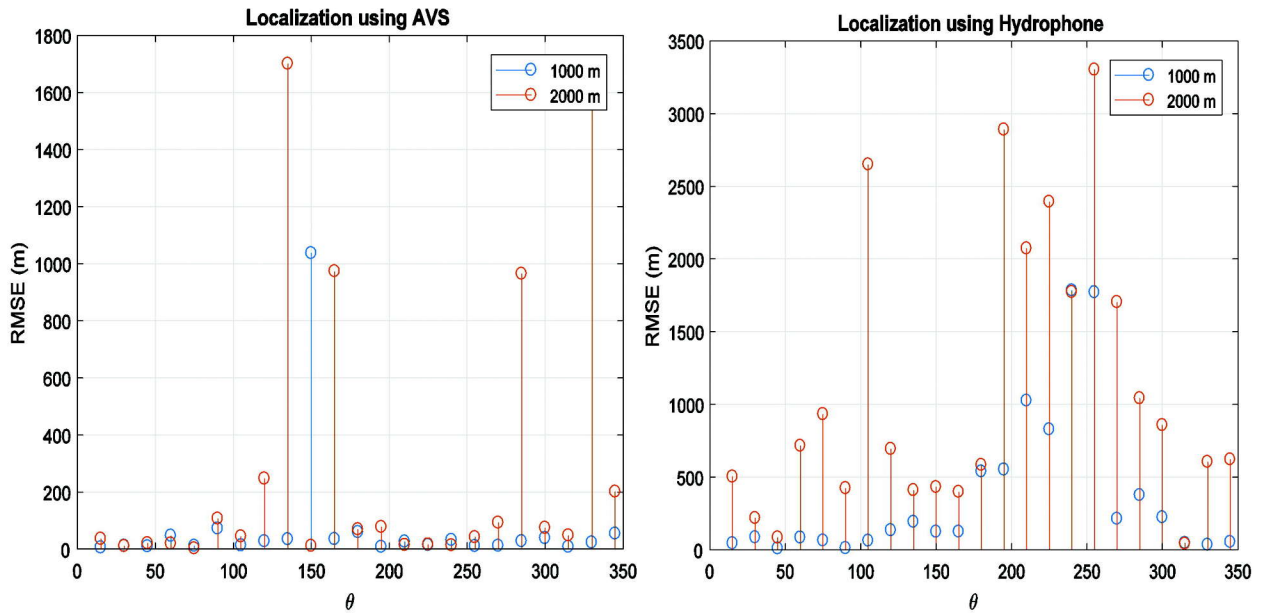
Fig. 15. RMSE of source localization with respect to bearing angle for sea-state
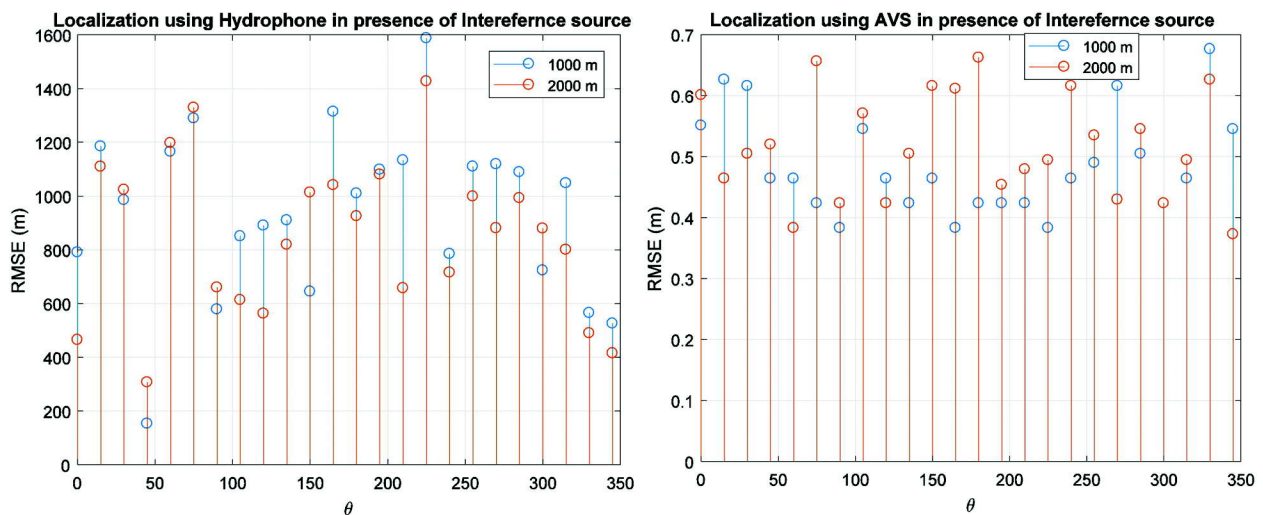3 and L-shape using hydrophone and AVS based sonobuoys inin the presence
of random drift of sensor positions of 50 m standard deviation.
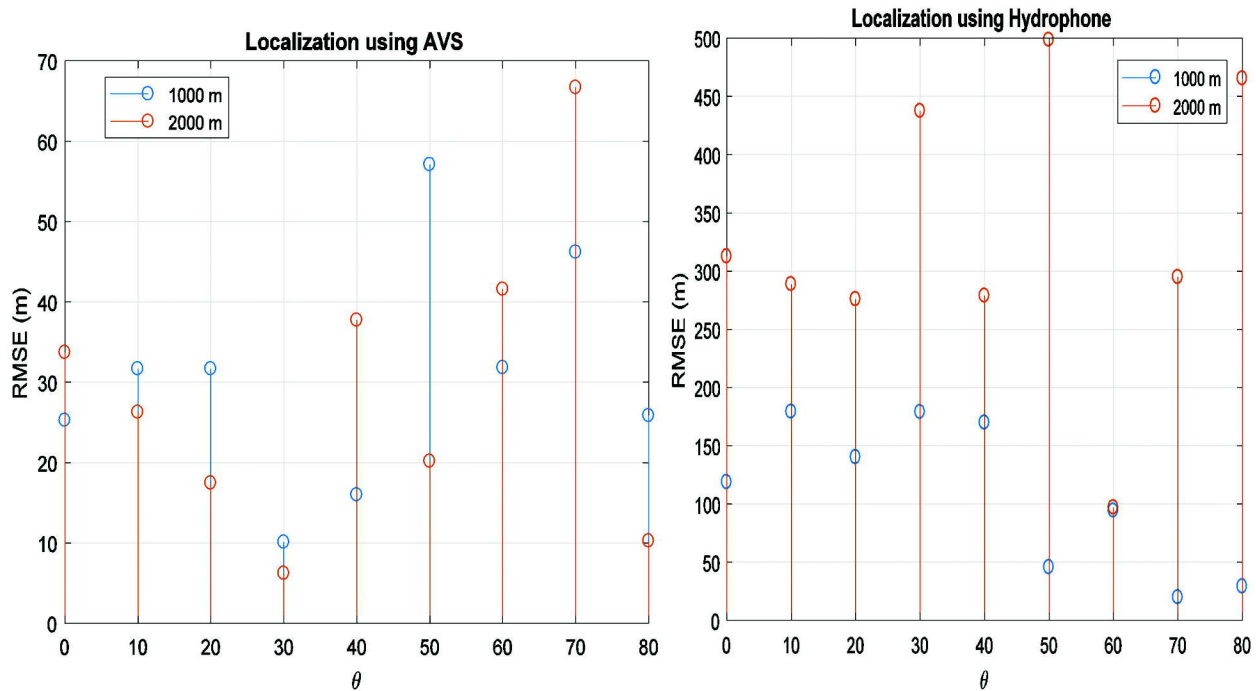
Fig. 16. RMSE of source localization with respect to bearing angle for sea-state 3and circular shape using hydrophone and AVS in presence of random drift of sensor position of 50 m standard deviation.

From Figures 15 and 16, we observe that AVS based sonobuoys gives more accurate location estimation of the source as compared to hydrophone based sonobuoys except at few angles for both L- shape and circular geometries of deployment. Also, by comparing Figures 15 and 16, it is seen that the circular geometry provides significantly larger improvement in localization accuracy as compared to L-shape geometry.

6. CONCLUSION

We have first discussed methods from the literature to estimate TDOA and DOA using GCC-PHAT and arc-tangent algorithms respectively. These methods are applicable for the hydrophone based sonobuoys and the AVS based sonobuoys respectively, since a single omnidirectional hydrophone does not provide DOA information. Based on the estimated TDOA and DOA, we have presented methods to localize the target in 2-D space. For comparing localization using AVS or hydrophone based sonobuoys, several simulation studies have been done to examine the various dependencies of localization performance. The main observations are (i) a circular geometry provides better accuracy as compared to L-shape geometry of sonobuoy deployment, (ii) increasing the number of sonobuoys improves the localization accuracy, and iii) AVS based sonobuoys provide better localization accuracy as compared to hydrophone based sonobuoys, especially in the presence of an interference source. The paper also gives quantitative values of the improvement in terms of RMSE localization errors for various cases that may be useful in planning practical deployment strategies for sonobuoy based source localization.

7. REFERENCES

[1] A. Nehorai and E. Paldi, 1994. "Acoustic vector-sensor array processing," *IEEE Trans. Signal Process,* **42**, 2481-2491.

[2] J. Reed, C. da Silva and R. Buehrer, 2008. "Multiple-source localization using line-of-bearing measurements: Approaches to the data association problem," *Proc. IEEE Military Communications Conference,* pp. 1-7.

[3]   X. Sheng and Y.H. Hu, 2005. Maximum likelihood multiple-source localization using acoustic energy measurements with wireless sensor network. *IEEE Trans. Signal Process*, **53**, 44-53.

[4]   D. Li and Y. Hu, 2003. Energy-based collaborative source localization using acoustic microsensor array. *EURASIP J. Appl. Signal Process*, pp. 321-327.

[5]   B.T. Fang, 1990. "Simple solutions for hyperbolic and related position fixes," *IEEE Transactions on Aerospace and Electronic Systems*, **26**(5), 748-753.

[6]   J. Abel and J. Smith, 1987. "The spherical interpolation method for closed-form passive source localization using range difference measurements," Acoustics, Speech and Signal Processing, *IEEE ICASSP '87*, pp. 471-474.

[7]   T.S. Rappaport, J.H. Reed and B.D. Woerner, 1996. "Position location using wireless communications on highways of the future," *IEEE Communications Magazine*, **34**(10), 33-41.

[8]   M. Vossiek, L. Wiebking, P. Gulden, J. Wieghardt, C. Hoffmann and P. Heide, 2003. "Wireless local positioning," *IEEE Microwave Magazine*, **4**(4), 77-86.

[9]   G. Carter, 1981. "Time delay estimation for passive sonar signal processing," *IEEE Transactions on Acoustics, Speech, and Signal Processing*, **29**(3), 463-470.

[10]   W. Hahn and S. Tretter, 1973. "Optimum processing for delay-vector estimation in passive signal arrays," *IEEE Transactions on Information Theory*, **19**(5), 608-614.

[11]   C. Knapp and G. Carter, 1976. "The generalized correlation method for estimation of time delay," *IEEE Transactions on Acoustics, Speech, and Signal Processing*, **24**(4), 320-327.

[12]   Y.T. Chan and K.C. Ho, 1994. "A simple and efficient estimator for hyperbolic location," *IEEE Transactions on Signal Processing*, **42**(8), 1905-1915.

[13]   S. Davies, 1987. "Bearing accuracies for arctan processing of crossed dipole arrays," *Proc. Oceans Conference*, pp. 351-356.

[14]   B.H. Maranda 2003., "The statistical accuracy of an arctangent bearing estimator," *Proc. Oceans Conference*, **4**, 2127-2132.

[15]   A. Griffin and A. Mouchtaris, 2013. 'Localizing multiple audio sources from DOA estimates in a wireless acoustic sensor network', *Proc. IEEE Workshop on Applications of Signal Processing to Audio and Acoustics*, pp. 1-4.

[16]   A. Griffin, A. Alexandridis, D. Pavlidi, Y. Mastorakis and A. Mouchtaris, 2015. A.: 'Localizing multiple audio sources in a wireless acoustic sensor network', *Signal Processing*, pp. 54-67.

Acoustic imaging and prospecting with back propagation in time reversal based on discrete huygens' modelling, Revisited

Y. Kagawa[1], Y. Zhao[1], L. Chai[1], N. Wakatsuki[1] and M. Singh[2]
[1]Department of Electronics and Information Systems, Akita Prefectural University,
Tsuchiya-Ebinokuchi 84-4, Yurihonjo, Akita 015-0055, Japan
[2]Acoustics and Vibration Metrology Section
CSIR-National Physical Laboratory, Dr. K.S. Krishnan Marg, New Delhi-110 012, India
[1]y2kagawa@gmail.com, [2]mahavir.acoustics@gmail.com

ABSTRACT

The paper discusses the discrete Huygens' modelling to describe the propagation and the application to the acoustic imaging, demonstrated with the back propagation in time reversal process. Discrete Huygens' model is a discrete version of the Huygens' Principle, with which the sequence and the process of the progress and the scattering can be simulated for wave propagation phenomena. As it provides a physical model, it does not require the solution of the wave equation but traces the sequences of the impulse scattering at the nodes taken at the intersections in the orthogonal transmission-line models. The advantage of the present physical model lies on the fact that as the algorithm is absolutely stable and as the inverse scattering matrix is the same as the original forward one, the same algorithm applies to the back propagation in time reversal due to the system in symmetrical with respect to time. The energy distribution evaluation over the field of interest leads to the imaging of an object under sensing.

1. INTRODUCTION

Imaging, exploration and prospecting are important fields in remote sensing. Acoustic waves have been used for sensing for many decades.

The most popular pulse echo sounding is a radar-type imaging technique, in which the imaging is made due to the strength of the reflected pulse and its transmission time to the reflected pulse from an object surface. The emanating wave must have a narrow beam, which is to be steered. The advantage of this system is that the pulse wave transmitting and receiving can be made one-sidedly, while the disadvantage is that the imaging is disturbed by the presence of the irregular field in the paths through which the emanating and reflected waves travel. Since the invention of so-called X-ray CT, the transmission type imaging systems of various kinds have been developed. An object to be sensed is placed between the transmitter and the receiver, between which the attenuation is measured along a line. The measurement is repeated as the direction of the line of the measurement is rotated. The image is reconstructed from the data back projected[1]. The narrow beam is again required, and the scattering and reflection at the various media intersurfaces are a nuisance and may cause an error. Another imaging technique is a scattering

tomography. Born or Rytov approximation must be used for linearizing the wave equation. It does not always work reasonably in practice[2].

The imaging technique in the present paper belongs to the scattering tomography but depends on the different mechanism, based on the back propagation in time reversal. For the image reconstruction, the back propagation uses the same algorithm as the forward propagation. The imaging lays in the fact that the scattered signals come back to the original source points from the secondary sources, that is, the reflection between the object surface and the surrounding medium.

The imaging techniques are an inverse problem. Some mathematics of the solution in time reversal process has been discussed. A wave equation is reversely solved, that is, initial conditions and parameters are sought from the response data for the wave equation and the associated boundary conditions[3]. A mirror process could be associated[4]. It is not easy to solve and not straightforward.

The present approach is based on the completely different mechanism as that no wave equation needs be solved inversely. Instead, the spatial energy density distribution is only evaluated in association with the backpropagation process. The region of higher pressure density corresponds to the secondary source regions that include the sources from the inner surfaces boundaries.

The paper first introduces the discrete Huygens' models, developing the scattering matrix for the medium of different impedances.

It is also shown that the inversion of the scattering matrix leads to the original scattering matrix, not only for the standard matrix regardless of the modified matrix for different propagation velocity and density. This is an alternative proof of the reciprocity principle and the system symmetry for time. In next physical problems, the systems are symmetrical with time, at least in ideal sense. The more example of simulation based on the back propagation in time reversal are demonstrated for the cases when all the data are accessible on the remote surface surrounding an object and for some cases when some data are missing, as the prospecting must sometimes be required on the one-sided boundary.

2. PROPAGATION

2.1 Discrete Huygens' models

The present paper first introduces a discrete counterpart to the Huygens' principle[5] - [10]. Some explanations are repeated for the paper to be self-contained.

The discrete Huygens' modelling which the authors refer to is known as the transmission-line matrix modelling (TLM) in the electromagnetic engineering community, which is best explained by the equivalent electrical transmission-line theory. P. B. Johns originally developed it for the electromagnetic field problem analysis [11] - [13].

What is particular about his method is that the solution is sought in a transmission-line network equivalently taken to the field of interest in the time domain, while the transmission-line has traditionally been solved in the frequency domain. The time domain solution is then obtained by Laplace transformation. The time domain solution procedure is here made for a series of the equally spaced transmission lines, which results in the scattering of the impulses at the crossed nodes taken at the equally spaced intervals. As computers become increasingly powerful both in execution time and memory size, engineers sometimes favour the direct time-domain approach, which provides the full wave solution.

We consider here the sound wave propagation and confine ourselves to a two-dimensional field model. As the sound wave is scalar, generality will not be lost because of the two-dimensional modelling. It is very easy to extend to the three-dimensional modelling except that it requires more computational resources. Waves radiate from a point source spherically. According to Huygens' principle, a wavefront consists of some secondary point sources, each of which gives rise to spherical waves, and the envelope of these waves forms a new spherical wavefront which again gives rise to a new generation of spherical waves and so on. The Huygens' principle is here considered in the discrete sense to implement this process of sequences

on a digital computer. This process is assumed to occur adhering to the directions of the Cartesian coordinates. The propagation takes place as the sequence of the impulse transmission and scattering at a node or an element with four to six branches of the transmission lines. When a sound impulse of unit amplitude is incident to one of the nodes, the sound impulses scatter in four to six directions.
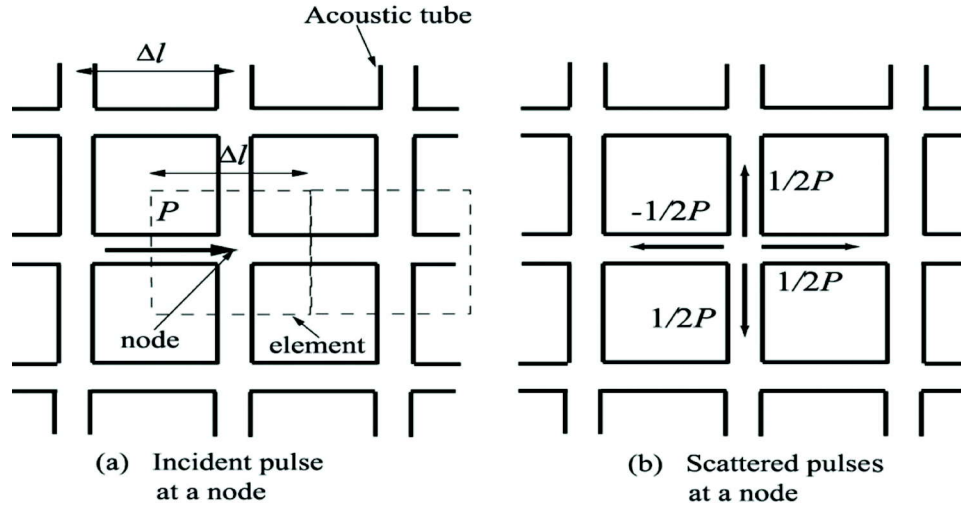
Fig. 1. Discrete Huygens' model for the acoustic tube mesh corresponding to the field

A two-dimensional acoustic field is equivalently placed by the orthogonal mesh made of the acoustic transmission lines or tubes as shown in Fig. 1. The orthogonally connected transmission lines form impedance discontinuity at the node because the characteristic impedance in a tube (= $\rho c_0 S$, where ρ is density and c_0 sound speed and S cross-sectional area) is the same for each branch and three branches are connected to one at the node, so that the impedance looked from one branch into the node is one-third. When an impulse of amplitude P is incident to one of the nodes, the scattering takes place. Each scattered pulse has one-quarter of the incident energy, and the magnitude of the scattered pressure is one-half, in which the sign of the reflected one to the incident direction is negative. This resembles the collision of the elastic balls of molecules as shown in Fig. 2 (a).
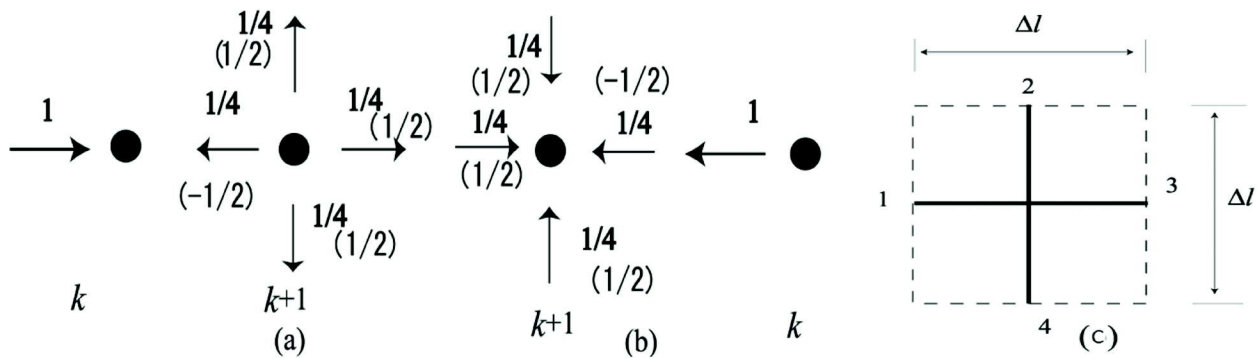
Fig. 2. Scattering and concentration in a two-dimensional element.
(a) Incident and scattered impulses; (b) time-reversed process. Numbers indicate the amount of energy (those in the parenthesis are for pressure); (c) the branches are numbered in clockwise.

For the general case, four impulses $P^1 \sim P^4$ are incident to the four branches at the same time $t = k\Delta t$ (where $\Delta t = \Delta_0 l/c_0$ is the time delay required for a pulse to travel the distance Δl, c_0 is propagation speed

along the tube or in free field, and k is the integer). The response can be obtained by superposing the contribution from all branches. The scattered impulse S^n at branch n at time $t + \Delta t = (k + 1)\,\Delta t$ is given as

$$_{k+1}S^n = \frac{1}{2}\sum_{m=1}^{4}{}_k P^m - {}_k P^n \tag{1}$$

where, $_k P^n$ indicates the incident impulse at branch n at time $t = k\Delta t$. This can be rewritten in the form of a scattering matrix expression as

$$\begin{bmatrix} S^1 \\ S^2 \\ S^3 \\ S^4 \end{bmatrix}_{k+1} = \frac{1}{2}\begin{bmatrix} -1 & 1 & 1 & 1 \\ 1 & -1 & 1 & 1 \\ 1 & 1 & -1 & 1 \\ 1 & 1 & 1 & -1 \end{bmatrix}\begin{bmatrix} P^1 \\ P^2 \\ P^3 \\ P^4 \end{bmatrix}_k$$

or
$$_{k+1}\{S\} = [A]\,_k\{P\} \tag{2}$$

where $[A]$ is can be called a scattering matrix. Pressure $P_{i,j}$ at the node of an element is given by

The radiated signal is assumed to be of low frequency so we have not considered absorption loss which is negligible as compared to geometrical spreading loss. The signal received at the ith sensor can thus be expressed as,

$$P_{i,j} = \frac{1}{2}\sum_{n=1}^{4}{}_k P^n \tag{3}$$

where, subscripts i, j represent the nodal position $(x, y) = (i\Delta l, j\Delta l)$, and the superscript numbers are referred to Fig. 2(c).

When the field is divided into square meshes, the scattered pulses which travel along the branches in reverse directions become incident pulses to the adjacent elements at whose nodes scattering again takes place. The scattered pulses represent the incident pulses to a node at position (i, j) at the adjacent nodes as

$$\begin{aligned}
_{k+1}P^1_{i,j} &= {}_{k+1}S^3_{i-1,j}, & _{k+1}P^1_{i,j} &= {}_{k+1}S^1_{i-1,j} \\
_{k+1}P^2_{i,j} &= {}_{k+1}S^3_{i,j+1}, & _{k+1}P^4_{i,j} &= {}_{k+1}S^2_{i,j-1}
\end{aligned} \tag{4}$$

This is the compatibility condition for the element connection. Repeating the operation of equations (2)-(4) on all nodes, the impulse responses in the field are traced at successive time intervals. The method is inherently the time domain approach, which is quite suitable for the simulation and visualisation of wave propagation behaviour on the computer.

2.2 Wave equation

It is possible to show that the wave equation can be created from the scattering algorithm.

Eq. (1) is substituted into Eq. (3) and applying the compatibility condition (4) in consideration of the adjacent nodes, so that the following expression is obtained for the pressures

$$_k P_{i-1,j} + {}_k P_{i+1,j} + {}_k P_{i,j-1} + {}_k P_{i,j+1} - 4\,{}_k P_{i,j} = 2({}_{k-1}P_{i,j} - 2\,{}_k P_{i,j} + {}_{k+1}P_{i,j}) \tag{5}$$

This expression leads to the wave equation as the distance Δl becomes small. This means that the discrete Huygens' model is equivalent to FD-TD, but it should be emphasised that the algorithm or the solution process is quite another. What is important is that the present model provides a physical model following to the Huygens' principle, which does not require the numerical solution of the wave equation, and present process is absolutely stable.

Expansion of Eq. (5) in Tayer series about $_k P_{i,j}$ arrives at the wave equation

$$\frac{\partial^2 P}{\partial x^2} + \frac{\partial^2 P}{\partial y^2} = \frac{1}{c^2}\frac{\partial^2 P}{\partial t^2} + \varepsilon \qquad (6)$$

with small error term ε, where

$$\varepsilon = 2\left\{\frac{\Delta l^2}{4!}\left(\frac{\partial^4 P}{\partial x^4}+\frac{\partial^4 P}{\partial y^4}\right)+\frac{\Delta l^4}{6!}\left(\frac{\partial^6 P}{\partial x^6}+\frac{\partial^6 P}{\partial y^6}\right)+\cdots\cdots\right\}+4\left\{\frac{1}{4!}\frac{\partial^4 P}{\partial t^4}+\frac{\Delta l^2}{6!}\frac{\partial^6 P}{\partial t^6}+\cdots\cdots\right\}$$

which vanishes as $\Delta l \to 0$. As for Eq. (5) is valid for any $_kP_{i,j}$, it is replaced by P and $c = c_o/\sqrt{2}$.

Two routes or schemes are possible for computer simulation, as shown in the followings.
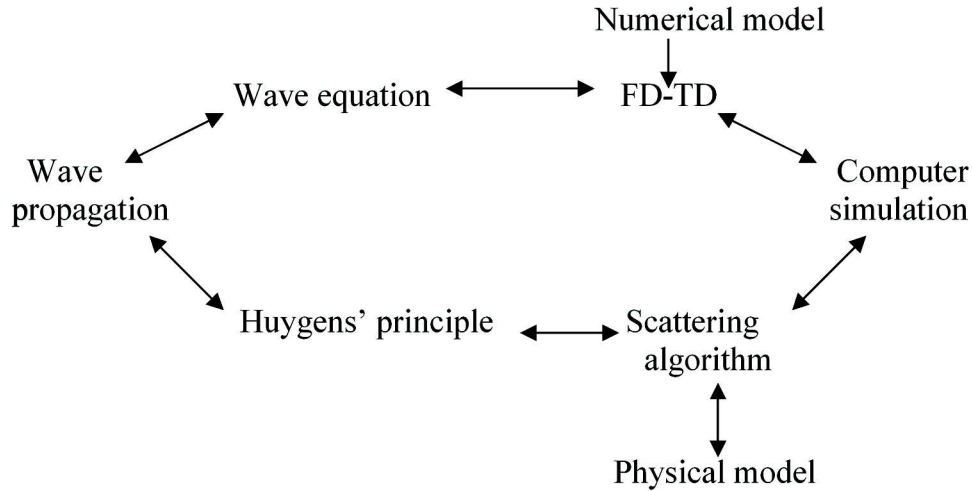
2.3 Propagation

By comparing Eq. (6) with the wave equation in free field, one finds that period the propagation speed in our network is slower by the factor $1/\sqrt{2}$ than that of the free field $c_0\sqrt{2}$ is a fraction, which corresponds to the diagonal length of the mesh. This factor is $1/\sqrt{3}$ for the three-dimensional field modelling. The propagation speed along the line is also delayed due to the presence of a pair of stubs of length $\Delta l/2$ attached to a rode. The propagation velocity C_p one transmission lines in x - or y-direction is given by

$$C_p = C_0\frac{\pi sl}{\lambda\sin-1\left\{\sqrt{2}\sin\left(\frac{\pi sl}{x}\right)\right\}}$$

$$\approx \frac{1}{\sqrt{2}} \ \text{for small } \lambda \qquad (7)$$

The line shows a low-pass characteristic, having the cut-off at $\Delta l = \lambda/4$.

The propagation on speed depends on the direction of the propagation, and cause the dispersion effect, which is not very large as $C_p/C_o = 0.981$ for $\Delta l/\lambda = 1/10$. Please see the references (13), (16) for more information.

Dispersive systems are not exactly symmetric with time as waves propagate. In many engineering problems, however, the dispersion is supposed to be small so that the effect is involved. The effect may appear in terms of some errors.

2.4 Non-reflective boundary

In many applications, an infinite domain simulation must be required. To achieve this condition, the non-reflective boundary must be provided surrounding the field of interest. The simplest and the most practical

way is to terminate the boundary of the field by the characteristic impedance Z_0 ($= \rho c_0$) of the free field. As in our network field, the travelling speed is lower by the factor $1/\sqrt{2}$, the reflection coefficient at the boundary must be

$$\tau = \frac{Z_0\sqrt{2} - Z_0}{Z_0\sqrt{2} + Z_0} = -0.17157 \tag{8}$$

With this condition imposed on the branch contacting to the outer space, the transparent condition can practically be assumed on the boundary as a quasi-boundary. This is however only valid for the plane wave incidence. The reflection slightly increases for the oblique incidence. Many other modelling is attempted to reduce the reflection. For some models, one assumes that no reflection wave is possible [14] and another provides absorbing multi-layers [15].

2.5 Inhomogeneous and dissipative media

The medium can be inhomogeneous, which can be realised by providing a proper stab tube or transmission line connected to the node as the 5th branch, with which the field characteristic impedance or the propagation speed can be varied (decreased). The stub works as an additional compliance or capacitance with the time synchronisation kept. This is illustrated in Fig. 3.
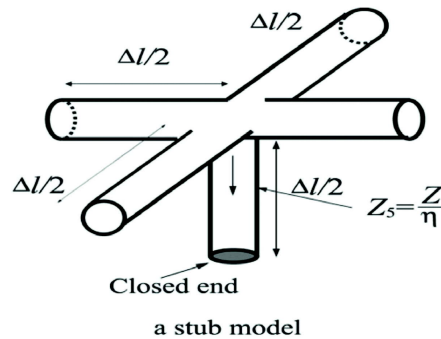
Fig. 3. Stub tube model with the fifth branch (velocity is controlled by the presence of this branch with the characteristic impedance changed by choosing parameter η property)

The scattering matrix defined in Eq. (2) is now given as

$$[A] = \frac{1}{2 + \frac{\eta}{2}} \begin{bmatrix} a & 1 & 1 & 1 & \eta \\ 1 & a & 1 & 1 & \eta \\ 1 & 1 & a & 1 & \eta \\ 1 & 1 & 1 & a & \eta \\ 1 & 1 & 1 & 1 & \eta \end{bmatrix} \tag{9}$$

where, η is the characteristic impedance parameter of the stub tube, and

$$a = -\left(1 + \frac{\eta}{2}\right), \quad b = -\left(2 - \frac{\eta}{2}\right)$$

Pressure vectors $_{k+1}\{S\}$ and $_k\{P\}$ consist five components. The condition for the 5th branch is that the input pulse to the 5th branch, is reflected back to the node with time delay Δt from the closed end, which has no connection to other elements so that $_kP5 = {}_{k+1}P5$

Though it is not directly concerned with the present paper, some are commented for other field conditions. The dissipative field can also be modelled by the introduction of another 6th tube of infinite length. The infinite length means no reflection, introducing energy dissipation. The wave propagation in

the mean-flowing medium means that the propagation speed is accelerated or retarded depending on the direction of the flow. This situation can also be incorporated in the modelling by providing the extra arms at one node directionally coupled with adjacent nodes [9].

3. BACK PROPAGATION

3.1 Propagation in time reversal

It is not always a simple task to solve the wave equation inversely, analytically or numerically [4]. The particular feature of the present model is that as it is a physical model, the back propagation in time-reversal is possible and can easily be implemented. Our scattering matrix expression is expressed by

$$_{k+1}\{S\} = [A]_k \{P\} \tag{10}$$

Premultiplying $[A]^{-1}$ on both side, knowing that

$$[A]^{-1} = [A] \tag{11}$$

One has thus,

$$_k\{P\} = [A]_{k+1} \{S\} \tag{12}$$

This is a time reversal process. The mechanism is depicted in Fig. 2(b). The mechanism is depicted in Fig. 2(b). It is interesting that identity of Eq. (11) is valid not only for Eq. (2) but also for Eq. (9) so that the backpropagation algorithm is the same as that of the forward propagation without regarding the medium properties. This is our finding in the present paper. The time reversal invariance is also mentioned in the particle model (17). The inversion of Eq. (9) can easily be checked by the use of MATHEMATICA. This means that when the output signals were put back into the places at which signals are measured, they came back to the original input source points. This is the key mechanism that can be utilised for the source identification and tomographic imaging. In the physical problem, systems are symmetrical with time, provided they are ideal. It is not so in real cases, where the loss is present so that the entropy increases as the wave propagates. The systems are, to be exact, not symmetrical with time. In many engineering models, however, when the loss is small, it can be ignored. The effect of the loss is evaluated regarding the errors as such. In the present demonstration here we only consider such cases where the systems are a reversal in time

Suppose an object whose characteristic impedance is different from that of the surrounding medium. When a source illuminates it, scattering will take place from its boundary. The scattered data collected along a line surrounding the field that encloses the object are back-propagated, and then the signals will go back to the source by way of the secondary sources over the object boundary. It suggests a possibility of imaging the presence of the inhomogeneity boundaries in the backpropagation approach by evaluating the energy density distribution in the space.

3.2 Some demonstrations

3.2.1 Source identification

Some identifications were well-demonstrated for the multiple and distributed sources in ref. [10].

The original sound sources are reversed from the scattered data collected by the receiving array along the surrounding boundary. The wave signals are recorded at many points over a surrounding boundary (non-reflective). They are put into the receiving boundary back, and then the waves go back to the source points. The simulated results show that if the data are collected at the interval points apart more than the wavelength of the signals, the identification may fail.

3.2.2 Imaging

The case when the impedance of an object, ρc is higher by 10% (due to higher density) than that of the surrounding medium is demonstrated in ref. [10]. In the present paper, the examination is extended to the cases with the media of different propagation speed and with the different energy evaluation processes of

the data. The object is illuminated by point sources over the boundary enclosing the object, and the scattered data are all recorded which are assumed to be the measured data. In the simulation, that is, the forward propagation responses are used for the 'measured' data. The data signals recorded are back-propagated into the vacant free space. For all the simulation to follow, the one-shot emanation of 16 impulses with the Gaussian profile is used for the exciting sound sources.

For imaging two possible data processing are considered. (Process 1): One procedure is to obtain the spatial distribution of the time-integrated energy at every node of the mesh in the back-propagation process. The spatial distribution is calculated concerning the values distributed for the empty field. (Process 2): Another procedure is that the compensation is made for the 'measured' data concerning the reference data calculated for the empty field before the backpropagation. The compensated data are then back-propagated into the free space for which the time-integrated energy density distribution is evaluated.
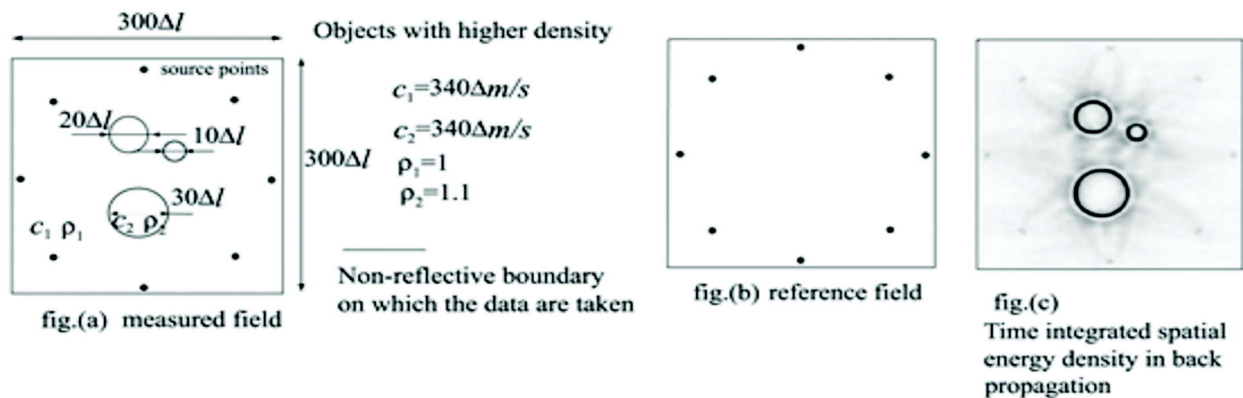
Fig. 4. Inversion, Multi-objects with higher density (Process 1)

Fig. 4 shows the case of multi-body objects when their mass density is 10% higher than that of the surrounding medium, while their propagation velocities are the same. With Process 1, the objects' boundaries are well visualised. However, for the case when the propagation speeds are different while the density is the same (the case when the propagation speed is lower by 10% in the objects), the results are very poor as shown in Fig.5. This last case can be improved with the use of Process 2. The results are as shown in Fig. 6.

The back-propagation is taken for every single excitation, and the result is superposed for all excitations.

Fig. 5. Inversion, Multi-objects with lower propagation speed (Process1)

$300\Delta l$

• source points

$20\Delta l$ $10\Delta l$

$30\Delta l$

$c_1\ \rho_1$ $c_2\ \rho_2$

fig.(a) measured field

Objects with lower propagation speed

$c_1=340\Delta m/s$

$c_2=306\Delta m/s$

$300\Delta l$ $\rho_1=1$

$\rho_2=1$

————

Non-reflective boundary on which the data are taken

fig.(b) reference field

fig.(c)
Time integrated spatial energy density in back propagation
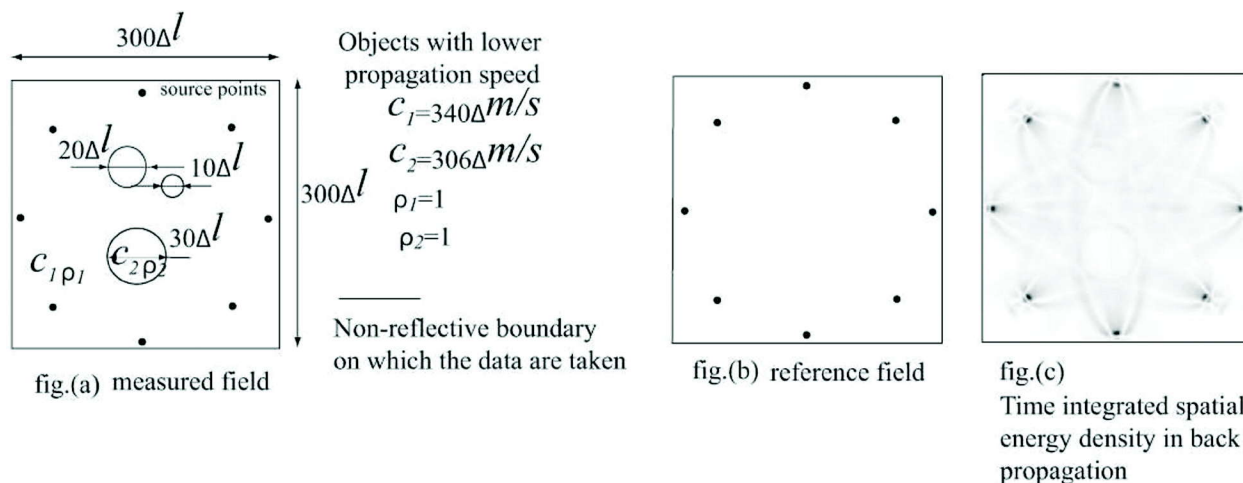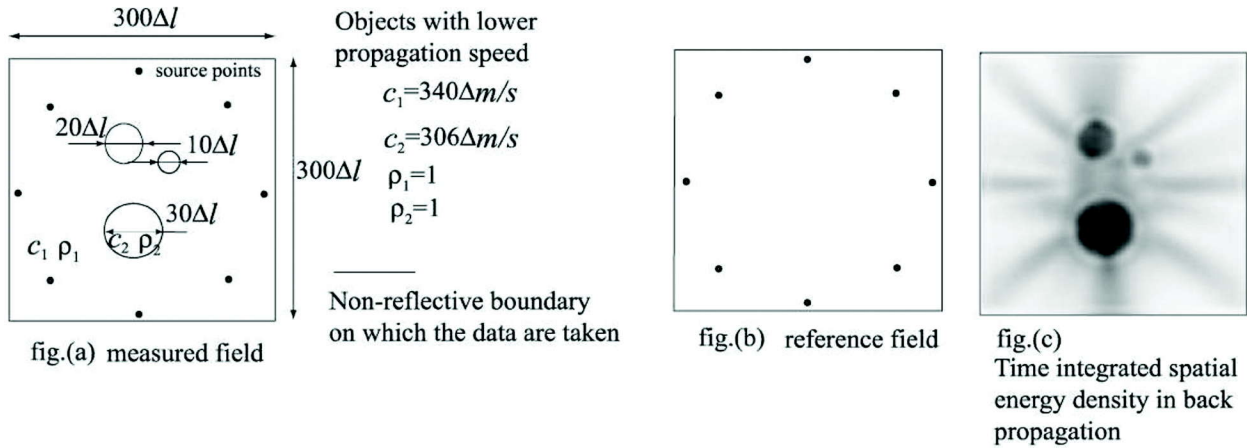
Fig. 6. Inversion, Multi-objects with lower propagation speed (Process 2)

Fig. 7 shows the result when the propagation speed in the objects is higher by 10% (Process 2). The objects are again visible, but their diameters look slightly smaller, while in Fig. 6, the objects look slightly larger. This effect may also happen in a radar-type echo-imaging.

$300\Delta l$

• source points

$20\Delta l$ $10\Delta l$

$30\Delta l$

$c_1\ \rho_1$ $c_2\ \rho_2$

fig.(a) measured field

Objects with higher propagation speed

$c_1=340\Delta m/s$

$c_2=374\Delta m/s$

$300\Delta l$ $\rho_1=1$

$\rho_2=1$

————

Non-reflective boundary on which the data are taken

fig.(b) reference field

fig.(c)
Time integrated spatial energy density in back propagation
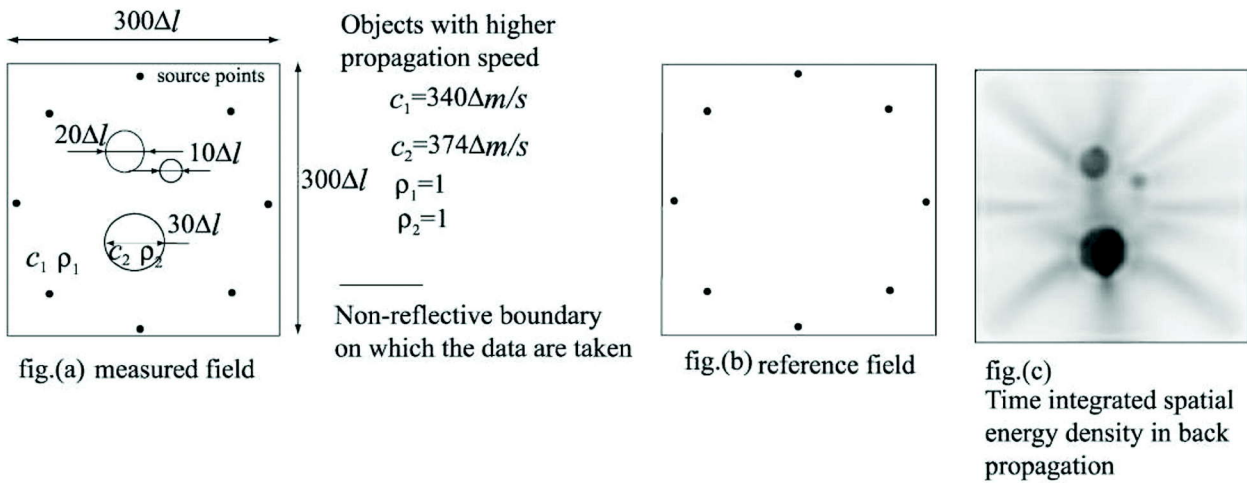
Fig. 7. Inversion, Multi-objects with higher propagation speed (Process 2)

For the field with different propagation velocity, it is found that Process 2 is more effective.

Fig. 8 is the case when the data are not complete, but the hard surface is assumed to present at the bottom which could work as the mirror sources (Process 2). The images are visible.

The back-propagation approach is a scattering tomography. Fig. 8 show that single-sided illumination is possible, but if all received data transmitted from the object are not collected, the result is degraded, as examined in the next simulation.

3.2.3 Sounding

Single-sided sounding models are then considered. Fig. 9 shows an example, in which a circular object with higher impedance (by 10%) is located beneath the ground or sea surface. A point source is provided over the ground surface over which the data are also taken. With different source point, only a part of the upper surface boundary is visible. Fig. 10 is the case when two boreholes driven into the ground are provided for the transmitted data collection. The sound source is placed on the ground surface, and the data are accessible
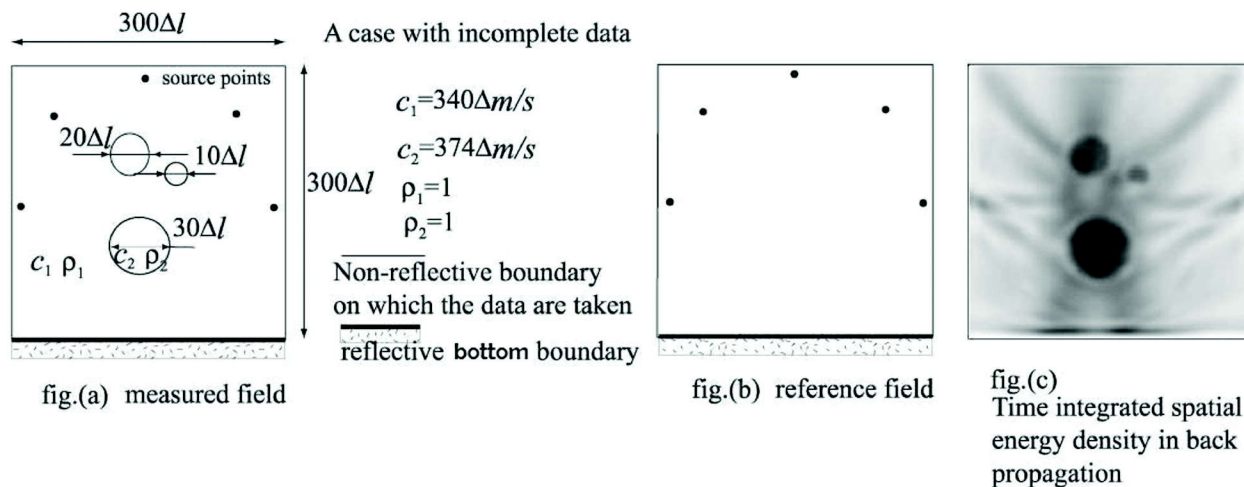
Fig. 8. Inversion, A case with incomplete data
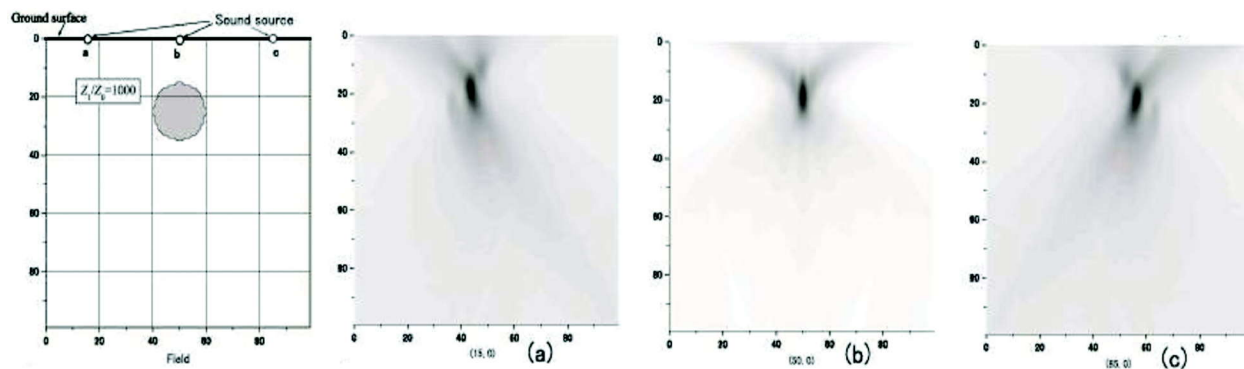
Fig. 9. Inversion, One-sided illumination and data collection
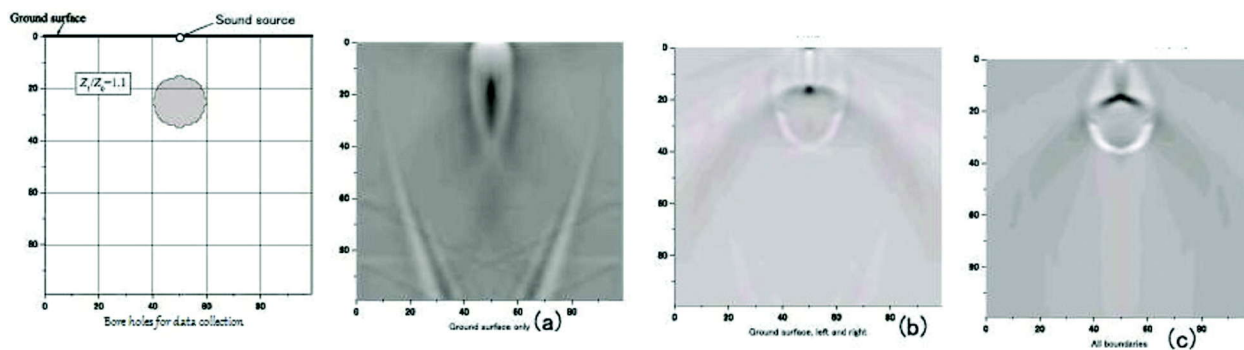
Fig. 10. Sounding with boreholes for data collection

at three-sided boundaries. The result is improved as shown in Fig. (b). Fig. (c) shows the cases when the data could be obtained at the bottom included. In all cases, we see artefacts between the circular objects, which may be caused by the wave interferences.

At this stage, we show the presence of the object boundaries. The quantitative evaluation of the object materials must be our next question.

4. CONCLUDING REMARKS

The discrete Huygens' models have been examined, and the use of the back-propagation approach has been proposed for the imaging. The imaging approach is quite different from that of the so-called scattering tomography. Our finding is that the inversion of the scatting matrix becomes the same matrix without regarding the medium properties. The possibility of the imaging and the remote sensing are here demonstrated by simulation. Extension to the three-dimensional field modelling is straightforward. The present approach features a new technique to the imaging and the remote sensing, which does not require a beam-formed sound source and complex reversal calculation. In the present simulation, we are only concerned about the acoustic wave. The case of the elastic wave problems can also be within our reach[10].

We came across the Viggen's paper of the lattice Boltzmann Method applied to the acoustics based on the particle models. The paper is available via WEB[17] and latest work[18,19]. He introduced the Chopard-Luthi wave model, one of the simplest models among lattice Boltzmann model, which is directly applicable to the wave problems. For comparison, he referred discrete Huygens's model and expressed the interests for the difference. We rather felt the similarity on the contrary, as they take ensemble average for Boolean occupation number, while we take a model of impulsive excitations and responses. This is the motivation of the present paper, where the title accomplishes "revisited".

5. ACKNOWLEDGEMENT

6. REFERENCES

[1] A.C. Kak and M. Slaney, 1988. Principles of Computerized Tomographic Imaging, (New York: IEEE Press).

[2] Y. Kagawa, T. Tsuchiya, T. Ishihara and K. Fujioka, 1996. Some experimental considerations on ultrasonic computed tomography, *Journal of Acoustic Society of Japan,* **52**(8), 605-615.

[3] M.K. Klibanov and A. Timonov, 2003. On the mathematical treatment of time reversal, *Inverse Problems.* **19**, 1299-1318.

[4] M. Fink and C. Prada, 2001. Acoustic time-reversal mirrors, *Inverse Problems*, **17R**, 1-38.

[5] Y. Kagawa, 1997. Computational Acoustics – Theories of Numerical Analysis in Acoustics with Emphasis of Transmission-line Matrix Modeling, Int. Symp. on Simulation, *Visualization and Auralization for Acoustic Research and Education, Tokyo,* pp. 19-26.

[6] Y. Kagawa, 2003. Discrete Huygens' model and its application to acoustics. 10th *Int'l. Congress on Sound & Vibration, Stockholm*, 7-10, July.

[7] Y. Kagawa, T. Tsuchiya, B. Fujii and K. Fujioka, 1998. Discrete Huygens' model approach to sound wave propagation, *J. Sound & Vib.*, **218**(3), 419-444.

[8] Y. Kagawa, T. Tsuchiya, T. Hara and T. Tsujii, 2001. Discrete Huygens' modelling simulation of sound wave propagation in varying velocity environments, *J. Sound & Vibr.* **246**(1), 419-436.

[9] Y. Kagawa, Tsuchiya, K. Fujioka and M. Takeuchi, 1999. Discrete Huygens' model approach to sound wave propagation?reverberation in a room, sound source identification and tomography in time reversal, *J. Sound & Vib.,* **225**(1), 61-78.

[10] Y. Kagawa, T. Fujitani, Y. Fujita, L. Chai, N. Wakatsuki and T. Tsuchiya, 2002. Discrete Huygens' modelling approach to wave propagations in a homogeneous elastic field, *J. Sound & Vib.,* **255**(2), 323-335.

[11] P.B. Johns and R.L. Beurle, 1971. Numerical solution of 2-dimensional scattering problems using a transmission-line matrix, *Procs. Inst. Elec. Eng.,* **118**, 1203-1208.

[12] P.B. Johns 1974. The solution of inhomogeneous waveguide problems using a transmission-line matrix, *IEEE Trans. Microwave Theory and Techniques, MTT*, **22**, 209-215.

[13] Y. Kagawa, N. Yoshida, T. Tsuchiya and M. Sato, 2000. Introduction to Equivalent Circuit Network Modelings, (Tokyo: Morikita-Shuppan) (in Japanese).

[14] J.A. Morente, J.A. Porti and M. Khalladi, 1992. Absorbing boundary conditions for the TLM method, *IEEE Trans. Microwave Theory and Techniques, MTT-* **40**(11), 2095-2099.

[15] L. Chai, S. Nogi, Y. Kagawa and N. Wakatsuki. 2005. Absorbing boundary conditions in Transmission-line Matrix (TLM) modelling, *J. Japan Society for Simulation Technology,* **24**(1), 59-65.

[16] C. Christopoulos, 1995. The transmission line modelling method, *IEEE Publications.*

[17] E.M. Viggen, 2009. The lattice Boltzmann method with application in Acoustics, Thesis, Dept. of Physics -NTNU.

[18] Renato S.T. de Carvalho, Julio A. Cordioli, 2016. Simulation of underwater acoustics and sediment wave propagation using the Discrete Huygens Modeling (DHM), *Proceedings of Forum Acusticum EAA Conference, Krakow,* pp. 1-8.

[19] A. Alia, 2018. Application of Discrete Huygens Method for Diffraction of Transient Ultrasonic Field, *Acoustical Physics,* 2018, **64**(1), 10-17.

Acoustic analyses of intonation in two dialects of Kannada - A comparative study

Theaja Kuriakose, Shridevi S Govanakoppa and Sangeetha V
JSS Institute of Speech and Hearing, Kelageri, Near Tapovana,
Sri Shivarathreeshwara Nagar, Dharwad-58007, Karnataka
crz148292@iitd.ac.in

ABSTRACT

Intonation refers to the change of fundamental frequency in a sentence. Intonation helps the speakers to express their ideas or emotions. There have been very limited studies to examine the effect of dialect in Intonation. The present study aimed to investigate and compare the terminal contour of intonation between Bangalore dialect Kannada and Dharwad dialect Kannada in sentences depicting various emotions. The results indicated differences in the intonation pattern between the dialects. The results also indicated presence of compound tone more in Dharwad dialect Kannada compared to Bangalore dialect Kannada.

1. INTRODUCTION

In human communication, prosodic features play an important role. These features make the system of communication productive and accurate. Prosody may reflect various features of the speaker or the utterance: the emotional state of the speaker; the form of the utterance (statement, question, or command); the presence of irony or sarcasm; emphasis, contrast, and focus; or other elements of language that may not be encoded by grammar or choice of vocabulary. The speech will sound monotone, if prosodic aspect of speech is affected. "Although much of the message in speech is conveyed by the segmental phonemes; additional information is carried out by the prosodic features"[1]. "Prosody may serve as the interface between low level segmental information and higher level grammatical structures in speech"[2]. Since, speech is considered as the primary mode of human communication, knowledge of prosodic features is essential to scientifically study the human communication and speech.

Intonation, rhythm and stress are classically understood as prosodic parameters. Intonation refers to the change of fundamental frequency in a sentence. Intonation helps the speakers to express their ideas or emotions .It is usually the terminal F0 pattern which varies across the different sentence types in non-tonal languages [3]. The study of intonation has attracted a great deal of scholarly attention, despite the difficulty in analysing this property of spoken language by the ear. Pattern of Intonation contour have been investigated in various Indian languages such as Kannada, Tamil, Gujarati and Hindi[4]. A pattern of a final fall (either a gradual or steep) was identified in sentence types such as neutral, jealousy, hesitation, request and for question, anger + question, frustration, accusation a final rise contour was identified in Kannada[5]. Studies on expression of emotions of anger, frustration, grief, joy, jealousy, neutral, surprise and worry were carried out in Tamil, Malayalam, Telugu and Bengali languages. It was found that, a final fall Fo pattern was

observed in most of the emotions in Tamil. However, the emotion fear was characterised by final rise pattern[6]. Intonation pattern of Malayalam and Telugu languages were characterised by final fall patterns for all types of emotions[7][8]. In Bengali, all emotions had terminal falling Fo patterns except for the emotions fear and surprise[9]. The intonation of various emotions such as anger, happiness, sadness and neutral in Punjabi language revealed raising Fo patterns for emotions with more excitement whereas the less excited emotion was spoken with falling contour.[10] But, these intonation patterns are not strictly universal. For example, exclamatory sentences had a raising pattern in Kannada and Konkani[3], which is a similar finding reported for English,[11] whereas, a falling pattern was seen for exclamatory sentences in Tulu. Similar results were reported in French and German respectively[12][13].

The terminal intonation patterns of different sentence types like declaratives, exclamatory, interrogatives, and imperatives were taken and recorded in three languages Kannada, Tulu and Konkani were examined[14]. F0 patterns showed that declaratives and imperatives had falling contours in all languages. Exclamatory sentences had raising contours in Kannada and Konkani, but falling contour in Tulu. Interrogatives had raising patterns across all languages, except for males in Kannada. The production of sentences in Kannada, Konkani and Tulu indicated differences in the terminal F0 pattern across the different sentence types.

A study done on Japanese and Russian languages reported that there is an increase in the height or magnitude of a rise for the intonation pattern of a declarative sentence in both languages[15]. For the language English there is a raising terminal contour in the exclamatory sentence[16].

A study on perceptual correlates of sentence-type intonation in French indicated that in French language declaratives and exclamatives were of falling intonation pattern, interrogatives were of rising and imperatives split between falling and rising contours depending on their specific functions[17]. Falling intonation is reported to indicate a declarative utterance, while a rising intonation contour declares an interrogative utterance in German[18].

Dialect is a particular form of a language which is peculiar to a specific region or social group. A study on the role of intonation in language and dialect discrimination by adults was examined[19]. In their study they investigated whether listeners are relying on pitch cues for language discrimination. They acoustically analyzed American English and German, and American and Australian English to demonstrate that these pairs are distinguishable using either rhythmic timing or pitch information alone. Then, American English listeners' ability to discriminate prosodically-similar languages was also examined using (1) low-pass filtered, (2) monotone resynthesized speech, containing only rhythmic timing information, and (3) re-synthesized intonation-only speech. Results showed that listeners can use only pitch cues to discriminate between American English and German. Additionally, although listeners are unable to use pitch cues alone to discriminate between American and Australian English, their classification of the two dialects is improved by the addition of pitch cues to rhythmic timing cues. They suggested that, the role of intonation cannot be ignored as a possible cue to language discrimination

The literature review suggests that there are many studies that have been carried out in intonation in various languages. However, limited studies have done to examine the intonation difference with respect to dialects. India is a multilingual country. Most of the Indian languages have different dialects and variations, sometimes very different from each other. Dialects of Kannada fall into four groups[20]. They are Coastal dialects, Northern Dialects, South-eastern Dialects and southern dialect. Prosodic variations have been well documented in many foreign languages across various dialects[21][22]. In Indian context, such studies are limited.

Need for the study - Studying intonation patterns in different dialects will help a speech language pathologist to understand the normal and abnormal aspects of prosody in a specific region or social group. This will further help in the assessment and management of prosodic errors in individuals with various speech and language disorders in a group of people belonging to a specific region. This would also shed

some light on the parameters of prosody that need to be incorporated for the synthesis of speech in the Indian languages. Several studies have been carried out to determine the intonation pattern in Kannada language. However no studies have been compared the intonation pattern between different dialects in Kannada. Hence the present study focused to determine the intonation patterns in Bangalore dialect Kannada and Dharwad dialect Kannada using acoustical methods in four different emotions such as 'happy', 'sad', 'anger' and 'question'.

Aim of the study-To investigate and compare the terminal contour of intonation between Bangalore dialect Kannada and Dharwad dialect Kannada in sentences depicting emotions such as 'happy', 'sad', 'anger' and 'question'.

2. METHODS

Development of the stimulus - Four sentences depicting emotions such as happy, sad, anger and question were chosen for the study and they were |ap‧a| |nangɛ| |h□sa| |bat‧ɛ| |k□dsɪd□ru|, |n∧n‧a| magangɛ| |kɪvɪnɛ| |kɛ:lɪst□ɪl‧a|, |nɪn‧a| |mukha| |nangɛ| |mat□□ɛ| |t□o:rɪsbɛda|, |ɪl‧ɪnd□a| |ɛʃtu| |d□u:ra| |ɪd□ɛ| |ma□isu:ru| respectively. All the sentences were having a mean length of utterance of about 4 to 5 words.

Stimulus recording - Two trained theatre artists were served as subjects for stimulus recording. The subject one was a native speaker of Kannada and from southern part (Bangalore) of Karnataka. The subject two was also native speaker of Kannada and he belonged to northern part (Dharwad) of Karnataka. The stimulus recording was carried out in a sound proof room. Before recording the stimuli both the subjects were seated comfortably and explained regarding the purpose of the study. Sony digital voice recorder was used for recording the stimulus and it was kept at a distance of approximately 5-6 inches away from the subjects mouth. The four sentences chosen for the study were then given to each of the subjects. The subject one was instructed to utter the sentences in the intended emotions thrice in Bangalore dialect Kannada and the subject two was also instructed to utter the sentences thrice in the intended emotions in Dharwad dialect Kannada. Hence a total of twenty four utterances depicting emotions such as 'happy', 'sad', 'anger' and 'question' were recorded out of which 12 sentences were in Bangalore dialect and 12 were in Dharwad dialect.

Perceptual evaluation - These recorded audio samples were given for perceptual evaluation to three experienced Speech- Language Pathologists and were instructed to rate the sample with respect to the intended emotion as good, average and poor. Based on the perceptual analysis rating, the investigator selected the best recording from each emotions in both Bangalore dialect and Dharwad dialect Kannada and these utterances were considered for further analysis .Thus the study included 8 sentences depicting emotions such as 'happy', 'sad', 'anger' and 'question' among which four sentences were uttered in Bangalore dialect Kannada and remaining four in Dharwad dialect Kannada.

Acoustic analysis - PRAAT software was used for the acoustic analysis. The highest and lowest F0 was noted in each sentence to calculate F0 range. The intonation contours were obtained by analysing the terminal syllable F0 contour for each sentence of Bangalore dialect Kannada and Dharwad dialect Kannada. A difference of 20 Hz or more between two levels was considered adequate for considering that as a rise or a fall and only change of less than 20 Hz was considered as steady[23]. For example the pitch curve extracted from praat software for the sentence "|nɪn‧a| |mukha| |nangɛ| |mat□□ɛ| |t□o:rɪsbɛda| as uttered by a subject one in south dialect is displayed below.

The PRAAT software enables simultaneous visualization of the fundamental frequency pattern for a given portion of speech signal, the intonation contours and also the waveform. A vertical cursor, which would be moved horizontally, was used to mark specific portion of the waveform, highlight and listen to the signal present in the marked portion of the waveform and by clicking the 'pitch' button the minimum fundamental Frequency (in Hertz), the maximum fundamental Frequency (in Hertz) and the average
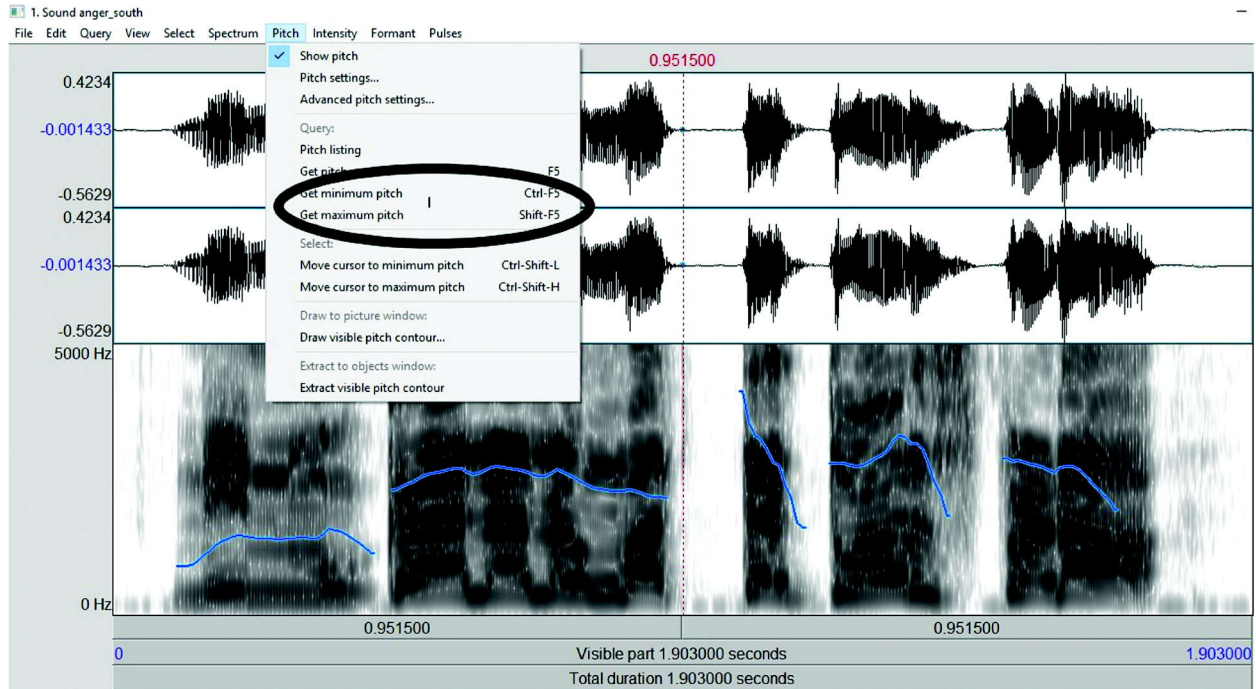
fundamental frequency (in Hertz) between these points could be noted as depicted in above figure. For each sentence, the range of frequency variations was calculated by subtracting the lowest frequency from the highest frequency. Thus the intonation contours obtained for all the sentences were compared to find out the intonation of utterances in each emotion of Bangalore dialect Kannada and Dharwad dialect Kannada.

3. RESULTS AND DISCUSSIONS

Acoustic analysis revealed differences in the intonation contours between Bangalore dialect and Dharwad dialect Kannada. Table 1 and Graph 1shows the F0 range of Bangalore dialect and Dharwad dialect Kannada.

Table 1. The F0 range of the emotions

Emotions	F0 Range	
	Dharwad dialect	Bangalore dialect
Anger	114 Hz	273 Hz
Happy	167 Hz	254 Hz
Question	121 Hz	126 Hz
Sad	92 Hz	100 Hz

Fo range was found to be higher for all the emotions in Bangalore dialect Kannada. This indicates more pitch variations in Bangalore dialect Kannada when compared to Dharwad dialect. The f0 range was found to be highest in emotion Anger in south dialect, whereas more difference in f0 range was found in the emotion Happy in Dharwad dialect Kannada. The lowest range of f0 was found in the emotion sad for both Bangalore and Dharwad dialect Kannada.

The results also indicated differences in intonation contours between Bangalore Dialect and Dharwad dialect Kannada in all the emotions. Table 2 shows the most common pattern and the terminal syllable intonation pattern for all the emotions considered in the present study in both the dialects.

Table 2. Most common pattern and the terminal syllable intonation pattern

Emotions	Most common pattern		Terminal syllable pattern	
	Dharwad dialect	Bangalore dialect	Dharwad dialect	Bangalore dialect
Anger	Fall	Fall	Flat	Fall
Happy	Rise-Fall	Fall	Rise-Fall	Rise
Question	Fall	Rise	Flat	Rise
Sad	Rise-Fall	Flat	Flat	Flat
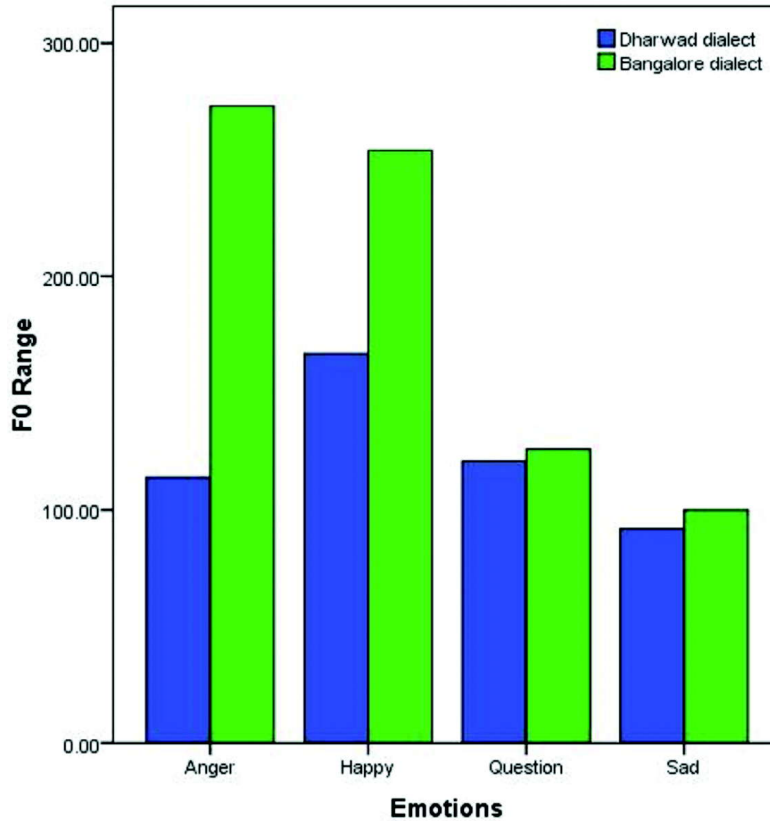
Graph 1: The F0 range of the emotions

For emotion Anger the most common contour was found to be falling in both Bangalore and Dharwad dialect Kannada, however the terminal syllable contour of final word in anger was found to be flat in Dharwad dialect and fall in Bangalore dialect Kannada. For the emotions happy and sad compound tone (rise, fall) was found in Dharwad dialect Kannada. Whereas the Bangalore dialect Kannada showed the most common intonation contours of fall and flat for the emotions happy and sad respectively. A falling pattern was found in the emotion 'question' in Dharwad dialect Kannada and a rising pattern was found in Bangalore dialect Kannada.

The results yielded many points of interest. Firstly, the results of acoustic analysis indicated the presence of compound tones to be more in Dharwad dialect when compared to Bangalore dialect Kannada. Second, there were variations observed in the terminal syllable of each utterance between the dialects in all emotions except for sad, where it was found to be flat in both the dialects. Finally, the range of pitch variation over the utterances was found to be more in Bangalore dialect than Dharwad dialect Kannada.

4. CONCLUSION

The present study attempted to investigate and compare the intonation contours in four types of emotions such as 'happy', 'sad', 'anger' and 'question' between Bangalore dialect and Dharwad dialect Kannada using acoustical methods. The results indicated differences in the intonation pattern between the dialects. The results also indicated presence of compound tone more in Dharwad dialect Kannada compared to Bangalore dialect Kannada. However the results can be generalized only with larger samples.

Studying the aspects of intonation patterns in different dialects provide an understanding of normal and abnormal aspects of prosody in a specific region or social group to a Speech Language Pathologist. It is essential to know the normal prosodic aspects for assessment and management of individuals with prosodic impairment. This also provides information for synthesising speech for various research purposes.

5. REFERENCES

[1]   W. A. Anisworth, 1976. *Perception of prosodic features*. Terhaar (Ed), London: Pergamon Press

[2]   L. Pisoni and Saweesh, 1975. Intonation in Kannada. In Manjula, R. *Unpublished Master's Dissertation*, University of Mysore.

[3]   M. M. Mathew and J. S. Bhat, 2010. Nature of Sentence Intonation in Kannada, Tulu and Konkani. *Language in India,* **10**, 15-25.

[4]   N. P. Nataraja, 1981. Intonation in four Indian languages under five emotional conditions. *Journal of AIISH,* **12**, 22- 27.

[5]   H. N. Nandini, 1985. Some prosodic aspects in Kannada. *Research at A.I.I.S.H*: Dissertation Abstracts, 82, Vol II. (D 134).

[6]   M. J. Varshini and N. P. Nataraja, 2000. Some aspects of intonation in Tamil. *Dissertation submitted to University of Mysore,* Mysore.

[7]   N. Mini and N. P. Nataraja, 2000. Intonation in Malayalam- Some aspects. Research at A.I.I.S.H, *Dissertation Abstracts,* **IV**, 90-91 (D 402).

[8]   C. S. Sandhya and N. P. Nataraja, 2000. Intonation in Telugu- Some aspects. Research at A.I.I.S.H, *Dissertation Abstracts,* **IV**, 90-91 (D 401).

[9]   S. Saha and N. P. Nataraja, 1999. Intonation in Bengali- some aspects. Research at A.I.I.S.H, *Dissertation Abstracts,* **IV**, 82 (D 396).

[10]   H. Dawood, R. Shahid and R. Touqeer, 2004. *From Annual Report*: Intonation Patterns in Punjabi. from http://www. crulp.org/research/reports/streport/

[11]   D. Bolinger, 1972. *Intonation: Selected readings. England*: Penguin Books Ltd.

[12]   D. Bassano and M. I. Mendes, 1994. Perceptual correlates of sentence-type intonation in French. *Journal of Phonetics,* **44**, 132-144.

[13]   V. Raithel and M. F. Hielscher, 2004. Emotional and linguistic perception of prosody. *Folia Phonatrica logop*, **56**, 7-13.

[14]   Mili Mary Mathew and Jayashree S. Bhat, 2010. Nature of Sentence Intonation in Kannada, Tulu and Konkani. *Language in India,* **10**(11), 15-25.

[15]   V. Markowa, 2000. Perceptual correlates of sentence type intonation in Russian & Japanese. *Journal of phonetics,* **29**(2), 137-154.

[16]   D. Bollinger, 1972. Intonation: selected readings. England: Penguine Books Ltd.

[17]   D. Bassano and M. I. Mendes, 1994. Perceptual correlates of sentence-type intonation in French. *Journal of phonetics,* **44**, 132-144.

[18] V. Raithel and M. F. Hielscher, 2004. Emotional and linguistic perception of prosody. *Folia Phonatrica logop,* **56**, 7-13.

[19] Chad Vicenik and Megha Sundara, 2013. The role of intonation in language and dialect discrimination by adults. *Journnal of phonetics,* **41**(5), 297-306.

[20] Michail Andronov, 2003. A comparative grammar of the Dravidian languages. Harrasowitz Verlag. Wiesbaden.

[21] J. I. Hualde, G. Elordieta, I. Gaminde and R. Smiljanic, 2002. From pitch-accent to stress-accent in Basque and the typology of accentual systems. In: Gussenhoven C, Warner N, editors. *Papers in Laboratory Phonology*. Cambridge University Press; Cambridge. **7**, 547-584.

[22] J. Bishop and J. Fletcher, 2005. Intonation in six dialects of Bininj Gun-wok. In: Jun S-A, editor. *Prosodic Typology*. Oxford University Press; New York. pp. 331-361.

[23] Rajesh, 1998. Analysis of prosodic aspects aspects of Kannada - In hearing impaired children. *Unpublished Master's Dissertation*, University of Myosre.

Development of multi-channel data logger for passive acoustic measurements

William A. Fernandes*, Yogesh Agarvadekar and Bishwajit Chakraborty
CSIR-National Institute of Oceanography
Dona Paula, Goa. 403004
william@nio.org

ABSTRACT

Recording of passive acoustic data involves a listening device along with an instrumentation system. The passive listening device transforms mechanical disturbances to electrical signals. The subsequent sampling and logging of the transformed data is accomplished by employing the instrumentation system. One such system is the Low cost "Multi-Channel Data Logger" (MCDL) that is indigenously developed at CSIR-National Institute of Oceanography with a capability to record 8- channels of passive acoustic signals simultaneously. Here we have presented the designed and developed MCDL system interfaced with a six channel hydrophone array to log ambient noise data from the underwater environment and also connected with dual low cost high sensitivity microphones for recording terrestrial ambient noise signals. The laboratory tests & field trials along with the data analysis results are presented to demonstrate the MCDL's multi-platform functionality.

1. INTRODUCTION

In marine environment the sound signals are generated by various sources (surface as well as undersea) and are collectively called as marine ambient noise (AN). AN is sometimes classified as geo-phonic, bio-phonic and anthro-phonic. These underwater ambient noise signals may travel longer distances and therefore can be studied for number of applications such as underwater object detection, tracking of marine habitats and identification etc. Moreover, the terrestrial applications include forest soundscape studies using animal/bird sounds, for species identification, quantification studies and protection. The birds migrate due to the effects of climate change, reaching at their breeding grounds sooner as global temperature rise[1]. Hence birds migration pattern does provide the signatures of climate change. However, long term monitoring of environmental parameters may be used for climate research[2]. The Study of traffic and pollution data can be used to comprehend the environmental parameters. All the above mentioned research studies can be undertaken by implementing economically low cost data loggers within the region of interest.

In this work, we present the low cost Multi-channel Data Logger (MCDL) system and the passive acoustic data acquired from laboratory tests to field trials held within the Goan boundaries, along with a demonstration data recorded at Radhanagri wildlife sanctuary, Maharashtra. It may be stated here that the developed low cost instrumentation system can be employed at different locations for monitoring species (marine as well as terrestrial) and also the marine traffic by utilizing multi-channel facility of the MCDL.

---

2. MATERIALS

The self contained battery operated autonomous Multi-Channel Data Logger (MCDL) designed around Teensy 3.6 cortex-M4F ARM (Advanced RISC Machine) processor board (www.pjrc.com). The Teensyduino software provides integrated support for Teensy microcontrollers within Arduino IDE software platform by adding microcontroller specific libraries and the compiled program download utility that loads the program to the microcontroller memory. The C program compiled either on Linux using GNU gcc compiler or Windows is utilized to convert the recorded binary formatted data to ASCII file format. The microcontroller is interfaced with 8- channel Successive Approximation Register (SAR) - Analog to Digital Converter (ADC) using byte transfer mode that transfers data from ADC to microcontroller. At the time of acquisition every sample ensemble of 8- channels, 16 bytes are transferred from ADC to microcontroller. In this mode a sampling rate of 100 kHz was obtained. The MCDL block diagram demonstrates the total system functioning protocol (fig.1). The system is powered through 8D cells each of 1.5V alkaline batteries having total capacity of 7.2AH, may provide approximately 40 hours of continuous sampling of 8 channels at a maximum sampling rate of 100 kHz. In active mode, it consumes maximum of 150 mA, while the sleep mode consumption is less than 0.5 mA approximately.
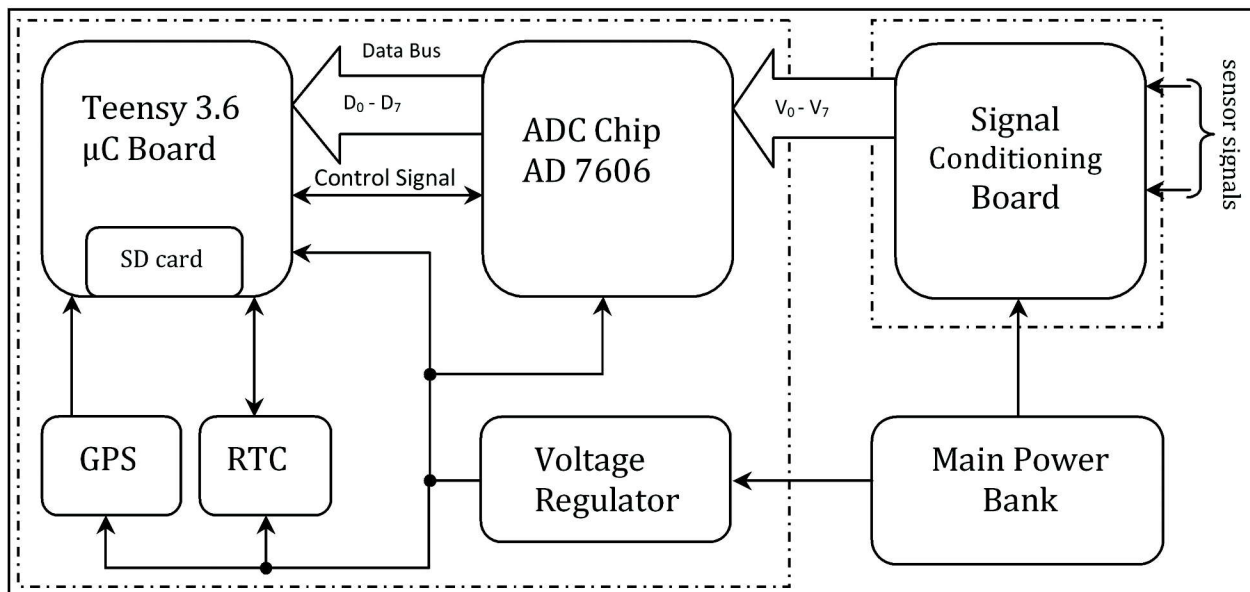

Fig. 1. Showing MCDL functional block diagram

For field trials and the demonstration, the sample rate of 25kHz was preferred for recording of bio-phonic and anthropogenic process generated acoustic signals. The marine AN data was acquired using single wideband C55 hydrophone (www.cetaceanresearch.com) for sampling duration of 30 seconds in every 1 minute. However, the laboratory test data was acquired for duration of 10 seconds in every 1 minute. The terrestrial ambient noise was also recorded by interfacing locally available low cost high sensitivity condenser microphones with the above mentioned configuration. The system is designed for short term deployments, however long term monitoring is also possible by upgrading the main power bank and its casing. The signal conditioning card consists of eight dual op-amps pairs configured in DC servo amplifier mode to enhance the electrical signal and to reduce the possibility of noise contamination from ancillary environmental factors. The precision Real-Time Clock (RTC) is provided to monitor sampling and recording time intervals together with time stamping the data. The precision RTC is synced with GPS time in every 24 hrs. During acquisition, the incoming signals are sampled, digitized and stored in the storage media of size 64 GB (upgradable up to 128 GB). The system features flexible and user customizable

configuration with sample rates as high as 100 kHz with a file size of 96 MB for 60 seconds. The main 16-bit logger board along with GPS, signal conditioning and main power bank are packed in water proof enclosure. The water-proof interface is also provided on the enclosure. The system is fully water-tight and therefore can be installed on any fixed/floating platform for the acquisition of AN data.

3. METHODS

After successful initial tests of the MCDL system that were carried out by interfacing sine signals to each channel, the laboratory tests were performed, interfaced with single wideband C55 hydrophone deployed in water contained glass aquarium of dimension 50 cm × 25 cm × 25 cm approximately. The aerator was installed and adjusted to generate air-bubbles in water medium, producing signals that are transformed and stored within the logger memory. During second phase of testing at the pool site, the Vertical Linear Array (VLA) of 6-channel hydrophones together with dual microphones were connected to MCDL for a short period of time, so as to check system's versatility. However, during tests and trials, the data was acquired leaving unused channels opened. The field trial at Dona Paula jetty was executed by interfacing single wideband C55 hydrophone (leaving unused channels opened), deployed at 2.5 m below the water surface and configured to record 30 seconds of sampled data at 25kHz for every 1 minute. However due to shallower depths and higher currents at Cortalim jetty, the hydrophone depth was limited to 1.5 m approximately.

Subsequently, the system demonstration was also arranged in the month of March, 2017 at Radhanagri wildlife sanctuary to study forest soundscape by capturing terrestrial ambient noise (birds, animals and wind generated sounds) data employing low cost higher sensitivity microphones. At dusk, the MCDL was placed at the irrigation department guest house with in the sanctuary with the intention to record early morning bird sounds, but the cricket chorus sound was evident during the period. However, at dawn many birds sound signals were observed. The marine AN data was also logged (as a part of the demonstration) by interfacing single wideband C55 hydrophone, placed approximately at 1 meter below the water surface in the Radhanagri dam for a short span of time. The analyses of the logged data were performed by utilizing Matlab (www.mathworks.com) computational platform employing basic signal processing tools.

4. RESULTS AND DISCUSSIONS

The design of 16-bit MCDL composed of integrated sensor (channel) interface, ADC & signal conditioning circuit board along with Teensy 3.6 cortex-M4F ARM micro-controller and storage. The system utilizes 8- channel SAR - ADC that employs byte transfer mode for data transfer from ADC to microcontroller. At the time of acquisition every sample ensemble of 8- channels, 16 bytes are transferred from ADC to microcontroller. In this mode a sampling rate of 100 kHz was obtained. The system has better features particularly towards sample rates, data storage capabilities and improved signal conditioning per channel. The configuration (config.txt) file is simple text format file that holds the settings (File prefix; sampling interval; sample rate; recording interval) and can be easily altered by the user using available text editors. However in the present data, the configuration file was set as per the requirement and unaltered for most of the tests except for file prefix & sampling interval. The MCDL is powered through 8 D cells each of 1.5V alkaline batteries having total capacity of 7.2 AH. In active mode, it consumes maximum of 150 mA, while the sleep mode consumption is less than 0.5 mA approximately. The system presently provides 64 GB microSD card (data storage media) that may be upgradable upto 128GB. Moreover it features flexible and user customizable configuration with sample rates as high as 100 kHz with a file size of 96 MB for 60 seconds.

The analyses of the data recorded in laboratory condition have shown the train of bubble blast sound signals Fig. 2(a). The spectrogram i.e., Short Time Fourier transform (STFT) of the laboratory recorded time series acoustic data acquired using the Multi-Channel Data Logger is presented in Fig. 2(b) in
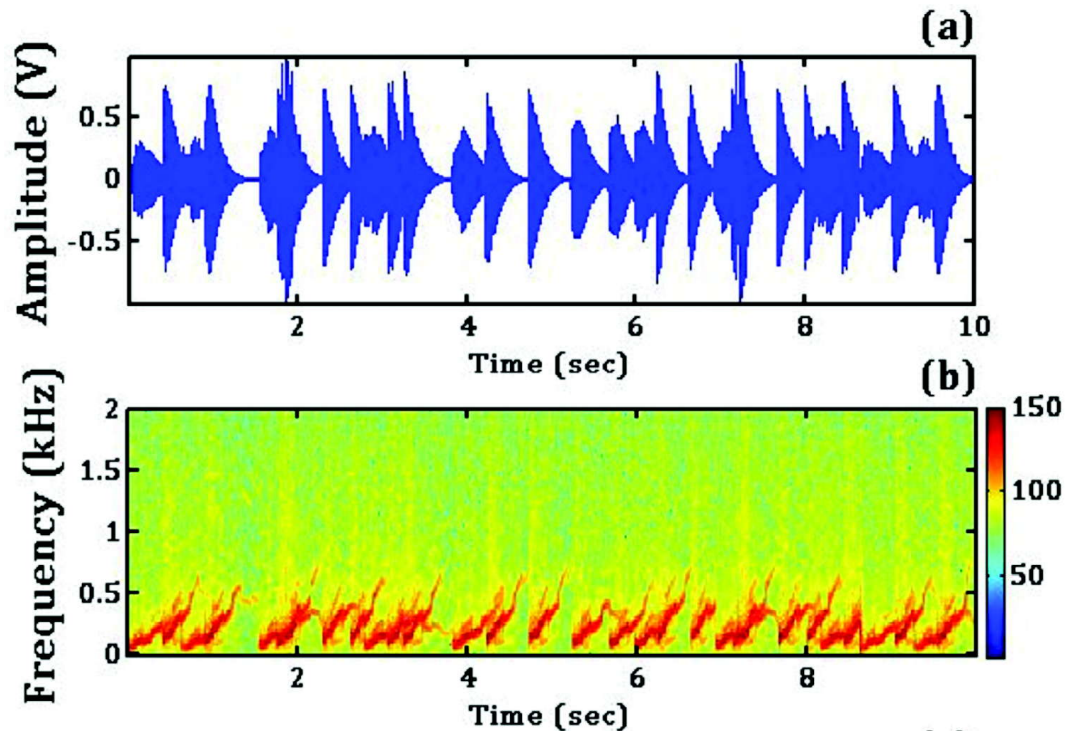
Fig. 2. Showing (a) Time series and (b) frequency spectrum of the bubble
blast sounds recorded in laboratory

terms of frequency (Hz) versus time (sec). Higher signal strengths of 132.7 dB are observed at 147 Hz. It was also observed that varying the bubble size produces variation in the signal strengths and also to its peak frequency[3]. In the second phase of testing, the MCDL was operated with an VLA of 6-hydrophones and dual microphones as an experiment to record underwater as well as land based AN signals. The logged array data have not shown much variations, however the microphones have recorded human talks and bird chorus.

The AN data acquired during field trials at Dona Paula jetty has shown jet skis underwater broadband sound signal, overlain with harmonically related tonals (ranging from 300 Hz to 5kHz that can be seen from Fig. 3(b)[4] and also the snapping shrimp noise, which is a dominant source of mid- frequency ambient noise[5]. The trial data recorded at Cortalim floating jetty has provided indication of piling information which was from the piling station positioned diagonally (~500 m) across the Zuari river banks, having signal strengths of 133 dB at the lower frequency of 48.83 Hz, observed through spectrogram (STFT) and Welch's power spectral density estimate (Fig. 4)[6]. Furthermore the demonstration data acquired at Radhanagri wildlife sanctuary, has shown significant improvement in capturing birds sound signals despite of rough windy conditions[7]. Moreover, the logged data have revealed the low amplitude signatures from birds which were otherwise ignored due to heavy noise induction. As it was equipment demonstration, other parameters were not necessary and hence the spot weather data was not collected. The terrestrial ambient noise data recorded at other locations within the Sanctuary, provided better results due to stable weather conditions or may be for the reason that the system installation was at lower elevation (Fig.5). However the source identification is not the purpose of this study. The recorded ambient noise during the transition period from dusk to night, the cricket noise signal was observed [8 & 9]. The cricket generates the sound pulse by the effect of scissoring movements of the two wings having a series of harmonically related frequency components that were noticed at 3.5 kHz, 6.7 kHz and 10.4 kHz (fig. 6)[8]. However the peak of the spectrum was found to be at 6.7 kHz.
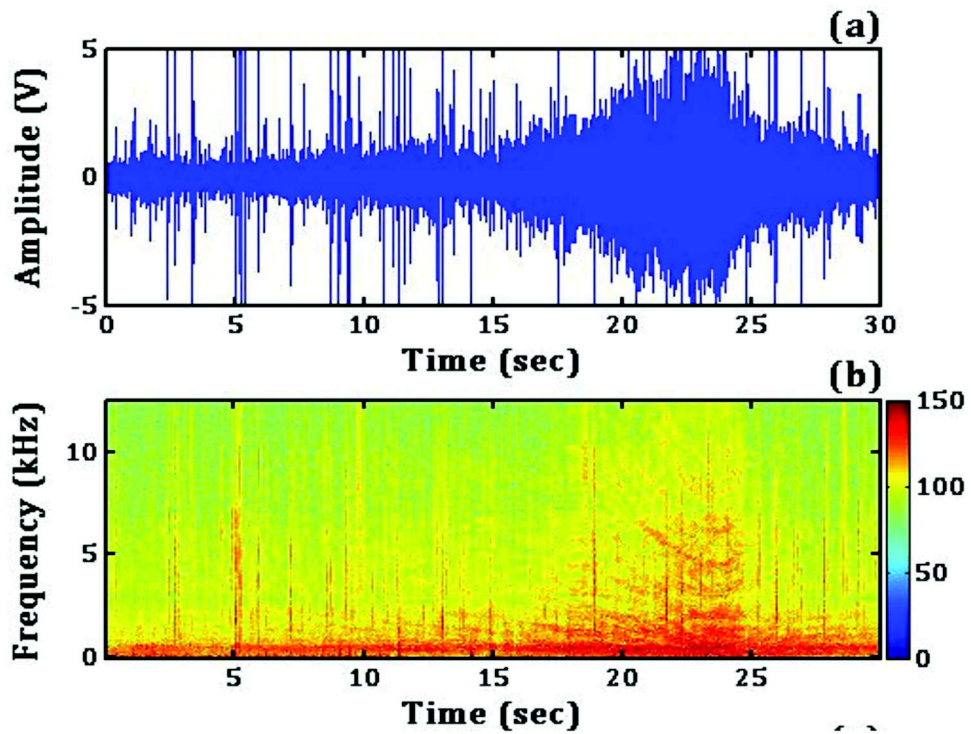
Fig. 3. Showing (a) Time series and (b) frequency spectrum of the Jet skis recorded at Dona Paula jetty
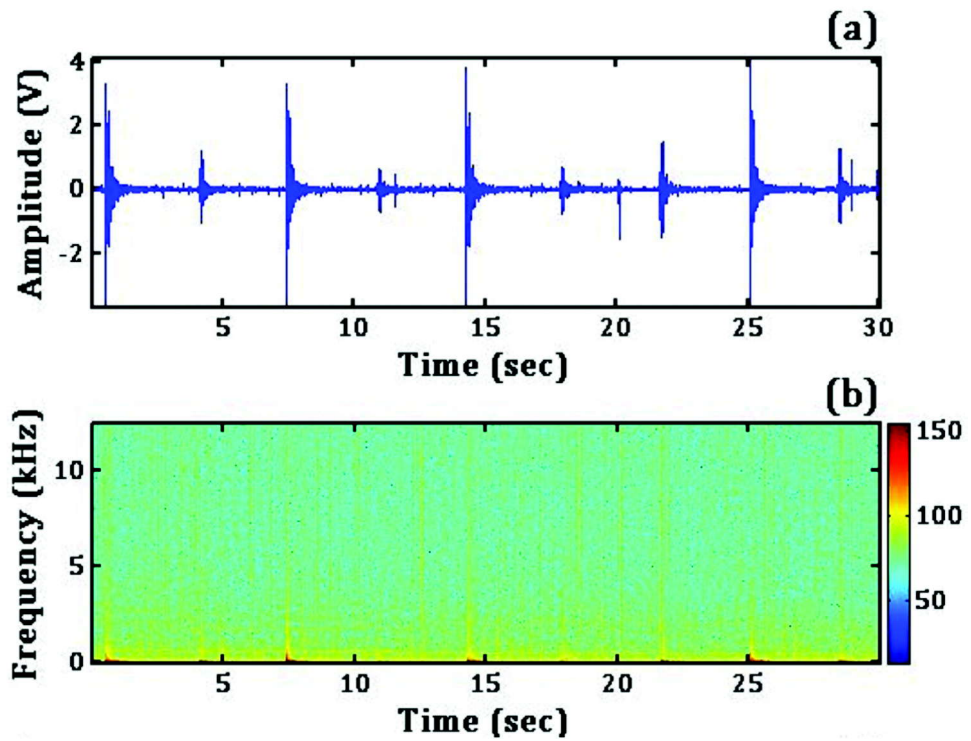
Fig. 4. Showing (a) Time series (b) frequency spectrum of the pile driving
noise signals recorded at Cortalim private jetty

William A. Fernandes, Yogesh Agarvadekar and Bishwajit Chakraborty
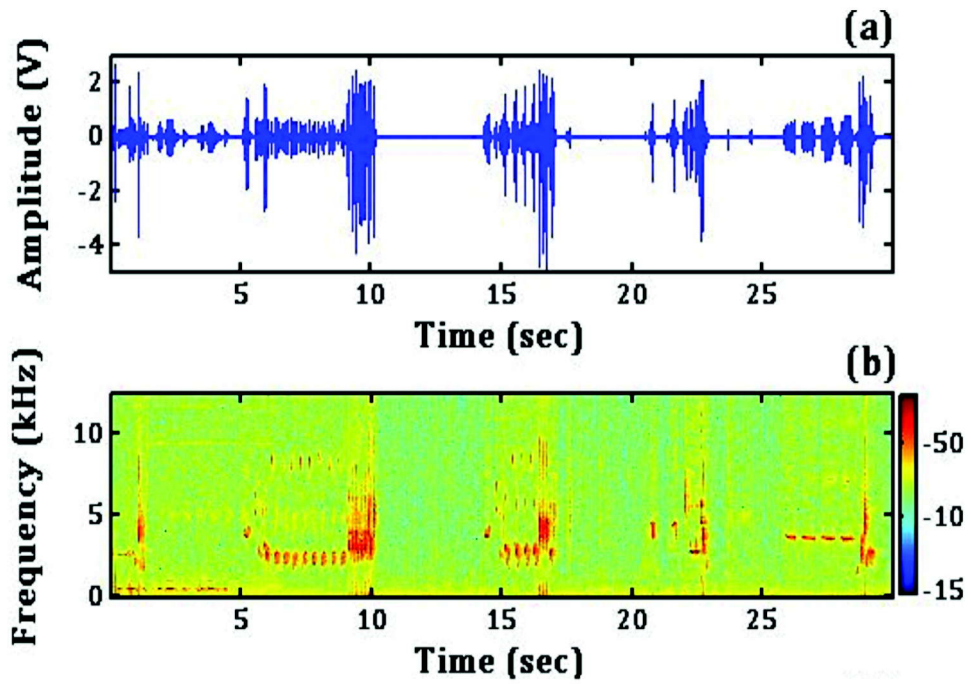
Fig. 5. Showing Time series & Frequency Spectrum of the small farm birds sound signal acquired at Irrigation department guest house, Radhanagri

Fig. 6. Showing Time series & Frequency Spectrum of the cricket sound signal acquired at Irrigation department guest house, Radhanagri

5. CONCLUSION

In this study , we presented indigenously developed Multichannel Data Logger (MCDL) that was employed to acquire AN data at various locations. The results were demonstrated through specified figures. The VLA of 6-channel hydrophones together with dual microphones were connected to check MCDL's flexibility in recording 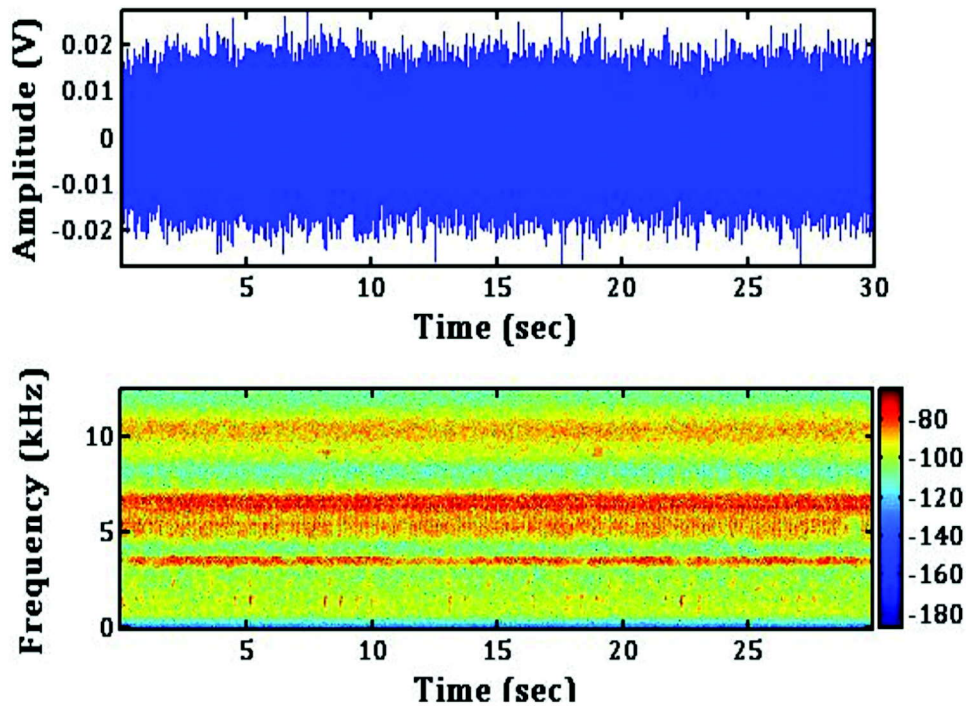underwater as well as land based AN signals, however logging of weather data was not attempted. The SAR-ADC & signal conditioning board has provided better results as can be seen from the figures (oscillograms and spectrograms). The AN data acquired during system demonstration at Radhanagri wildlife sanctuary have shown the evidence of small farm birds. Additionally, the cricket noise sounds were also observed. Finally, the results have illustrated that the system is capable of recording quality data under the effects of moderate weather conditions.

6. ACKNOWLEDGMENT

7. REFERENCES

[1]   E. Lehikoinen, T. H. Sparks, A. P. Møller, W. Fiedler and P. Berthold, 2010. "Changes in migration, Birds and limate change", *Oxford: Oxford University Press,* pp 89-112.

[2]   N. Rubolini, N. Saino and A.P. Møller, 2010. "Does migratory behaviour constrain the phenological response of birds to climate change?", *Clim Res*, **42**, 45-55.

[3]   S. Husin, A. Addali and D. Mba, 2011. "Acoustic frequency for bubble size correlation using acoustic emission", *Sixth International Conference on Computational and Experimental Methods in Multiphase and Complex Flow*, At Kos, Greece.

[4]   Christine Erbe, 2013. "Underwater noise of small personal watercraft (jet skis)" *J. Acoust. Soc. Am.* **133**, EL326.

[5]   John A. Hildebrand, 2009. "Anthropogenic and natural sources of ambient noise in the ocean" *Marine Ecology Progress Series,* **395**, 5-20.

[6]   Donatas Bagočius, 2015. "Piling underwater noise impact on migrating salmon fish during Lithuanian LNG terminal construction (Curonian Lagoon, Eastern Baltic Sea Coast)", *Marine Pollution Bulletin*, **92**, 45-51.

[7]   C. M. Harris, 1966."Absorption of sound in air versus humidity and temperature", *J Acoust Soc Am,* 40, 148-159.

[8]   Gerald Pollack, 2014. "Cricket acoustic communication", *Scholarpedia*, **9**(2), 11999.

[9]   J.-F. Augoyard, 1998. "The cricket effect. Which tools for the research on sonic urban ambiences?", "*Stockholm, Hey Listen*!" Conference, Royal Swedish Academy of Music.

Studies of ultrasonic and acoustic parameters of copper (II) surfactant of mustard and groundnut oils treated at different temperatures

Renu Bhutra[1], Rashmi Sharma[2] and Arun Kumar Sharma[3,*]
Department of Chemistry
[1]Rajesh Pilot Govt. Polytechnic College, Dausa-303303, Raj., India
[2]S.P.C. Govt. College, Ajmer-305001, Raj., India
[3]Govt. P.G. College Jhalawar-326001- Raj India
sharmaarun423@gmail.com

ABSTRACT

Colloid chemical behavior and micellar characteristics of Cu (II) soaps derived from mustard and groundnut oils, (fresh oils and treated with 15 and 60 min.) at high temperature in benzene have been investigated and verified by ultrasonic velocity measurement. From these values, various acoustic parametershave been calculated. The results have been analyzed byMasson equation. The results have been explained on the basis of solute-solvent interactions. The decrease in β and L_f with increasing concentration of the complex is indicating that there is sufficient solute- solvent interaction due to which micellar alignment is considerably affected.

1. INTRODUCTION

Now a day ultrasonic is considered to be a powerful tool in research activity in various fields. Ultrasonic investigations have established its versatility to furnish information as to the understanding of solute-solvent interaction. A number of workers[1-5] have discussed the physico-chemical aspects of ultrasonic velocity and related parameters. The Gruneisen parameter and internal pressure obtained from ultrasonic velocity and density data play a significant role in understanding internal structure, clustering phenomenon and quasi-crystalline nature of binary mixture[6-10]. Ultrasonic measurements have also been used to determine solvation number in aqueous media[11-13]. Ultrasonic investigation of liquid mixture have significant importance in understanding intermolecular interaction between the component molecules as that finds application in several industrial and technological processes[14-15]. Derived parameters from ultrasonic velocity measurements provide qualitative information regarding the nature and strength of molecular interactions in liquid mixtures[16-17]. The present work deals with the determination of ultrasonic velocity measurements which have been used to obtain information regarding various acoustic parameters and solute-solute interactions of copper (II) surfactants of mustard and groundnut oils (fresh oils and treated with 15 and 60 min.) at high temperature in non-aqueous solvent benzene at 303.15 K to access the effect of solvent molecules on the micellar nature of solute molecule[18-19]. The studies have also been done to understand the nature of the solution and observed that the increase in the internal pressure and in lowering the compressibility of the solution. The studies were done in non-aqueous solvents (benzene) to access the

effect of the micellar nature of solute molecule and solute-solute interactions. Because the synthesized compound is maximum soluble in benzene. This information is of fundamental importance for understanding solute-solute, solute-solvent interactions in solutions below and above critical micelle concentration and the structural aspects of the micelle. It is anticipated that it will generate a new hopes in various industrial and analytical applications of the newly synthesized surface active agrochemicals.

2. EXPERIMENTAL

All the chemicals used were of LR/AR grade. Copper soap was prepared by earlier reported methods [20]. All the soaps are stable at room temperature, their physical parameters and composition of oils are discussed in Table -1-2. The Cu (II) soaps are abbreviated as follows:

1. Copper - Mustard soap (CM)
2. Copper - Groundnut soap (CG)
3. Copper - Mustard soap treated for 15 min at high temperature. (CM_{15})
4. Copper - Groundnut soap treated for 15 min at high temperature. (CG_{15})
5. Copper - Mustard soap treated for 60 min at high temperature. (CM_{60})
6. Copper - Groundnut soap treated for 60 min at high temperature. (CG_{60})

Ultrasonic interferometer from Mittal Enterprises, Model M-82 with accuracy of $\pm$ 0.03% was used for the measurements of ultrasonic velocities in various solutions at a fixed frequency 2MHz. Water maintained at 303.15 K temperature in a thermostat was passed through the jacket of the cell before the measurement was actually made. The total distance d (1 cm) and wavelength λ are co related by following relation:

$$\lambda = 2d/n \tag{1}$$

The ultrasonic velocity U in the solution can be calculated by following relation:

$$U = \lambda \times f \tag{2}$$

3. RESULTS AND DISCUSSIONS

3.1. Acoustic parameters

Ultrasonic investigations have important parameter to understanding of solute - solvent interactions. A

Table 1. Fatty acid composition of oils used for Copper Soap synthesis

Name of oil	% Fatty Acids					
	16:0	18:0	18:1	18:2	18:3	Other Acids
Groundnut Oil	10	4	61	18	-	C_{20}-C_{24} 7%
Mustard Oil	2	1	25	18	10	C_{20}-C_{22} 41%

Table 2. Analytical and physical Data of Copper Soaps derived from treated and untreated oils

Name of Copper Soap	Color	Melting point (in °C)	Yield %	Metal %		S.V.	S.E.	Average Mol. Wt.
				Found	Calculated			
CG	Green	98	70	10.15	9.724	188.70	297.29	656.08
CM	Green	92	72	9.58	9.110	175.80	319.10	699.72
CG_{15}	Green	105	75	11.90	11.936	238.40	235.31	532.12
CM_{15}	Green	84	74	12.48	12.549	266.47	210.53	482.56
CG_{60}	Green	68	76	13.59	13.744	280.00	200.35	462.20
CM_{60}	Green	61	78	12.96	13.138	260.00	215.76	493.03

number of workers have discussed the physicochemical aspects of ultrasonic velocity and related parameters. It has been used to determine the solvation number[21].

The specific acoustic impedance Z, adiabatic compressibility β, intermolecular free length L_f, apparent molar compressibility ϕ_k, molar sound velocity R and primary solvation number S_n have been calculated by using the following relationships[22].

$$Z = U\rho \tag{3}$$

$$\beta = \frac{1}{U^2\rho} \tag{4}$$

$$L_f = K\sqrt{\beta} \tag{5}$$

$$\phi k = \left[1000.\frac{\beta\rho_0 - \beta_0\rho}{c\rho_0}\right] + \frac{\beta M}{\rho_0} \tag{6}$$

$$R = M.(U)\rho_0 \tag{7}$$

$$M = X_1 M_1 + X_2 M_2 \tag{8}$$

$$Sn = \left[\frac{n^0}{n}\right].\left[1 - \frac{V\beta}{n^0 V^0 \beta^0}\right] \tag{9}$$

Where β_0, β, d_0, d, n_0, n, $\bar{V}_0$ and $\bar{V}$ are adiabatic compressibility, density, number of moles and molar volume of solvent and solute solution respectively. The molar volume of the solvent $\bar{V}_0$ and soap solution $\bar{V}$ may be written as:

$$\bar{V} = X_1 M_1 + X_2 M_2 / \rho \tag{10}$$

$$\bar{V}_0 = X_1 M_1 + X_2 M_2 / \rho_0 \tag{11}$$

In equations (10) and (11) M equal to the molecular weight of component and X the mole fraction of the component and subscript 1 and 2 represents to solute and solvent respectively.

The experimental values of u and other parameters for Cu (II) soaps of untreated oils, treated oils for 15 minutes and treated oils for 60 minutesare recorded in Table-(3-8). The data clearly indicate that the values of u, Z, ϕ_k, S_n and R increase whereas the values of β and L_f decrease consistently with increase in the soap concentration. The increase in ultrasonic velocity may be attributed to the solute-solvent interaction. The increase in the values of specific acoustic impedance Z with soap concentration c due to lyophobic interaction between soap and solvent molecules, which increases the intermolecular distance between the molecules and main cause of propagation of ultrasound waves [23].

Table 3. Ultrasonic velocity and other acoustic parameter of copper soap derived from untreated Groundnut oil. (CG)

c (mol l^{-1})	ρ (g dm^{-3})	u (m s^{-1})	Z ×10^{-5} (g cm^{-2} s^{-1})	β_{ad} × 10^{11} (cm^2 dyne^{-1})	L_f (A°)	$-\phi_k$ × 10^8	R × 10^{-2}	S_n × 10^{-3}
0.0015	0.8693	1278.0	1.1109	7.0437	0.5296	58.861	45.241	-18.512
0.0031	0.8696	1282.1	1.1148	6.9966	0.5278	42.853	45.322	-9.178
0.0038	0.8697	1284.1	1.1168	6.9730	0.5269	39.656	45.361	-7.312
0.0077	0.8699	1288.2	1.1207	6.9264	0.5252	23.490	45.512	-3.633
0.0115	0.8694	1294.5	1.1255	6.8637	0.5228	18.969	45.727	-2.401
0.0153	0.8696	1298.7	1.1293	6.8182	0.5210	15.928	45.884	-1.790
0.0230	0.8700	1302.9	1.1335	6.7712	0.5192	11.012	46.144	-1.189
0.0306	0.8706	1307.2	1.1380	6.7222	0.5174	8.684	46.390	-0.888
0.0383	0.8709	1311.5	1.1421	6.6763	0.5156	7.132	46.655	-0.708
0.0459	0.8714	1315.8	1.1466	6.6283	0.5137	6.193	46.905	-0.588

Table 4. Ultrasonic velocity and other acoustic parameter of copper soap derived from untreated Mustard oil. (CM)

c (mol l^{-1})	ρ (g dm^{-3})	u (m s^{-1})	$Z \times 10^{-5}$ (g cm^{-2} s^{-1})	$\beta_{ad} \times 10^{11}$ (cm^2 dyne^{-1})	L_f (A°)	$-\phi_k \times 10^8$	$R \times 10^{-2}$	$S_n \times 10^{-3}$
0.0014	0.8691	1282.1	1.1142	7.0006	0.5280	91.90	45.302	-19.598
0.0029	0.8693	1292.4	1.1235	6.8871	0.5237	83.068	45.459	-9.588
0.0036	0.8695	1294.5	1.1255	6.8635	0.5228	72.216	45.497	-7.637
0.0072	0.8697	1298.7	1.1295	6.8172	0.5210	40.045	45.649	-3.794
0.0108	0.8699	1305.1	1.1353	6.7492	0.5184	31.271	45.828	-2.502
0.0144	0.8704	1307.2	1.1378	6.7236	0.5174	24.060	45.944	-1.872
0.0215	0.8710	1311.5	1.1422	6.6755	0.5156	16.580	46.197	-1.243
0.0287	0.8715	1315.8	1.1468	6.6273	0.5137	12.854	46.448	-0.928
0.0359	0.8722	1320.1	1.1515	6.5785	0.5118	10.661	46.693	-0.739
0.0430	0.8730	1324.5	1.1563	6.5297	0.5099	9.201	46.937	-0.613

Table 5. Ultrasonic velocity and other acoustic parameter of copper soap derived from treated Groundnut oil for 15 Minute (CG$_{15}$)

c (mol l^{-1})	ρ (g dm^{-3})	u (m s^{-1})	$Z \times 10^{-5}$ (g cm^{-2} s^{-1})	$\beta_{ad} \times 10^{11}$ (cm^2 dyne^{-1})	L_f (A°)	$-\phi_k \times 10^8$	$R \times 10^{-2}$	$S_n \times 10^{-3}$
0.0019	0.8691	1273.9	1.1071	7.0904	0.5313	22.23	45.202	-15.225
0.0038	0.8696	1278.0	1.1112	7.0416	0.5295	22.88	45.271	-7.545
0.0047	0.8699	1280.0	1.1135	7.0163	0.5285	23.42	45.299	-6.006
0.0094	0.8700	1286.2	1.1190	6.9481	0.5260	16.90	45.476	-2.972
0.0141	0.8702	1290.3	1.1228	6.9023	0.5242	13.15	45.628	-1.969
0.0188	0.8707	1294.5	1.1271	6.8541	0.5224	11.53	45.764	-1.466
0.0282	0.8716	1298.7	1.1319	6.8028	0.5204	8.32	45.988	-0.973
0.0376	0.8723	1302.9	1.1365	6.7529	0.5185	6.64	46.219	-0.726
0.0470	0.8730	1307.2	1.1412	6.7038	0.5166	5.60	46.455	-0.578
0.0564	0.8737	1311.5	1.1458	6.6546	0.5147	4.91	46.688	-0.479

Table 6. Ultrasonic velocity and other acoustic parameter of copper soap derived from treated Mustard oil for 15 Minute. (CM$_{15}$)

c (mol l^{-1})	ρ (g dm^{-3})	u (m s^{-1})	$Z \times 10^{-5}$ (g cm^{-2} s^{-1})	$\beta_{ad} \times 10^{11}$ (cm^2 dyne^{-1})	L_f (A°)	$-\phi_k \times 10^8$	$R \times 10^{-2}$	$S_n \times 10^{-3}$
0.0021	0.8692	1273.9	1.1073	7.0895	0.5313	21.009	45.196	-13.789
0.0041	0.8693	1278.0	1.1110	7.0433	0.5296	19.940	45.280	-6.840
0.0052	0.8694	1280.0	1.1129	7.0202	0.5287	19.715	45.323	-5.450
0.0104	0.8698	1284.1	1.1169	6.9726	0.5269	12.734	45.462	-2.707
0.0156	0.8702	1288.2	1.1210	6.9246	0.5251	10.478	45.598	-1.792
0.0207	0.8707	1292.4	1.1253	6.8762	0.5232	9.396	45.730	-1.334
0.0311	0.8714	1296.6	1.1299	6.8260	0.5213	6.751	45.958	-0.885
0.0415	0.8723	1300.8	1.1347	6.7750	0.5194	5.477	46.179	-0.660
0.0519	0.8732	1305.1	1.1396	6.7240	0.5174	4.717	46.397	-0.525
0.0622	0.8741	1309.3	1.1445	6.6733	0.5155	4.204	46.616	-0.435

Table 7. Ultrasonic velocity and other acoustic parameter of copper soap derived
from treated Groundnut oil for 60 Minute (CG_{60})

c (mol l^{-1})	ρ (g dm^{-3})	u (m s^{-1})	$Z \times 10^{-5}$ (g cm^{-2} s^{-1})	$\beta_{ad} \times 10^{11}$ (cm^2 dyne^{-1})	L_f (A°)	$-\phi_k \times 10^8$	$R \times 10^{-2}$	$S_n \times 10^{-3}$
0.0022	0.8690	1271.9	1.1053	7.1138	0.5322	8.138	45.182	-13.284
0.0043	0.8693	1273.9	1.1074	7.0889	0.5313	8.435	45.235	-6.616
0.0054	0.8695	1275.9	1.1094	7.0643	0.5304	10.913	45.268	-5.268
0.0108	0.8703	1282.1	1.1157	6.9909	0.5276	10.917	45.409	-2.602
0.0162	0.8712	1286.2	1.1205	6.9391	0.5256	9.646	45.519	-1.720
0.0216	0.8715	1290.3	1.1246	6.8916	0.5238	8.620	45.657	-1.281
0.0325	0.8719	1294.5	1.1287	6.8441	0.5220	6.046	45.900	-0.851
0.0433	0.8722	1298.7	1.1327	6.7978	0.5202	4.707	46.151	-0.636
0.0541	0.8727	1302.9	1.1370	6.7502	0.5184	3.954	46.392	-0.507
0.0649	0.8729	1307.2	1.1410	6.7048	0.5167	3.387	46.647	-0.421

Table 8. Ultrasonic velocity and other acoustic parameter of copper soap derived
from treated Mustard oil for 60 minutes (CM_{60})

c (mol l^{-1})	ρ (g dm^{-3})	u (m s^{-1})	$Z \times 10^{-5}$ (g cm^{-2} s^{-1})	$\beta_{ad} \times 10^{11}$ (cm^2 dyne^{-1})	L_f (A°)	$-\phi_k \times 10^8$	$R \times 10^{-2}$	$S_n \times 10^{-3}$
0.0020	0.8693	1273.9	1.1073	7.0891	0.5313	21.892	45.193	-14.102
0.0041	0.8697	1278.0	1.1114	7.0408	0.5295	21.602	45.265	-6.989
0.0051	0.8698	1282.1	1.1151	6.9947	0.5277	25.810	45.327	-5.543
0.0101	0.8704	1286.2	1.1195	6.9452	0.5259	16.236	45.455	-2.751
0.0152	0.8710	1290.3	1.1238	6.8960	0.5240	13.020	45.582	-1.820
0.0203	0.8714	1294.5	1.1280	6.8486	0.5222	11.252	45.720	-1.356
0.0304	0.8717	1298.7	1.1321	6.8018	0.5204	7.774	45.972	-0.901
0.0406	0.8720	1302.9	1.1361	6.7555	0.5186	6.015	46.225	-0.673
0.0507	0.8723	1307.2	1.1403	6.7086	0.5168	4.991	46.473	-0.536
0.0609	0.8727	1311.5	1.1445	6.6622	0.5150	4.292	46.723	-0.445

The decrease in intermolecular free length L_f with increase in soap concentration indicates that there is significant interaction between soap and solvent molecules. The decrease in adiabatic compressibility of the soap solutions with increasing soap concentration may be explain on the basis of the that the soap molecules are surrounded by a layer of solvent molecules firmly bounded. This results in the increase in the internal pressure and in lowering the compressibility of the solution *i.e.* solution becomes harder to compress. The above findings may be supported by the fact that as the concentration of solute increases, a larger portion of solvent molecules are electostricted and the amount of bulk solvent decreases causing the compressibility to decrease. In the present study, du/dc is negative which indicates the electrostriction of solvent molecule[24].

The variation in the solvation number with concentration is in fairly good agreement with the results proposed by various workers[25] for the solution of lanthanum nitrate in methanol and ethanol. The values of molar sound velocity R increase linearly with increase in soap concentration. The values of du/dc for copper soaps are positive showing resemblance with the results of other workers[26].

3.2. Micellar Features

The plots of *u*, *Z*, *β* and L_f *versus* c show break at a particular soap concentration, which corresponds to the CMC of these soaps (Fig. 1-4). At the CMC hydrocarbon chain structure of soap molecule allows extensive contact between adjacent chains due to change in vibrational and rotational degree of freedom of methylene group. The values of CMC of these soaps are recorded in Table-9. From the Table-9, it is clear that CMC follows the order:

$$CG > CM, \quad CG_{15} < CM_{15}, \quad CG_{60} > CM_{60}$$
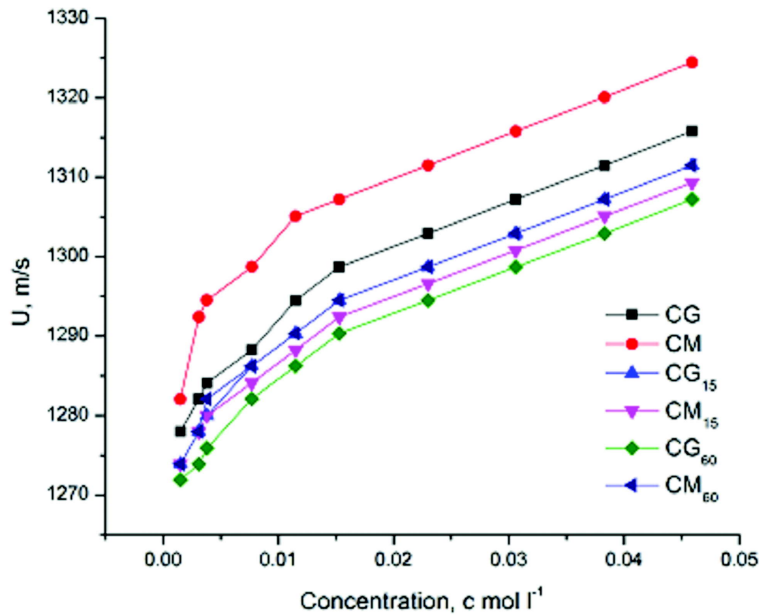
Fig. 1. Plots of *u* versus *c* for copper soaps derived from treated and untreated groundnut and mustard oils at high temperatures in benzene.
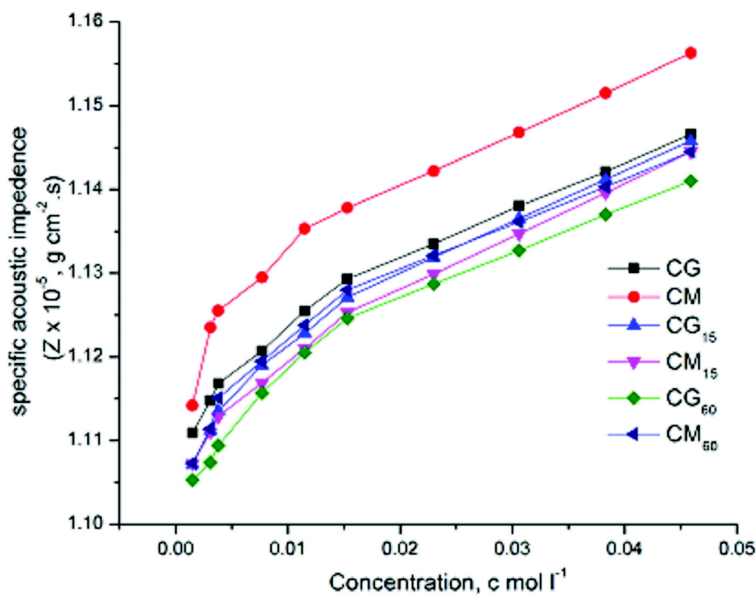
Fig. 2. Plots of *z* versus *c* for copper soaps derived from treated and untreated groundnut and mustard oils at high temperatures in benzene.
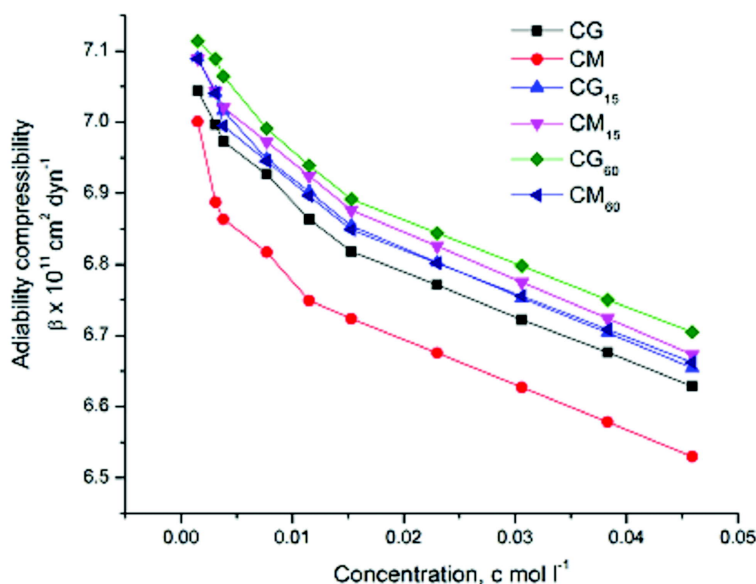
Fig. 3. Plots of β_{ad} versus *c* for copper soaps derived from treated and untreated groundnut and mustard oils at high temperatures in benzene.
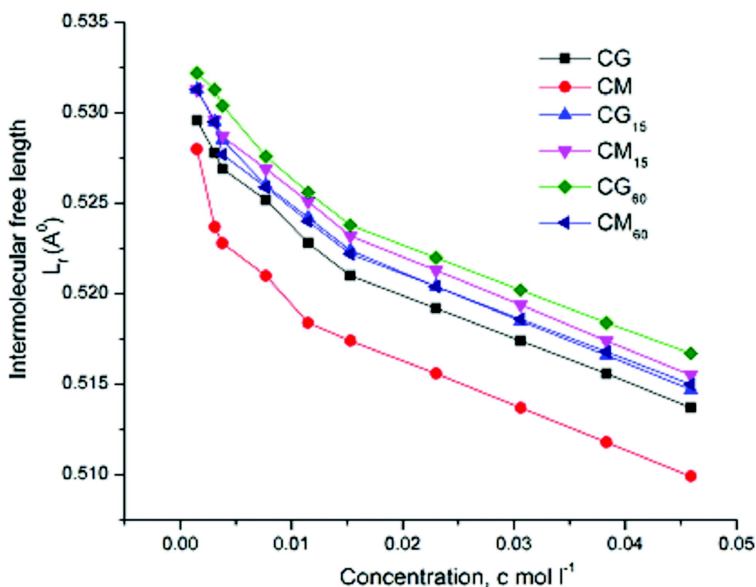

Fig. 4. Plots of L_f versus *c* for copper soaps derived from treated and untreated groundnut and mustard oils at high temperatures in benzene.

The variation of the ultrasonic velocity with soap concentration c is expressed by the equation:

$$u = u^0 + Gc \qquad (12)$$

Here u_0 is the ultrasonic velocity in the solvent. Here G is Gruneisen constant[27]. The value of G is obtained from the slope of the linear plots of u *versus* c below CMC. The plots of ultrasonic velocity versus soap concentration (Fig-1) are extrapolated to zero soap concentration. It is found that the extrapolated values of ultrasonic velocity is in agreement with the experimental value of the velocity in the solvent, indicating that the soap molecules do not aggregate to an appreciable extent below CMC[28].

Table 9. Values of CMC of Copper soaps derived from untreated and treated oils.

Plot	Name of the soap					
	CG	CM	CG_{15}	CM_{15}	CG_{60}	CM_{60}
u versus c	0.0115	0.0105	0.0135	0.0155	0.0165	0.0150
Z versus c	0.0115	0.0105	0.0135	0.0155	0.0165	0.0150
β_{ad} versus c	0.0115	0.0105	0.0135	0.0155	0.0165	0.0150
L_f versus c	0.0115	0.0105	0.0135	0.0155	0.0165	0.0150
ϕ_k versus $\sqrt{c}$	0.012	0.011	0.0139	0.0154	0.0164	0.0151

It is interesting to point out those values of the parameters u, Z, β_{ad} and L_f with respect to copper soaps of different untreated and treated oils follow the order:

[u] CM > CG   [u] : CG_{15} > CM_{15} [u] $\Rightarrow CM_{60}$ CG_{60}

[Z] CM > CG   [Z] : $CG15$ > $CM15$ [Z] CM_{60} > CG_{60}

[β] CM < CG   [β] CG_{15} < CM_{15} [β_{ad}] CM_{60} < CG_{60}

[Lf] CM< CG   [L_f] CG_{15} < CM_{15} [Lf] CM_{60} < CG_{60}

The comparison of results for copper soaps of untreated and treated oils suggests that the values of u and Z follow the order:

$$CG > CG_{15} > CG_{60}$$
$$CM > CM_{15} > CM_{60}$$

As observed, the values of ϕ_k increase sharply up to the critical micelle concentration and after CMC it increases gradually. ϕ_k is a function of concentration and its value is found to be in good agreement with that obtained from the following Masson equation [29].
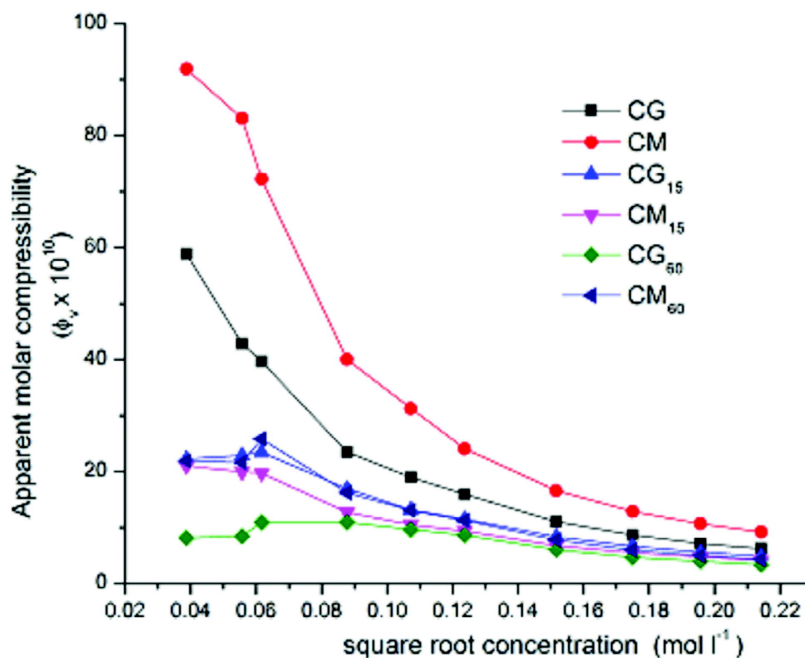
$$\phi_k = \phi^0_k + S_k \sqrt{c} \tag{13}$$

Fig. 5. Plots of ϕ_k versus $\sqrt{c}$ for copper soaps derived from treated and untreated groundnut and mustard oils at high temperatures in benzene.

Where ϕ_k is the limiting apparent molar compressibility and S_k is a constant. The plots of apparent molar compressibility ϕ_k against square root of soap concentration $\sqrt{c}$ are characterized by the intersection of two straight lines at the CMC (Fig. 5). Values of $\phi°_k$ are evaluated from the intercepts of the linear plots of ϕ_k versus $\sqrt{c}$ and values of S_k are calculated from the slope of these plots. In view of the two intersecting straight lines for ϕ_k versus $\sqrt{c}$ plots, it is reasonable to determine two values of parameters $\phi°_k$ and S_k below and above CMC designated as $\phi°_{k1}$, S_{k1} and $\phi°_{k2}$, S_{k2} respectively and recorded in Table 10. From the Table 10, it is clear that the values of $\phi°_{k1}$ and $\phi°_{k2}$ are negative for all these copper soaps. The negative ϕ_k values may be due to the loss of compressibility of solvent due to strong electrostrictive forces in the vicinity of ions [30]. The change in the values of $\phi°_k$ and S_k below and above CMC suggests that there is a phenomenal change in the micellarformation.

Table 10. Values of various constants obtained from Masson's equation for Copper soaps derived from treated and non-treated oils in benzene

Name of the soap	$u_0 \times 10^{-5}$	$G \times 10^{-5}$	$\phi°_{k1} \times 10^8$	$\phi°_{k2} \times 10^8$	$S_{k1} \times 10^8$	$S_{k2} \times 10^8$
CG	1275.5	1.6642	-73.0	-23.0	2.1445	0.3345
CM	1287.0	1.6642	-141.0	-34.0	4.7046	0.4877
CG_{15}	1270.5	1.6318	-33.0	-21.5	0.7002	0.3057
CM_{15}	1272.0	1.1917	-30.0	-17.0	0.6248	0.1943
CG_{60}	1267.0	1.1503	-13.0	-14.5	0.1051	0.2308
CM_{60}	1271.5	1.4281	-30.0	-22.0	0.5543	0.3249

The values of limiting apparent molar compressibility ($\phi°_{k1}$ and $\phi°_{k2}$) are negative and are in the following order :

$$\phi°_{k2} > \phi°_{k1} \text{ and } S_{k1} > S_{k2}$$

It is apparent from that CMC values follow the order:

$$CG > CM, \ CG_{15} < CM_{15}, \ CG_{60} > CM_{60}$$

The results suggested there is decrease in the CMC with the increase in average molecular weight of the soap.This order of CMC is same as observed by other physical properties.

4. CONCLUSION

The ultrasonic velocity and other acoustical parameters of copper surfactants derived from Groundnut and Mustard oil with non polar pure benzene shows the intermolecular interaction in constituent molecules. The decrease in adiabatic compressibility of the soap solutions with increasing soap concentration may be explained on the basis of that the soap molecules are surrounded by a layer of solvent molecules firmly bounded. This results in the increase in the internal pressure and in lowering the compressibility of the solution. This provides useful information about the nature of inter molecular forces occurs in the mixture.

5. ACKNOWLEDGMENT

6. REFERENCES

[1] R. Sharma and A. K. Sharma, 2017. Natural Edible Oils: Comparative Health Aspects of Sesame, Coconut, Mustard (Rape Seed) and Groundnut (Peanut) A Biomedical Approach. *Biomed J. Sci. & Tech Res.* **1**(5), BJSTR.MS.ID.00044.

[2] G. Savaroglu and M. Ozdemir, 2008. Apparent molar volume and apparent molar isentropic compressibility of glycerol in fructose water at different temperature. *J. Mol. Liquids,* **137**, 51-57.

[3] P. Tank, R. Sharma and A. K. Sharma, 2017. A Pharmaceutical approach & Antifungal activities of Copper Soaps with their N & S donor complexes derived from Mustard and Soyabean oils. *Glob. J. Pharmaceu. Sci.* **3**(4), GJPPS.MS.ID.555619.

[4] V. K. Syal, S. Chauhan and R. Gautam, 1998. Ultrasonic velocity measurements of carbohydrates in binarymixtures of DMSO + H$_2$O at 25°C. *Ultrasonics,* **36**, 619-621.

[5] P. Tank, R. Sharma and A. K. Sharma, 2017. Thermal Behaviour and Kinetics of Copper (II) Soaps and Complexes Derived from Mustard and Soyabean Oil. *J. Anal. Pharm. Res.* **4**(2), 1-5.

[6] S. Sharma, R. Sharma and A. K. Sharma, 2017. Synthesis, Characterization, and thermal degradation of Cu (II) Surfactants for sustainable green chem. *Asian J. Green Chem*. **2**(2), 129-140.

[7] A. K. Sharma, S. Sharma and R. Sharma, 2017. Thermal degradation of Cu (II) metallic Soaps and their Characterizations. A Pharmaceutical Application. *Chronicles of Pharmaceutical Science.* **1**(5), 312-319.

[8] S. Sharma, R. Sharma, L. C. Heda and A. K. Sharma, 2017. Kinetic parameters and Photo Degradation studies of Copper Soap derived from Soybean Oil using ZnO as a Photo catalyst in Solid and Solution Phase. *J. Inst. Chemists* (India). **89**(4), 119-136.

[9] A. K. Sharma, M. Saxena and R. Sharma, 2017. Synthesis, spectroscopic and fungicidal studies of Cu (II) soaps derived from groundnut and sesame oils and their urea complexes. *Bulletin of Pure and Applied Sciences.* **36**(2), 26-37.

[10] A.K. Sharma, M. Saxena and R. Sharma, 2018. Synthesis, Spectroscopic and Biocidal activities of environmentally safe Agrochemicals. *J. Biochem. Tech.* **7**(3), 1139-1147.

[11] S. Punitha and R. Uvarani, 2014. Physico-chemical studies on some saccharides in aqueous cellulose solutions at different temperatures- Acoustical and FTIR analysis. *J. Saudi Chem. Soc*. 18, 657-665.

[12] A. Joram, R. Sharma and A. K. Sharma, 2017. Thermal Degradation of Complexes Derived from Copper (II) Groundnut Soap *(Arachishypogaea)* and Copper (II) Sesame Soap *(Sesamumindicum) Z phy chem.* **232**(4), 459–470

[13] V. M. Kagathara, M. R. Sanariya and P. H. Parsania, 2000. Sound velocity and molecular interaction studies on chloroepoxy resins solutions at 30°C. *Eur. Polym. J.* **36**, 2371-2374.

[14] S. Khan, R. Sharma and A. K. Sharma, 2017. Antifungal Activities of Copper Surfactants derived from Neem *(AzadirectaIndica)* and Karanj *(Pongamia pinnata)* Oils: A Pharmaceutical Application. *Glob. J. Pharmaceu. Sci.* **3**(4), GJPPS.MS.ID.555616.

[15] A. K. Dash and R. Paikaray, 2013. Acoustical study on ternary mixture of dimethyl acetamide (DMAC) in diethyl ether and isobutyl methyl ketone at different frequencies. *Phys. Chem. Liq.* **51**(6), 749-763.

[16] R. Sharma, R. Bhutra and S. Khan, 2010. Micellar Behaviour of Copper Surfactants Derived from Fresh (Untreated) Sesame Oil and Used (Treated at High Temperature) Sesame Oil. *Tenside Surf Det.* **47**, 106-112.

[17] A. K. Sharma, M. Saxena and R. Sharma, 2017. Ultrasonic studies of Cu (II) Soaps derived from Mustard and Soybean oils. J. Pure Appl. Ultrason. **39**(3), 92-99.

[18] P. Tank, R. Sharma and A. K. Sharma, 2017. Studies of Ultrasonic and acoustic parameters of complexes derived from Copper (II) surfactant of mustard oil with N and S atoms containing ligands in non-aqueous media (benzene) at 303.15 K. *J. Acous. Soc. Ind.* **44**(2), 87-99.

[19] R. Bhutra, R. Sharma and A. K. Sharma, 2017. Viscometric and CMC studies of Cu(II) surfactants derived from untreated and treated groundnut and mustard oils in non-aqueous solvent at 298.15 K. *J. Inst. Chemists (India).* **90**, 29-47.

[20] R. Bhutra, R. Sharma and A. K. Sharma, 2017. Comparative Studies of Treated & Untreated Oils as Cu (II) Surfactants "ISBN978-3-659-83122-5" *LAP Lambert Academic Publishing Germany*.

[21] V. Sivakumar, R.V. Verma, P.G. Rao and G. Swaminathan, 2007. Studies on the use of power ultrasound in solid liquid myrobal an extraction process. *J. Clean Prod.* **15**, 1813-1818.

[22] S. Khan, R. Sharma and A. K. Sharma, 2017. Ultrasonic studies of Cu(II) Soap derived from seed oil of Pongamia pinnata (Karanj) in non-aqueous binary and ternary systems at 298.15K. *Malaysian J. Chem.* **19**(2), 99-110.

[23] G. Singh and T. S. Banipal, 2008. Partial molar adiabatic compressibilities and viscosities of some amino acids in aqueous glycerol solutions at 298.15K. *Indian J. Chem.* **47A**, 1355-1364.

[24] P. Tank, R. Sharma and A. K. Sharma, 2018. Viscometric Studies of Cu (II) surfactants derived from mustard oil in benzene at 303.15K. *Tenside Surf Det.* In press.

[25] S. V. Ranganayakulu, C. S. Reddy and D.L. Reddy, 2008. Ultrasonic studies of the binary mixtures of ethyl acetate and cresols-application of Kosower and Dimroth Treatments. *Mat. Chem. Phys.* **90**, 213-216.

[26] P. Tank, R. Sharma and A. K. Sharma, 2018. Micellar Features and Various Interactions of Copper Soap Complexes Derived from Edible Mustard Oil in Benzene at 303.15 K. *Curr. Phy. Chem.* **8**(1), 46-57

[27] S. R. Kanhekar, P. Pravina and K. B. Govind, 2010. Thermodynamic properties of electrolytes in aqueous solutions of glycine at different temperatures. *Indian J. Pure Appl. Phys.* **48**, 95-99.

[28] A. K. Sharma, M. Saxena and R. Sharma, 2017. Ultrasonic studies of Cu (II) Soaps derived from Groundnut and Sesame oils. *Tenside. Surf. Det.* **55**(2), 127-134.

[29] D. O. Masson, 1929. Solute molecular volumes in relation to solvation and ionization, *Philos. Mag.*, **8**, 218-235.

[30] A. K. Sharma, M. Saxena, R. Sharma, Ultrasonic studies of Copper Soaps Urea complexes derived from Mustard and Soyabean oils. *J. Phy. Sci.* In press.

INFORMATION FOR AUTHORS

ARTICLES

The Journal of Acoustical Society of India (JASI) is a refereed publication published quarterly by the Acoustical Society of India (ASI). JASI includes refereed articles, technical notes, letters-to-the-editor, book review and announcements of general interest to readers.

Articles may be theoretical or experimental in nature. But those which combine theoretical and experimental approaches to solve acoustics problems are particularly welcome. Technical notes, letters-to-the-editor and announcements may also be submitted. Articles must not have been published previously in other engineering or scientific journals. Articles in the following are particularly encouraged: applied acoustics, acoustical materials, active noise & vibration control, bioacoustics, communication acoustics including speech, computational acoustics, electro-acoustics and audio engineering, environmental acoustics, musical acoustics, non-linear acoustics, noise, physical acoustics, physiological and psychological acoustics, quieter technologies, room and building acoustics, structural acoustics and vibration, ultrasonics, underwater acoustics.

Authors whose articles are accepted for publication must transfer copyright of their articles to the ASI. This transfer involves publication only and does not in any way alter the author's traditional right regarding his/her articles.

PREPARATION OF MANUSCRIPTS

All manuscripts are refereed by at least two referees and are reviewed by the Publication Committee (all editors) before acceptance. Manuscripts of articles and technical notes should be submitted for review electronically to the Chief Editor by e-mail or by express mail on a disc. JASI maintains a high standard in the reviewing process and only accept papers of high quality. On acceptance, revised articles of all authors should be submitted to the Chief Editor by e-mail or by express mail.

Text of the manuscript should be double-spaced on A4 size paper, subdivided by main headings-typed in upper and lower case flush centre, with one line of space above and below and sub-headings within a section-typed in upper and lower case understood, flush left, followed by a period. Sub-sub headings should be italic. Articles should be written so that readers in different fields of acoustics can understand them easily. Manuscripts are only published if not normally exceeding twenty double-spaced text pages. If figures and illustrations are included then normally they should be restricted to no more than twelve-fifteen.

The first page of manuscripts should include on separate lines, the title of article, the names, of authors, affiliations and mailing addresses of authors in upper and lowers case. Do not include the author's title, position or degrees. Give an adequate post office address including pin or other postal code and the name of the city. An abstract of not more than 200 words should be included with each article. References should be numbered consecutively throughout the article with the number appearing as a superscript at the end of the sentence unless such placement causes ambiguity. The references should be grouped together, double spaced at the end of the article on a separate page. Footnotes are discouraged. Abbreviations and special terms must be defined if used.

EQUATIONS

Mathematical expressions should be typewritten as completely as possible. Equation should be numbered consecutively throughout the body of the article at the right hand margin in parentheses. Use letters and numbers for any equations in an appendix: Appendix A: (A1, (A2), etc. Equation numbers in the running text should be enclosed in parentheses, i.e., Eq. (1), Eqs. (1a) and (2a). Figures should be referred to as Fig. 1, Fig. 2, etc. Reference to table is in full: Table 1, Table 2, etc. Metric units should be used: the preferred from of metric unit is the System International (SI).

REFERENCES

The order and style of information differs slightly between periodical and book references and between published and unpublished references, depending on the available publication entries. A few examples are shown below.

Periodicals:
[1]   S.R. Pride and M.W. Haartsen, 1996. Electroseismic wave properties, *J. Acoust. Soc. Am.*, **100** (3), 1301-1315.
[2]   S.-H. Kim and I. Lee, 1996. Aeroelastic analysis of a flexible airfoil with free play non-linearity, *J. Sound Vib.*, **193** (4), 823-846.

Books:
[1]   E.S. Skudzryk, 1968. *Simple and Comlex Vibratory Systems*, the Pennsylvania State University Press, London.
[2]   E.H. Dowell, 1975. *Aeroelasticity of plates and shells*, Nordhoff, Leyden.

Others:
[1]   J.N. Yang and A. Akbarpour, 1987. Technical Report NCEER-87-0007, Instantaneous Optimal Control Law For Tall Buildings Under Seismic Excitations.

SUMISSIONS

All materials from authors should be submitted in electronic form to the JASI Chief Editor: B. Chakraborty, CSIR - National Institute of Oceanography, Dona Paula, Goa-403 004, Tel: +91.832.2450.318, Fax: +91.832.2450.602,(e-mail: bishwajit@nio.org) For the item to be published in a given issue of a journal, the manuscript must reach the Chief Editor at least twelve week before the publication date.

SUMISSION OF ACCEPTED MANUSCRIPT

On acceptance, revised articles should be submitted in electronic form to the JASI Chief Editor (bishwajit@nio.org)

THE JOURNAL OF ACOUSTICAL SOCIETY OF INDIA

The Journal of Acoustical Society of India

ASI

CHIEF EDITOR:

B. Chakraborty
CSIR-National Institute of Oceanography
Dona Paula,
Goa-403 004
Tel: +91.832.2450.318
Fax: +91.832.2450.602
E-mail: bishwajit@nio.org

ASSOCIATE SCIENTIFIC EDITOR:

A R Mohanty
Mechanical Engg. Department
Indian Institute of Technology
Kharagpur-721302, India
Tel. : +91-3222-282944
E-mail : amohantyemech.iitkgp.ernet.in

Editorial Office:
MANAGING EDITOR
Mahavir Singh

ASSISTANT EDITORS:

Yudhisther Kumar
Devraj Singh
Kirti Soni
ASI Secretariat,
C/o Acoustics, Ultrasonics & Vibration
Section CSIR-National Physical Laboratory
Dr. KS Krishnan Road
New Delhi 110 012
Tel: +91.11. 4560.8317
Fax: +91.11.4560.9310
E-mail: asisecretariat.india@gmail.com

The Journal of Acoustical Society of India is a refereed journal of the Acoustical Society of India **(ASI)**. The **ASI** is a non-profit national society founded in 31st July, 1971. The primary objective of the society is to advance the science of acoustics by creating an organization that is responsive to the needs of scientists and engineers concerned with acoustics problems all around the world.

Manuscripts of articles, technical notes and letter to the editor should be submitted to the Chief Editor. Copies of articles on specific topics listed above should also be submitted to the respective Associate Scientific Editor. Manuscripts are refereed by at least two referees and are reviewed by Publication Committee (all editors) before acceptance. On acceptance, revised articles with the text and figures scanned as separate files on a diskette should be submitted to the Editor by express mail. Manuscripts of articles must be prepared in strict accordance with the author instructions.

All information concerning subscription, new books, journals, conferences, etc. should be submitted to Chief Editor:

B. Chakraborty, CSIR - National Institute of Oceanography, Dona Paula, Goa-403 004,
Tel: +91.832.2450.318, Fax: +91.832.2450.602, e-mail: bishwajit@nio.org

Annual subscription price including mail postage is Rs. 2500/= for institutions, companies and libraries and Rs. 2500/= for individuals who are not **ASI** members. The Journal of Acoustical Society of India will be sent to **ASI** members free of any extra charge. Requests for specimen copies and claims for missing issues as well as address changes should be sent to the Editorial Office:

ASI Secretariat, C/o Acoustics, Ultrasonics & Vibration Section, CSIR-National Physical Laboratory, Dr. KS Krishnan Road, New Delhi 110 012, Tel: +91.11.4560.8317, Fax: +91.11.4560.9310, e-mail: asisecretariat.india@gmail.com

The Journal of Acoustical Society of India

A quarterly publication of the Acoustical Society of India

Volume 45, Number 2, April 2018

ARTICLES

INFORMATION

FOREWORD

Acoustic techniques continue to be the most effective means for probing the ocean volume and the structure beneath the sea floor. Our data collection and research studies in the Indian Ocean region reveal that the ocean environment is changing rapidly and the ocean in the near-future will be in many ways different from the one we know today. As we see unprecedented changes occurring in the marine environment on a global scale, one naturally wonders how the ocean is responding to both natural processes and human activities.

We need to understand the changing ocean to help us design and develop effective and state of the art underwater sensors and surveillance technologies. We have learned a great deal about how a sound understanding of ocean environment can help enhance our present technical capabilities and trigger future advancements. For sustained growth and development of futuristic underwater systems, we believe that it is crucial to understand and address such fundamental problems and evolve new directions and innovative technologies.

It is heartening to note that JASI is bringing out a special issue to address and summarize the recent accomplishments in this critical and specialized area of research and development – the influence of the ocean medium on the performance of underwater sensor systems. The papers in this special issue themed "Ocean Environmental Acoustics" indicate surge in interest and swift progress in the area of underwater acoustic experiments and modeling in the last few years.

Before I conclude, I wish to thank the editorial board for sparing their precious time to review the papers and assist the authors in refining the papers further with their suggestions and encouragement. I also compliment the authors for coming out with a bouquet of papers covering different aspects of the main theme.

S. Kedarnath Shenoy
Director
Naval Physical and Oceanographic Laboratory
Defence Research and Development Organisation
Ministry of Defence, Kochi, Kerala-682021

EDITORIAL

Ocean Acoustics is the science of sound waves in the ocean, and has become an imperative tool for underwater remote sensing. Advancement in the field of *Ocean Acoustics* has propelled researchers to investigate oceanic features and associated processes. Besides scientific investigations, the development of a coastal security system for India's coastline requires a technology where *Ocean Acoustics* can be relied up on to provide enormous support.

The propagation of sound, especially in the shallow coastal environment is a complex function of varying bathymetry and oceanography, and the presence of various dynamic features. Also, the target and receiver motion leads to a highly non-linear problem both for prediction of sensor performance and for optimization of search tracks for successful naval operations. Usually, the problem is split into the lines of physics (environmental variability and propagation physics) and mathematical operations (target motion and optimal search strategies). Accurate sonar performance in the presence of dynamic interferers in a complex acoustic propagation environment requires the computation of the full field array response to both signal and the dynamic noise field. In the year 2018, the Naval Physical & Oceanographic Laboratory (NPOL) conducted an International Conference *"ICONS"* to bring world-wide premier research institutes under one umbrella. The inspirational efforts have resulted in number of original research articles.

Journal of Acoustical Society of India (JASI) has been publishing quality research articles covering the recent advancement in the field of Ocean Acoustics to familiarize the ocean scientists with the advances in Ocean Acoustics Technology and establish a benchmark for future research. The special issue *"Ocean Environmental Acoustics"* has compiled a selection of insightful papers that address most recent advancement on Ocean Acoustics Research in India. A variety of topics, including computational acoustics and experimental acoustics has been covered in this issue. The special issue encourages researchers to establish joint collaborative projects and to conduct possible experiments using underwater acoustics technology.

The special issue includes 7 papers that were reviewed and accepted. Among them five papers were based on the experimental results while two papers covered the development of new techniques for the analysis of sonar data. The first paper is related to the inversion of sound speed profile in a shallow water environment using multipath travel time information derived from measurements of acoustic channel impulse response (Poonam Panchal and Sreeram Radhakrishnan). Padmanabham et al. discussed the effect of sonic layer depth on the acoustic Transmission Loss levels for the deep water region using the experimental results and ray theory based Gaussian beam acoustic model, BELLHOP. The generation of reverberation profiles considering the Volume, Surface and Bottom scatterings and its performance evaluation using the measured sonar data is described by Amit Kumar Verma *et al.* The feasibility of linear estimation techniques to reconstruct the acoustical images of objects using simulation and qualitative evaluation of their performances using experiment data is explained by Hareesh *et al.* Linthish *et al.* deals with the experimental methods developed for low-frequency receiving sensitivity measurement of underwater transducers in a small acoustic tank with real-time signal processing techniques The problem of direction of arrival estimation of unknown sources in deep water scenario is established using a computationally efficient scheme of MVDR beam forming (Patrik Jain and Rema Devi). Detection of target in an underwater environment is very challenging due to reverberation and fast fading nature of the channel. To address this aspect, Thasneem et al. introduced a new detection technique *viz.* segmented replica correlation using Fractional Fourier Transform.

The Guest Editor thanks Shri. S. Kedarnath Shenoy, Director, NPOL for his encouragement to complete this special issue of JASI. He also thanks Dr. Biswajith Chakraborty, Chief Editor, JASI, for his consent and advice to consolidate the special issue. The Guest Editor sincerely acknowledges the support and cooperation rendered by the experts Dr. Biswajith Chakraborty, Dr. MP Ajaikumar, Dr. KG Radhakrishnan, Dr. GV Krishnakumar, and Smt. Pradeepa R who have meticulously reviewed the manuscripts to make it suitable for publication in JASI.

Dr. P.V. Hareesh Kumar
Associate Director & Sc. G
NPOL, Kochi
Guest Editor, JASI

Inversion of acoustic impulse response data to estimate water column sound speed profile in shallow water

Poonam Panchal and Sreeram Radhakrishnan

Naval Physical and Oceanographic Laboratory, Thrikkakara, Kochi, India
panchal.poonam@gmail.com

ABSTRACT

The water column sound speed profile is estimated using multipath travel time information derived from measurements of acoustic channel impulse response in a shallow water environment. An acoustic propagation experiment is conducted and impulse response data obtained for two source receiver ranges of 245m and 320m in a water depth of 71m. The sound speed profile in shallow water is highly influenced by the slope and depth of the thermocline. The inverse problem to estimate the sound speed profile is posed as an optimization problem in which the objective function gives a quantitative measure of the mismatch between the observed and modelled travel times. A ray-theory based forward propagation model is implemented to model multipath travel times. Inversion formulated as an optimization problem is solved by employing the method of Genetic Algorithm (GA) which shares an analogy with biological evolution. The ground truth sound speed profile is estimated from *in-situ* conductivity, temperature and depth (CTD) measurements and the search space is defined based on previous measurements at the same location. The sound speed profile estimated by inversion of acoustic impulse response data is found to agree reasonably well with *in-situ* sound speed profile. The difference between the inversion results and measurements is very small and not significant for most applications of acoustical oceanography and sonar range prediction.

1. INTRODUCTION

Underwater acoustic communication in shallow water is highly influenced and limited by the temporal variability of the properties of the propagation medium. The multipath propagation in shallow water tends to elongate the impulse response which leads to complications in decoding the transmitted message. Transmission through a single dominating propagation path is expected to be the ideal situation for underwater acoustic communication[1]. Numerical simulation of acoustic transmission renders itself as a useful and reliable means to understand the complexities associated with shallow water acoustic propagation. However, realistic simulation of an underwater acoustic propagation experiment requires several environmental input parameters[2,3]. The essential input parameters are bathymetry, seabed properties, sound speed profile and the source-receiver geometry at the instant of propagation. The absence of any of these parameters may introduce error in propagation modeling, limiting the agreement between simulation and measurements. Studies have also shown that poor knowledge of the sound speed profile gives rise to significant errors in geo-acoustic inversion results[4].

Matched-field processing (MFP) is a popular inversion technique in which replica fields are computed with the help of acoustic propagation models[5]. Later, the values of unknown parameters are estimated by correlating the replica fields with the measured acoustic fields. For application in range-dependent environments, Ballard and Becker[6] utilized a linearized perturbative technique to determine sound speed which makes use of estimates of horizontal wave numbers in the shallow water waveguide as a function of depth. They demonstrated that complications arise in regions above the thermocline where sound speed reduces gradually with depth and the acoustic field has very little energy. Error also occurs near the sea floor when seabed properties are not well known. Svensson[7] inverted acoustic communication signals for sound speed profile using a differential evolution algorithm conceptually similar to genetic algorithms. Their objective function measured the normalized cross correlation between the observed and modeled impulse response estimates focusing on a single peak value of impulse response.

Formulation of inversion as an optimization problem enables various optimization techniques to be applied to the inverse problems[8-10]. Genetic Algorithms have already found application in problems of ocean acoustic tomography[11] and geo-acoustic inversion using measurements of the full acoustic field at a vertical array of hydrophones. Gerstoft[12] was the first to apply GA to the problem of geo-acoustic inversion to estimate compressional and shear velocities and layer thickness of the bottom sediment. Gingras and Gerstoft[13] applied GA to the problem of source localization and successfully demonstrated inversion of both geometric and geo-acoustic parameters.

This paper aims to utilize measurements of acoustic channel impulse response to resolve multipath arrivals in a shallow water environment and later use the measured multipath arrival times for estimating the water column sound speed profile. The inversion approach used here is formulated as an optimization problem and solved by the GA method. It identifies the optimum sound speed profile which represents the best fit of ray arrival times given by numerical simulation to the impulse response peaks observed in measurements. We define a search space for sound speed at each depth and the objective of the optimization algorithm is to arrive at the best-fit sound speed profile. The sound speed characteristics that change in this parameter space are the depth and slope of the thermocline. The characteristics of the thermocline have a strong influence on the ray pattern and the impulse response and are therefore the most important to determine. The objective function of the optimization problem minimizes the sum of the squares of difference of measured and modeled travel time to obtain the best fit model of water column sound speed profile. The paper is organized as follows. Section 2 gives an overview of inversion, ray theory and a brief description of the method of sound speed profile inversion using the measured arrival time of eigenrays. The shallow water acoustic experiment and the impulse response data showing multipath arrival times are presented in section 3. The theory, working principle and implementation of optimization method used for inversion are briefly explained in section 4. Section 5 discusses the inversion results for two cases. Summary and concluding remarks are provided in section 6.

2. INVERSION IN OCEAN ACOUSTICS

Inverse problems in ocean acoustics attempt to fit the parameters of interest by means of a relationship associating measurements and the parameters to be retrieved. The actual relationship is defined on the basis of the data *d* derived from measurements, according to the method to be followed and the model vector *m* of parameters {m_i} to be recovered.

$$\{m_i\} = m \in M \text{ for } i = 1, 2, \ldots, D_M \tag{1}$$

Where D_M denotes the dimension of the model space *m*. Similarly, the data may be written as:

$$\{d_j\} = d \in Data \text{ for } j = 1, 2, \ldots, D_{Data} \tag{2}$$

Representing an element of the D_{Data} dimensional data space Data. Using this terminology, the forward and inverse models are regarded as rules that connect these two spaces:

$$\text{Forward model: } M \rightarrow Data \quad \text{Inverse model: } Data \rightarrow M \tag{3}$$

In this paper, the ray travel times of various multipaths (direct, surface-reflected, bottom-reflected and so on) in shallow water are derived from the measurements of impulse response. The ray travel time from the source to the receiver corresponding to different multipaths contains the necessary information for the calculation of water column sound speed profile. The inverse problem is defined on the basis of relationship between the arrival time of a specific eigenray and the sound speed profile along the propagation direction. In ray acoustics, the sound speed profile determines the path traversed by any given eigenray and hence there exists a unique solution for the forward problem of determining ray arrival times from the sound speed. For successful implementation of this method, it is essential to relate the peaks of the signal for the reference sound speed profile to those of the actual measurements. Eigenrays and their arrival structure were modelled with Bellhop Gaussian Beam Tracing Model developed by Porter and Bucker[14].Bellhop was chosen for this analysis since it has proven to be an accurate modelling tool for high-frequency (>1 kHz) transmissions.
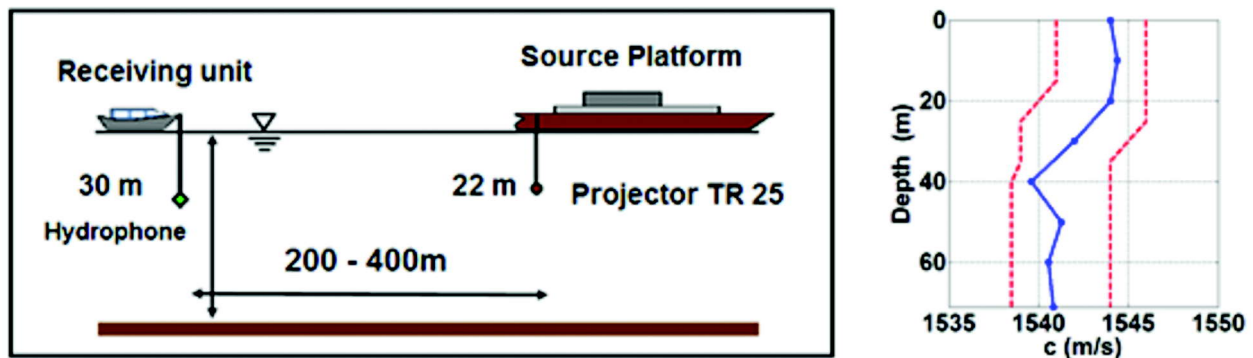

Fig. 1. LEFT: Schematic of the acoustic propagation experiment. RIGHT: Sound speed profile measured at the time of acoustic transmissions. The minimum and maximum (dashed lines) values of sound speed as a function of depth correspond to data range observed in measurements from earlier surveys conducted in March.

3. ACOUSTIC EXPERIMENT

An acoustic propagation experiment was conducted and impulse response measurements were made in March 2015 at a shallow water location in the Arabian Sea (119 km west-south-west of Kochi, India). The left panel of Fig. 1 shows the schematic of the source receiver geometry realized during the experiment. A hydrographic vessel *INSSutlej* was anchored in a water depth of 71m which served as the source platform. An omni-directional broadband projector TR-25 was used for transmitting linear frequency modulated (LFM) pulses of length 50 ms sweeping frequencies in 16-22 kHz band at a depth of 22m. The transmitting voltage response of TR-25 varies from 136 dB re 1µPa/ 1V at 1m at 16 kHz to 141 dB at 22kHz. A survey boat drifted gradually towards the source platform starting from a distance of 400m. The signals were received by B&K 8105 hydrophones deployed from the boat. The hydrophone has a sensitivity of -195.4 dB re 1µPa/ 1V in the 16-22 kHz frequency band. The hydrophone and projector depths were monitored by depth sensors. In the present study, data from the 30m depth hydrophone is analyzed for two source receiver ranges of 245m and 320m. The ranges were calculated from GPS measurements with an accuracy of 10m. The water column sound speed profile was estimated from conductivity temperature depth (CTD) casts made at regular intervals over the entire course of the experiment. The right panel of Fig. 1 shows the profile measured at 0900 hours which coincides with the time of acoustic transmissions. It also shows the sound speed range at each depth based on data collected in earlier surveys during March at the same location. This range is used as the initial search space for defining sound speed at a given depth in the forward propagation model.

The time dispersed impulse response was estimated by matched filtering of received time series with a synthetic 50 ms 16-22kHz LFM wave form. Figure 2 shows the matched filtered envelope after time alignment with respect to the direct path for 20 consecutive pings. Due to the pulse compression of LFM signals after matched filtering and the short source-receiver range (~245 m), a well-resolved arrival structure is obtained. This configuration corresponds to a source depth of 22m, receiver depth 30m in 71m water depth. The first six arrivals can be clearly identified in the dataset comprising of 20 pings.
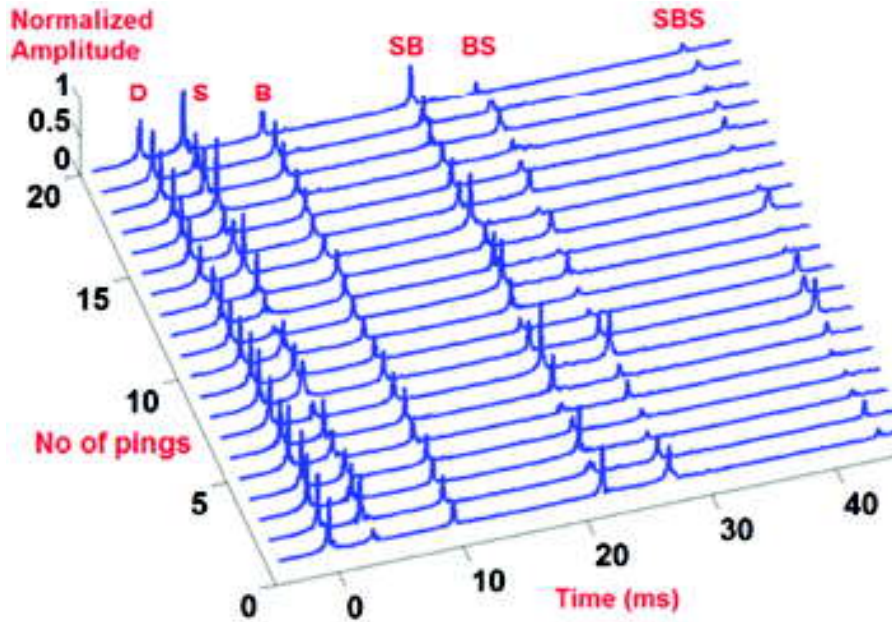

Fig. 2. Impulse responses in the form of matched filtered envelope after time alignment with respect to the direct path for 20 consecutive pings. It shows the arrivals representing the first 6 eigen rays for a source depth of 22m, receiver depth 30m and range 245m. (D-Direct, S-Surface, B-Bottom, SB-Surface Bottom, BS-Bottom Surface and SBS-Surface Bottom Surface)

In the present study, two such datasets are utilized for inverting water column sound speed profile using time of arrival information. Direct methods do exist for measuring the near-surface sound speed. This inversion technique provides a complementary method of measurement.
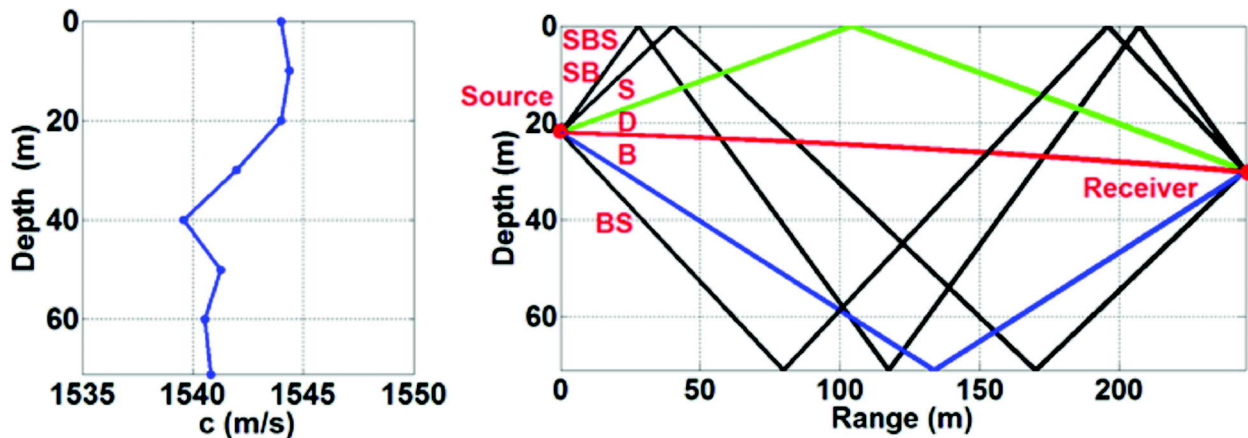

Fig. 3. LEFT: Sound speed profile measured by CTD cast. RIGHT: First 6 Eigenrays for a source depth of 22m, receiver depth 30m and range 245m modeled using Bellhop ray theory based propagation model.
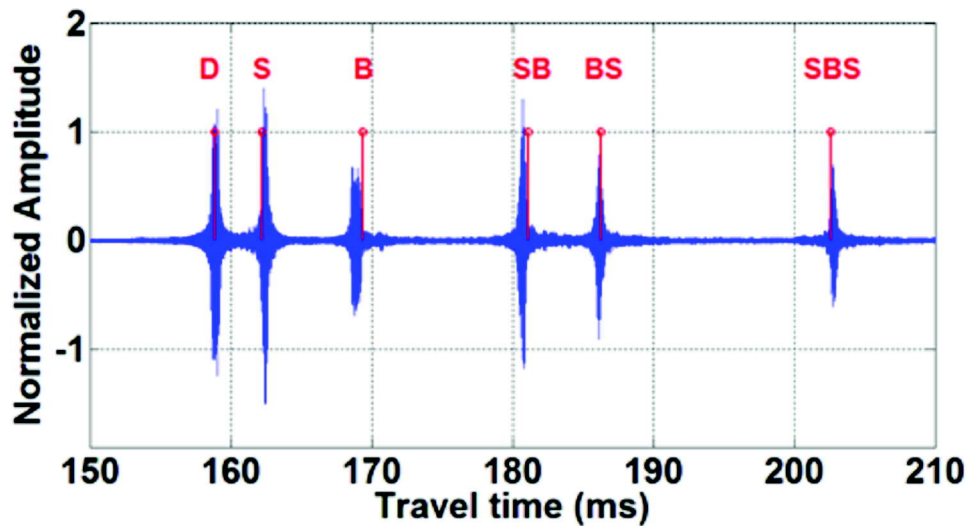
Fig. 4. Measurements of time dispersed impulse response for 50 ms 16-22 kHz LFM signal. Modelled arrival times are also plotted. The arrival time of direct path based on ray tracing is 158.88 milliseconds. Source depth is 22m, receiver depth 30m and range is 245m.

The measured sound speed profile was used as input to run the forward propagation model. The left panel of Fig. 3 shows measured sound speed profile. The right panel shows the first 6 eigenrays which include direct, surface, bottom, surface-bottom, bottom-surface and surface-bottom-surface paths for the first configuration corresponding to a source receiver range of 245m. The measured and modelled impulse response travel times are plotted in Fig. 4. The multipath arrival structure modelled using in-situ measured sound speed profile as input matches very well with the measured data. The first arrival corresponding to direct path takes 158.88 ms to reach the receiver. The objective function used here is the sum of least square difference between the measured and modelled travel time of multipath arrivals which can be written as

$$Q = [X_i - M_i]^T [X_i - M_i] \text{ for } i = 1 \text{ to } 6 \tag{4}$$

Where X_i = Measured travel time of ith arrival, M_i = Modeled travel time of ith arrival. Here I varies from 1 to 6 representing direct, surface, bottom, surface-bottom, bottom-surface and surface-bottom-surface paths. The forward propagation model generates modeled arrival times (M_i) and the optimization algorithm aims to identify the M_i which gives the least value of the objection function. The least objective function represents the highest degree of match between the modeled and measured travel times.

4. INVERSION METHOD

Genetic algorithms (GA) are self-adaptive, stochastic search mechanisms to solve a wide variety of optimization and inversion problems. GA is based on underlying genetic biological evolution principles and natural selection[15]. GA intelligently executes a random simultaneous search from a wide sampling of the cost surface to solve global optimization problems.GA allows a population of individuals to evolve under specified selection rules in a way that next generation is fitter than previous generation and finally reaches to a highest state of fitness. Evolution process of GA optimization is facilitated by three major constituent operators, selection, crossover and mutation.Given a sound speed profile we can calculate the travel times by solving the forward problem. Each forward model run corresponds to a distinct water column sound speed profile. Other input parameters remain constant. The initial search space consists of a coarse resolution sound speed profile. These constraints on sound speed as a function of depth are fixed using sound speed values estimated from *in-situ* CTD measurements during earlier surveys conducted in the month of March at the same location.

Table 1. Initial search space for water column sound speed profile

S No	Depth range z(m)	Sound speed rangec(z) (m/s)
1	$z_1 = 0$	$1541 < c(z_1) < 1546$
2	$z_2 = 10$	$c(z_1) -0.5 < c(z_2) < c(z_1) +0.5$
3	$19< z_3 <21$	$c(z_2) -0.5 < c(z_3) < c(z_2) +0.5$
4	$z_4 = 30$	$c(z_3) -3 < c(z_4) < c(z_3) -1$
5	$39 < z_5 < 41$	$c(z_4) -3 < c(z_5) < c(z_4) -2$
6	$49 < z_6 < 51$	$c(z_5) -1 < c(z_6) < c(z_3) +2$
7	$z_7 = 60$	$c(z_6) -1 < c(z_7) < c(z_6) +1$
8	$z_8 = 71$	$c(z_7) -1 < c(z_8) < c(z_7) +1$

To describe the profile characteristics properly and efficiently keeping in mind the physical processes, each profile is represented by eight depth points as given in Table 1. There are two points from the surface to the thermocline (z = 0 and 10 m), three points spanning the thermocline (z = 19-21m, 30m, 39-41 m) and two points for minimum below the thermocline (z = 49-51m, 60m). The points z = 0 and z = 71m represent the surface and bottom respectively. The sound speed gradients in the layers above and below the thermocline are set not to exceed 0.5 s^{-1} whereas the gradient in the thermocline can be as high as 3.0 s^{-1} as observed in data collected in earlier surveys during March.

5. RESULTS AND DISCUSSION

An initial population of 10 candidate sound speed profiles for GA was created by selecting sub population of 10 best candidates among 20 randomly generated candidates (Fig. 5) within the search space defined at each depth in the earlier section. The fitness of each sound speed profile is checked based on the difference between the measured travel times and the travel times computed using the forward propagation model. Then, through a set of evolutionary steps the initial population evolves to attain a higher level of fitness. The GA parameters used for inverting the two datasets are listed in Table 2.
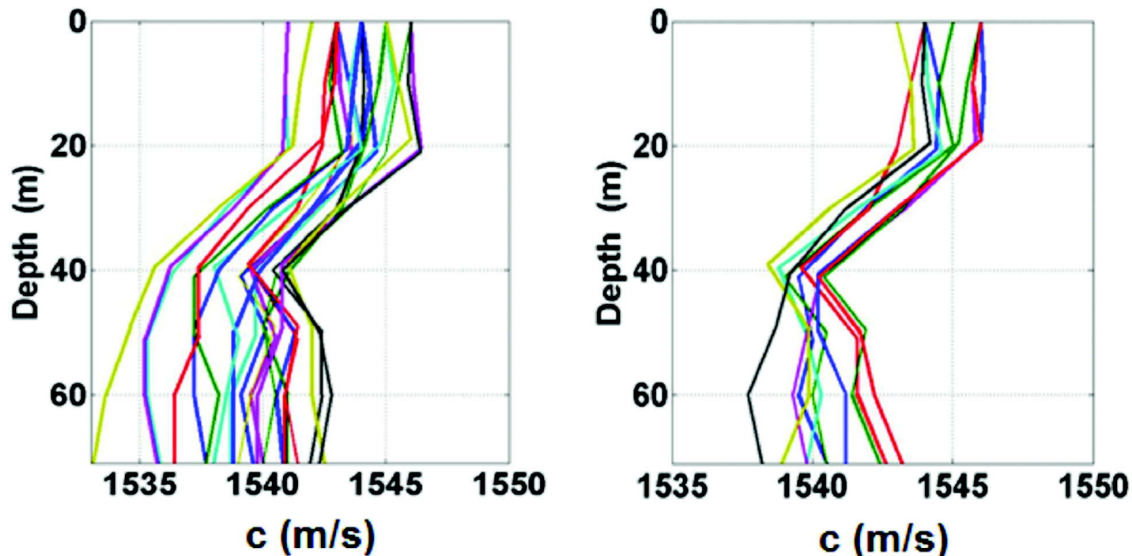

Fig. 5. LEFT: The initial population of 20 randomly generated sound speed profiles. RIGHT: Best 10 sound speed profiles chosen from the initial population to ensure that the profiles are strictly confined within the sound speed constraints.

Table 2. The values of GA parameters for model runs 1 to 4 for a source receiver range of 245m and 320 m

Run No	No of Generations	Population size	Mutation rate	Selection rate	Cost Function (245 m)	Cost Function (320 m)
1	5	10	0.02	0.5	0.000067	0.0032
2	10	10	0.02	0.5	0.000050	0.0019
3	15	10	0.02	0.5	0.000043	0.0015
4	20	10	0.02	0.5	0.000041	0.0015

For each dataset, four inversion runs are carried out for generations of 5, 10, 15 and 20 respectively. The size of initial population is set at 10 with a crossover probability of 1, a selection rate of 0.5 and a mutation rate of 0.02 from one generation to the next.

It is possible that the reduction in value of the objective function may not reflect as an improvement in the estimated values of the sound speed profile. Therefore, the estimated sound speed values are compared to the measured values at each of the 8 depth points to evaluate the effectiveness of the optimization method. For the 245m impulse response data, it is observed that the objective function converges after 10 generations. The improvement in accuracy is only marginal as the number of generations is increased beyond 10. The objective function value is equal to 0.000041 for a GA run of 20 generations using 245m range impulse response data. The plots comparing the measured sound speed profile and GA estimated sound speed profile appear in Figure 6.The top layer is fairly uniform up to a depth of 20m. The thermocline slope as observed in the measured profile is 0.2 s^{-1}. The thermocline layer begins at 20m and extends upto a depth of 40m. The sound speed observed at 20m depth is 1543 m/s and it reduces to 1540 m/s at the bottom of the thermocline. The layer below the thermocline is fairly uniform with a top-to-bottom difference of less than 1.5 m/s over a depth of 30m. The slope and depth of the thermocline agree well between the measured and estimated profiles for inversion using 245m range impulse response data.
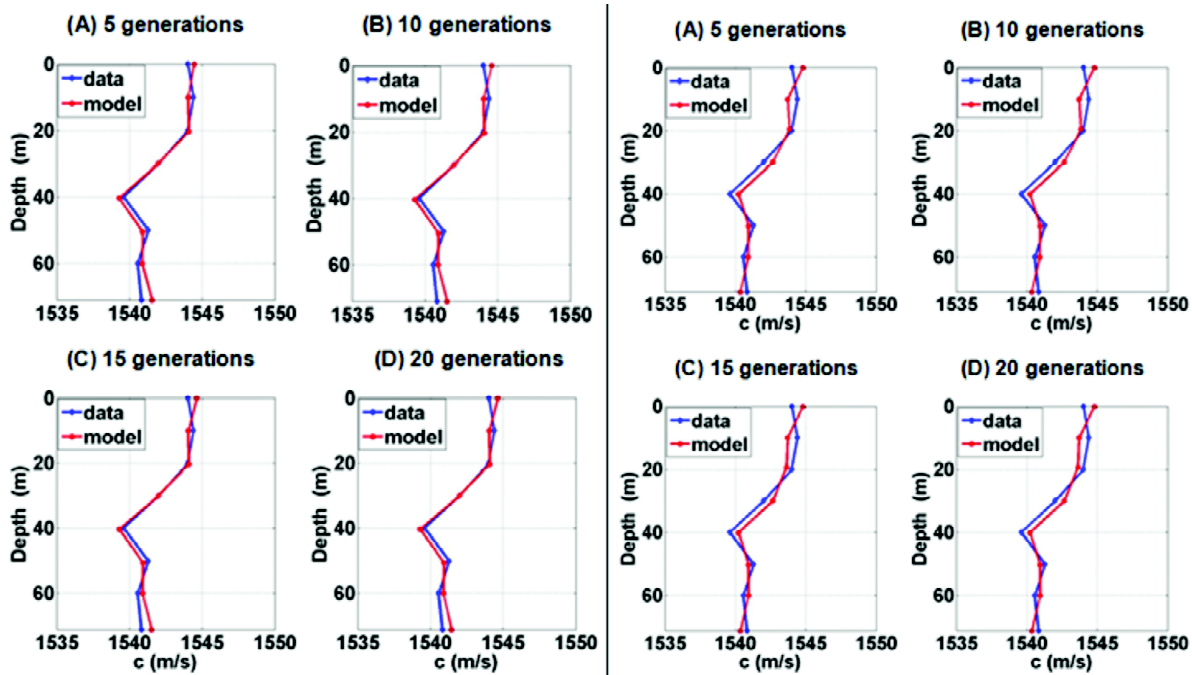

Fig. 6. Comparison of Best fit sound speed profile with CTD measured data for GA runs corresponding to 5, 10, 15 and 20 generations. Source receiver ranges are 245m (left panel) and 320 m (right panel)

It is observed that as the range increases to 320m, the performance of GA deteriorates and the estimated profile does not match well with that of the measured profile. The estimated sound speed is 1.0 ms^{-1} more than the measured sound at the sea surface. At a depth of 10m, the estimated value is about 1.0 ms^{-1} less than the corresponding measured value. The match is better at the depth of 20m. The thermocline layer extends from 20 to 40m as observed both in the measured and estimated profile. The depth of the thermocline compares well with that of the measured data. However, the inversion method based on 320m impulse response data fails to predict accurately the slope of the thermocline. This discrepancy may be overcome with the help of range dependent propagation modelling wherein the sound speed profiles change with between the source and the receiver. The GA estimated sound speed profile shows a marginal difference of less than 0.5m s^{-1} in the layer below the thermocline. The objective function value is equal to 0.0015 for a GA run of 20 generations using 320m range impulse response data. There is no improvement in the objective function value as the number of generations is increased beyond 20 generations.

6. SUMMARY AND CONCLUSIONS

The present work is a preliminary attempt to invert water column sound speed profile using measurements of impulse response in shallow water. The multipath travel time information is extracted from impulse response data for two source receiver ranges of 245m and 320m. A forward propagation model based on ray tracing is implemented to model multipath travel times and compared to measured data. An objective function which computes the mismatch between measured and modeled travel time is optimized to obtain the best fit model of water column sound speed profile. In this work, inversion procedure based on a Genetic Algorithm is implemented to solve the optimization problem. Based on the inversion results obtained using the two datasets, the following conclusions are made regarding the feasibility of the inversion technique as a complementary method of measuring sound speed profile.

At 245 m range, the slope and depth of the thermocline agree well between the measured and inversion estimated profiles. The improvement in accuracy is only marginal as the number of generations is increased from 10 to 20. However, it was noted that the reduction in value of the objective function may not translate to improvement in the estimated values of the sound speed profile. Results indicate that as the range increases to 320m, the performance of GA deteriorates and the mismatch between the inversion estimated and the measured profile increases. It is important to note that these results represent the sound speed profile in a range-averaged sense over the source receiver range whereas the measured data was observed near the source station. As the source receiver range increases, it is expected that the difference between the measured and estimated profile will increase.

7. ACKNOWLEDGEMENTS

8. REFERENCES

[1] D. B. Kilfoyle and A.B. Baggeroer, 2000. The state of the art in underwater acoustic telemetry.IEEE J. *Ocean. Eng.* **25**, 4-27.

[2] M. Siderius, M. Porter and P. Hursky, 2003. Measurements and modeling comparisons of underwater communications performance at three shallow water sites, *Proc. Oceans 2003 IEEE, Piscataway, NJ, USA.* **4**, 1773-1779.

[3] C. Bjerrum-Niese, L. Bjørnø, M. Pinto, and B. Quellec, 1996. A simulation toolfor high data-rate acoustic communication in a shallow-water time varying channel. *IEEE J. Oceanic Eng.,* **21**, 143-149.

[4]   M. Snellen, D.G. Simons, M. Siderius, J. Sellschopp, and P.L. Nielsen, 2001. An evaluation of the accuracy of shallow water matched field inversion results. *J. Acoustical. Soc. America,* **109**, 514-527.

[5]   A. Tolstoy, 1993. *Matched Field Processing for Underwater Acoustics*. World Scientific, Singapore.

[6]   M.S. Ballard and K.M. Becker, 2010. Inversion for range-dependent water column sound speed profiles on the New Jersey shelf using a linearized perturbative method, *J. Acoustical. Soc. America,* **127**(6), 3411-3421.

[7]   E. Svensson, 2006. Inverting acoustic communication signals for the sound speed profile, *J. Acoustical. Soc. America,* **120**(3), 1347-1355.

[8]   W. Munk and C. Wunsch, 1979. Ocean acoustic tomography: A scheme for large scale monitoring. *Deep-Sea Research*, **26**, 123-161.

[9]   A. Tolstoy, 1994. Simulated performance of acoustic tomography via matched field processing. *J. Comput. Acoust.*, **2**, 1-10.

[10]   M.I. Taroudakis and M. Markaki, 1997. On the use of matched field processing and hybrid algorithms for vertical slice tomography, *J. Acoustical. Soc. America,* **102**, 885-895.

[11]   M.I. Taroudakis, 2002 Ocean acoustic tomography, in Lecture Notes, ECUA2002, (Gda□sk University of Technology, Gda□sk, Poland), 77-95.

[12]   P. Gerstoft, 1994. Inversion of seismo-acoustic data using genetic algorithms and a posteriori probability distributions, *J. Acoustical. Soc. America*. **95**, 770-782.

[13]   D.F. Gingras and P. Gerstoft, 1995. Inversion for geometric and geoacoustic parameters in shallow water: Experimental results, *J. Acoustical. Soc. America*, **97**, 3589-3598.

[14]   M.B. Porter and H.P. Bucker, 1987. Gaussian beam tracing for computing ocean acoustic fields, *J. Acoustical. Soc. America,* **82**, 1349-1359.

[15]   Randy L. Haupt, A. Sue Ellen Haupt, 2004. *Practical Genetic Algorithms,* Second Edition, John Wiley & Sons, Inc.

Effect of sonic layer depth on acoustics transmission loss in deep waters-measurements and modeling

Padmanabham M.[1], G.V. Krishna Kumar[1] and P.V. Nair[2]
[1]Naval Science and Technological Laboratory, Visakhapatnam-530 027
[2]Naval Physical and Oceanographic Laboratory, Kochi-682021
padmanabham.m@nstl.drdo.in

ABSTRACT

A two ship experiment was conducted to study the impact of Sonic Layer Depth (SLD) on acoustic propagation in deep waters off west coast of India. Depth at the experimental site is found to be ~2000 m with very mild slope. While one ship transmitted CW pulses at two different frequencies (1000 Hz and 1600 Hz) from a fixed location, the other received the same at different (15 km and 28 km) using a three hydrophone array. The hydrophones are placed at three different depths (15 m, 45 m and 75 m) while the first hydrophone is in SLD zone the other two are below the SLD. During the experiment relevant environmental parameters such as sound speed profile, wind speed and sediment information were also collected. Analysis of sound speed profile reveals the presence of a very shallow SLD(~25 m). The acoustic data thus collected was analyzed and presented in this paper. Experimentally measured acoustics Transmission Loss (TL) levels were compared against the predicted using the ray theory based Gaussian beam acoustic model (BELLHOP). As expected the TL was found to be high for the receivers placed below the SLD(45 m and 75 m) than the one (15 m) inside the SLD. Also, minimum TL was noticed at two ranges (15 and 28 km) due to bunching of low grazing bottom bounced rays. Measured TL compared well with simple geometric spreading (17*log (range)) law for the hydrophone placed at 15m depth.

1. INTRODUCTION

Literature suggests[1-5] when an underwater device such as sonar transmits a signal; it undergoes morphological changes due to various environmental factors. These factors include variation of sound speed with depth causing changes in refractive index, presence of ocean boundaries causing multipath and scattering effects, high temporal and spatial variability of ocean environment causing fading of signal, presence of different types of sediments at the bottom boundary causing different attenuations *etc*. All these environmental factors put together determines how particular sonar performs in a given environment through a parameter called transmission loss (TL) in sonar equations. The TL of a location greatly influences the Signal Excess (in some context Figure of Merit) which in turn influences the detection ranges of sonars. Meaning that performance of any sonar system critically depends on the prevailing TL at the sonar operational site. Since the ocean environment is temporal as well as spatially varying, the TL also varies accordingly. Therefore it is prudent to conduct an experiment in the place of interest to arrive at TL statistics over period of time. The measured TL levels thus obtained are usually compared against the theoretically estimated levels to fine tune the theoretical models to suite the area of interest. It is in this context that a two

ship experiment was conducted in deep waters of southwest coast of India to measure TL at different ranges for two frequencies. The measured TLs thus obtained were compared against the simple geometric spreading law including the attenuation and also against the ray theory (BELLHOP) based propagation model predictions. The findings in this paper will have far reaching implications on the performance of variable depth sonar.

2. MEASUREMENTS AND ANALYSIS OF ACOUSTIC DATA

Two ships were engaged in the experimental setup for carrying out the TL measurements, while one ship transmitted the signals from a fixed location and the other received the same at different ranges upto a maximum range of 30 km. This experiment was conducted at a location, where the water depth was around 2000m. CW pulses of frequencies 1000Hz and 1600Hz were transmitted from a depth of 9 m and the same were received by a three element hydrophone array where the hydrophones are placed at 15 m, 45 m, and 75 m depths. The data recorder and hydrophones were tested and calibrated prior to the experiment. The array was lowered from a ship which is completely silent during the entire experiment. The data was recorded using digital recorder with a sampling frequency of 24 kHz. The measured data was corrected for hydrophone sensitivity and amplifier gain before being converted to pressure (Pa). Later, they were passed through a band-pass filter of width 50 Hz to improve the signal-to-noise ratio to estimate received level.
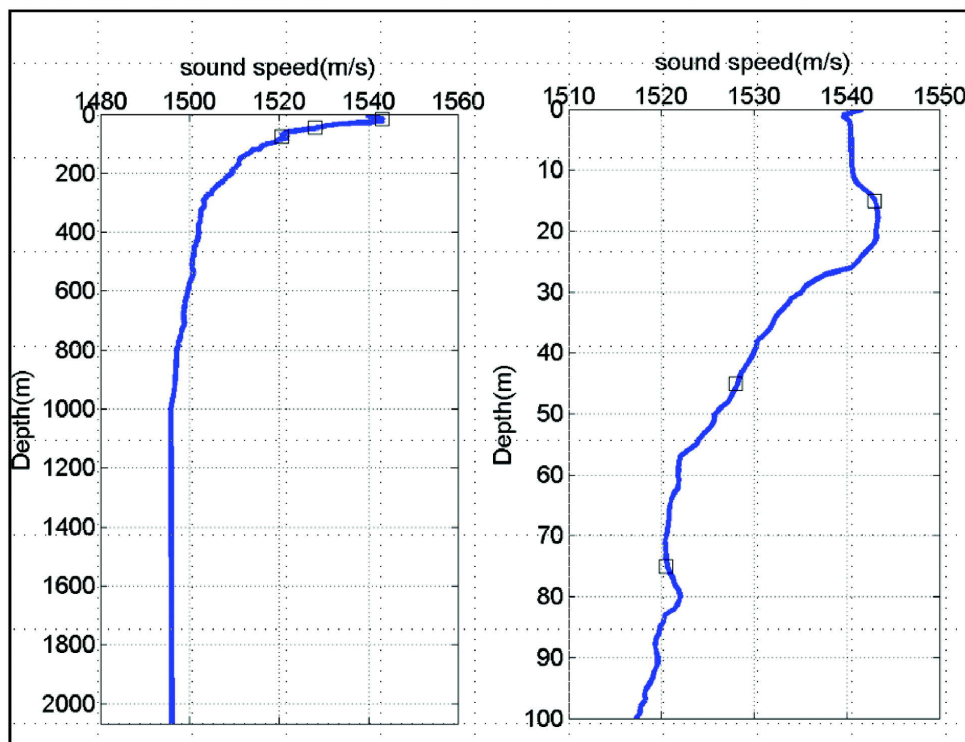

Fig. 1. Sound speed profile at the experimental site. Left panel full profile and right panel zoomed profile. The square boxes indicate position of hydrophones in the water column.

The TL values are calculated by subtracting source level from the received level. Along with acoustic measurements, CTD (Conductivity, Temperature, and Depth) profile was also collected to determine sound speed profile at the location. The calculated sound speed profiles using CTD data is plotted in Fig. 1. (Left panel full profile - Right panel zoomed profile). The figure clearly indicates the presence of shallow sonic layer (~25m).

3. NUMERICAL MODELING OF ACOUSTICS PROPAGATION

Ray theory methods are still used extensively in the operational environment where computational speed is a critical factor and environmental uncertainty poses much more severe constraints on the attainable accuracy. Therefore an Ocean acoustic propagation model based on ray theory, BELLHOP (http://oalib.hlsresearch.com/modes/acoustictoolbox/at.zip) was utilized to compute the TL.BELLHOP is designed in order to perform two-dimensional acoustic ray tracing for a given sound speed profile c (z) in ocean waveguides with attenuation or variable absorbing boundaries. The calculation of acoustic pressure is based on the theory of Gaussian beams. Ray tracing requires the solution of the ray equations to determine the ray coordinates. Amplitude and acoustic pressure requires the solution of the dynamic ray equations, which are described in3. For a system with cylindrical symmetry, the ray equations can be written as5,

$$\frac{dr}{ds} = c\xi(s), \qquad \frac{d\xi}{ds} = \frac{1}{c^2}\frac{dr}{ds}$$
$$\frac{dz}{ds} = c\zeta(s), \qquad \frac{d\zeta}{ds} = \frac{1}{c^2}\frac{dc}{dz} \qquad (1)$$

Here, r(s), z(s) represent the ray coordinates in cylindrical coordinates and s is arc length of the ray, c is sound speed, and the pair $[\xi(s), \zeta(s)]$ represents tangent along the ray.Initial conditions for, r(s), z(s), $\xi(s)$, $\zeta(s)$ are

$$r(0) = r(s),\ z(0),\ = z(s),\ \xi(0) = \frac{\cos(\theta s)}{c(s)},\ \text{and}\ \zeta(0) = \frac{\sin(\theta s)}{c(s)} \qquad (2)$$

Where [θ]s represents the launching angle, (r(s), z(s)) source position and c(s) is the sound speed at the source position. The coordinates are sufficient to obtain the ray travel time:

$$\tau(s) = \tau(0) + \int_0^s \frac{ds}{c(s)} \qquad (3)$$

Ray and dynamic equations are integrated in BELLHOP using a two-step polygon method. The standard measure in underwater acoustics of the change in signal strength with range is TL defined as the ratio in decibels between the acoustic intensity I(r, z) at a field point and the intensity I0 at 1-m distance from the source, *i.e.*

$$TL = -10\log\left(\frac{I(r,z)}{I_0}\right) \quad = -20\log\left(\frac{|P(r,z)|}{|P_0|}\right) \quad (dBre\ 1m) \qquad (4)$$
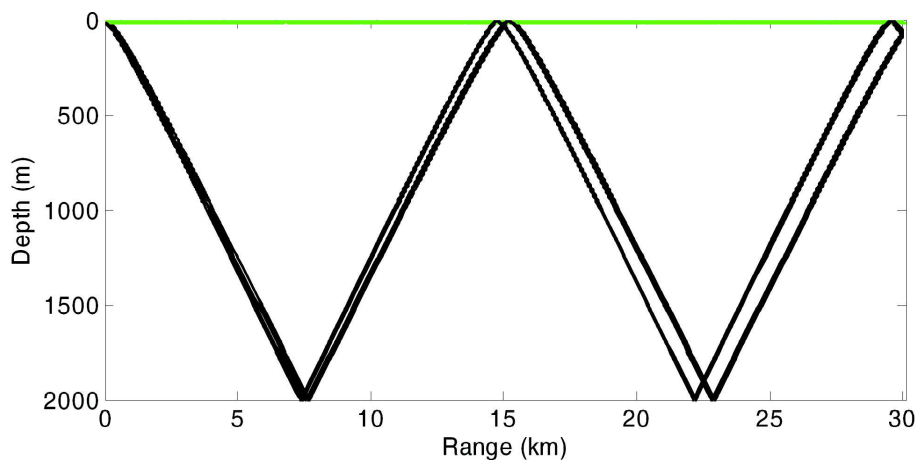

Fig. 2. The propagation of Eigen rays over the range of 30 km,
for source depth 9 m and receiver depth 75 m.

As brought earlier, the TL was estimated theoretically using BELLHOP model for all the experimental conditions, one such TL estimation for a source depth of 9m and receiver depth of 75 m for 30 km range is presented at Fig. 2. It is evident from the figure that till the SLD total area got insonified with two distinct shadow zones (first one is close to source region and the second is around 23 km range) created by low grazing bottom bounced rays. Bunching of rays have taken place around 15 km and 28 km, therefore the TL measured around this zone is ought to be less than the rest.

4. DATA AND MODEL COMPARISON

Comparisons between the measured TL and the ray theory (BELLHOP) based propagation model predictions for three receiver depths 15 m, 45 m and 75m for frequencies 1000 Hz and 1600 Hz are shown in Fig. 3. In
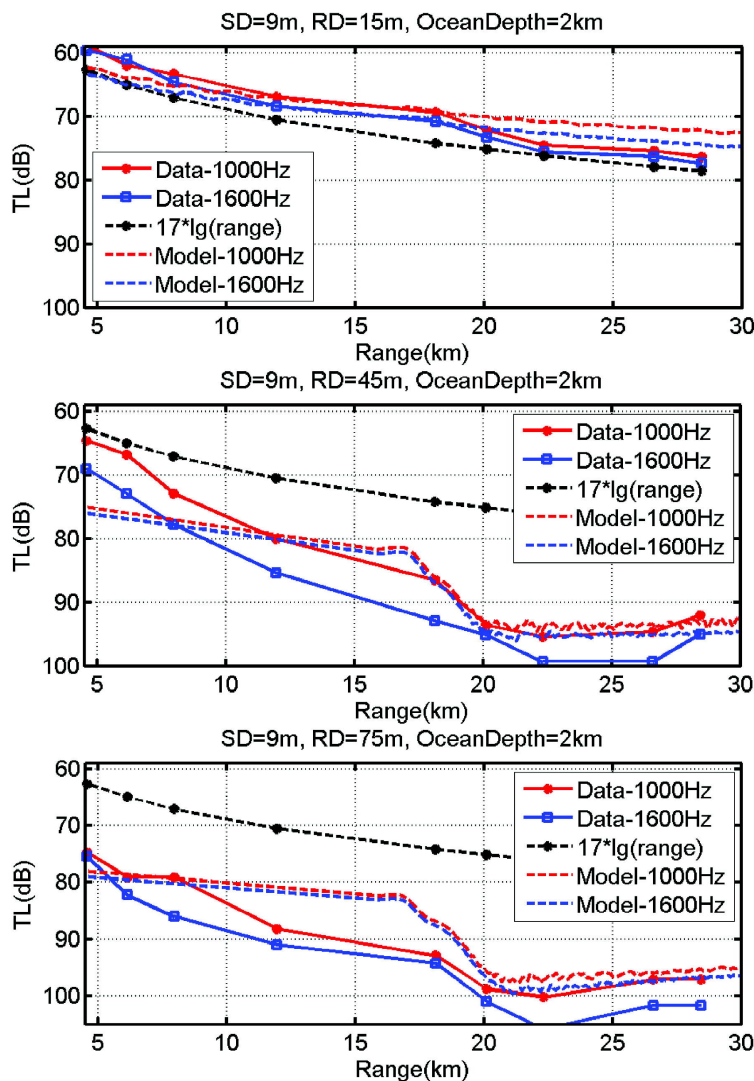

Fig. 3. Measured and modeled data comparison of TL for three receiver depths (15m, 45m, and 75m) for two frequencies (1000 Hz& 1600 Hz). black color broken line with filled circles represents simple geometric spreading, broken lines of red and blue color represents bellhop model based TL estimation for 1000 Hz and 1600 Hz respectively and similarly continuous lines with filled circle and unfilled square represents the measured data for 1000 Hz and 1600 Hz respectively.

addition to ray theory based propagation model predictions, a simple spherical spreading law with attenuation was also used in comparisons. It evident from Fig. 3 that the TL has increased with range across all the frequencies and receiver depths as expected. TL was slightly higher in case of 1600Hz compared to 1000Hz on expected lines owing to higher attenuation rates.

TL was noticeably higher for the receiver depths 45 and 75 m compared to 15 m as the former is placed below the sonic layer. As expected from the bunching of low grazing bottom bounce rays, the TL was lower at two ranges (15 and 28 km) than observed at other ranges. All these phenomena are well reflected in BELLHOP model predictions. The measured TL matched with the geometric spreading (17*log (range)) law with attenuation for the receiver depth 15m only which is due to the receiver in the sonic layer. Whereas for other receiver depths 45 and 75m, measured values were much higher than the geometric spreading law.

5. SUMMARY AND CONCLUSIONS

A two ship acoustic experiment was conducted to study the effect of sonic layer depth on acoustic wave propagation at a deep water site off west coast of India. Measured Transmission Loss (TL) levels were compared against the simple geometric spreading law (including attenuation) as well as with levels predicted using ray theory based model. A very shallow sonic layer depth was found to be present at the experimental site using the Conductivity, Temperature and Depth (CTD) profile data.

High TL was noticed for receiver depths 45 and 75 m, since these were placed below the sonic layer whereas the source was within the sonic layer. However, comparatively the TL was noticed to be lower at two ranges (15 and 28 km) due to bunching of low grazing bottom bounces in this region. Further, two low TL zones were also noticed, while one is close to source region and other is at 23km range. The data model comparisons reveal that the ray based model BELLHOP has been able to reflect the measured TL features with reasonable agreement. The measured TL matched with the geometric spreading (17*log (range)) law with attenuation for the receiver depth 15m which is in the sonic layer. Whereas for other receiver depths 45 and 75m, measured TL levels were much higher than the geometric spreading law.

6. ACKNOWLEDGEMENTS

7. REFERENCES

[1] R.J. Urick, 1983. Principles of Underwater Sound, 3rd ed., McGraw-Hill: New York.

[2] Qihu Li, 2011. Digital Sonar Design in Underwater Acoustics: Principles and applications, Zhejiang university press, China.

[3] M.B. Porter and H.P. Bucker, 1987. Gaussian beam tracing for computing ocean acoustic fields, *J. Acoustical. Soc. America*, **82**, 1349-1359.

[4] M.B. Porter,2017. Ocean Acoustics Library, BELLHOP http://oalib.hlsresearch.com.

[5] F.B. Jensen, W.A. Kuperman, M.B. Porter, and H. Schmidt,1994. Computational Ocean Acoustics (AIP, New York).

Generation of time domain reverberation profiles and evaluation with sonar sea trials data

Amit Kumar Verma and Sukhendu Sharma

Naval Science and Technological Laboratory, Visakhapatnam 530027, India
amitkumar.verma@nstl.drdo.in

ABSTRACT

Underwater Acoustic Reverberation causes primary limitation on Active Sonar system performance. Hence, impact of Active Sonar system design parameters on Reverberation needs evaluation. The power level simulation of Reverberation is done here and the time domain Reverberation envelope profile due to Volume, Surface and Bottom scatterings is generated. The model developed takes into consideration the 3 dimensional (3-D) array beam pattern from -90 to +90 degrees (both horizontal and vertical) including the side lobes. The output profile is generated by including all the Sonar parameters, Sonar-Sea Geometry parameters and Sea Environment parameters. Different envelope profiles are formed with different spreading losses and compared. Study is also done by generating envelope profiles with varying sea channel depths and Sonar operating depths. Performance evaluation of the model is also done by comparing the generated reverberation envelope with that of a Sonar sea trials' data envelope.

1. INTRODUCTION

Reverberation is the sum total of scattering contributions from sea boundaries and other in-homogeneities present in the sea and is the unwanted resultant of any Active Sonar transmissions. It causes primary limitation on sonar system performance. Hence, it is very pertinent that the impact of design assumptions on Reverberation be evaluated.

This paper discusses the generation of Sonar's Reverberation power envelopes (reverberation profiles) due to volume, surface and bottom scatterings. The model developed takes into consideration the 3 dimensional (3-D) array beam pattern from -90 to +90 degrees (both horizontal and vertical) including the side lobes. This work also compares the generated Reverberation profiles by varying parameters like depth of the channel, running depth of the Sonar and different propagation losses. Performance evaluation of the model is later done by comparing the generated Reverberation envelope with that of a Sonar sea trials' data envelope. The results discussed here are specific to a underwater weapon Sonar. But by using parameters from other sonars, the simulation model can be also be used for other sonars. Comparisons between generated reverberation profiles and sea trial data reverberation profiles will help us in direct evaluation of the impact of design assumptions.

The paper is organized as follows. The generation of the envelopes due to Reverberation is discussed in Section 2. The approach used for estimation of Reverberation for increasing range cells and the assumptions are discussed in this section. Section 3 dwells on the Matlab simulated results by varying parameters like

different spreading loss models, varying depth and geometry of the Sonar. Section 4 evaluates the generated power level Reverberation envelopes with Sonar sea trial data.

2. ENVELOPES DUE TO REVERBERATION

The Reverberation Level has been computed for all the three cases of Volume, Surface and Bottom. The total Reverberation power is the sum total of Volume, Surface and Bottom Reverberations' power which are discussed in this section. The parameters of Sonar depth, channel depth and Sonar pitch angle are taken from the Sonar operating geometry and conditions.

2.1 Approach

The envelope generated here due to the Reverberations is a power level profile. It is different from the Reverberation time series generation scheme[1,2] where the latter uses Rev-3D, 3-D ray-based model for computing time series for reverberation and propagation power delay.

The following are the intrinsic assumptions in our generation of power level Reverberation profile:

1. Primary Scattering only,
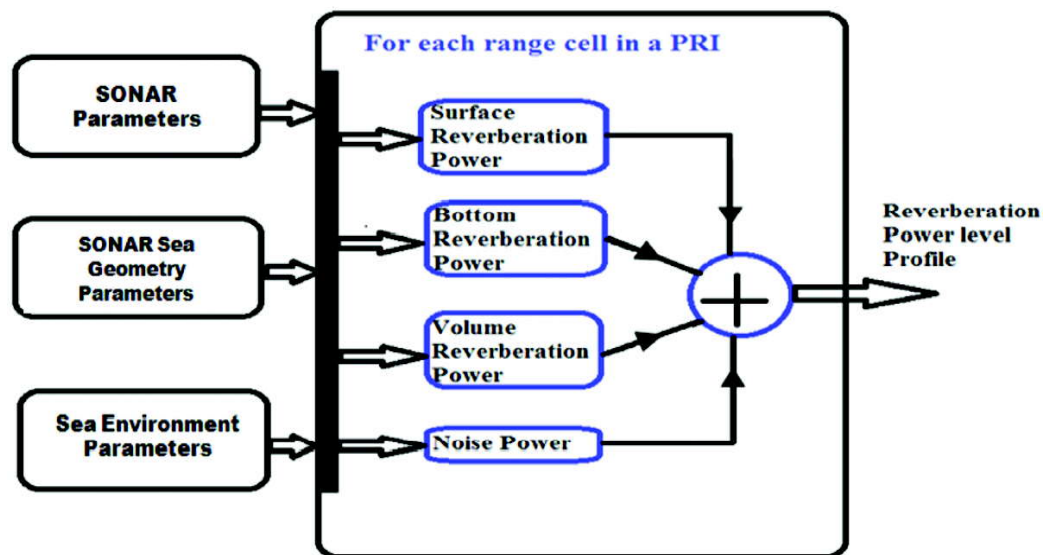2. Iso-velocity Sea environment
3. Direct Propagation path.

Fig. 1. Generation of power level Reverberation profile.

The combined Reverberation profile generation approach is shown in Fig. 1. The power level Reverberation profile is obtained by calculating the sum of powers due to Surface Reverberation, Volume Reverberation, Bottom Reverberation and noise for each of the range cells, as per Eqs. (1) and (2), in a Pulse Repetition Interval (PRI). Each of these Reverberations and noise power are generated based on the input parameters of

1. Sonar parameters, which include
   (a) Transmitter and Receiver 3-D beam patterns,
   (b) Transmitted Power (Source Level),
   (c) Time Varying Gain (TVG) and
   (d) Transmission pulse width.

2. Sonar-Sea Geometry parameters, which include
    (a) Sea Channel depth,
    (b) Sonar running depth and
    (c) Sonar pitch angle.
3. Sea Environment parameters, which include
    (a) Wind speed at the surface,
    (b) Noise Spectrum Level,
    (c) Volume backscatter strength,
    (d) Bottom condition and type (not considered here),
    (e) Bathymetry profile (not considered here), and
    (f) Propagation losses.

With these parameters, Reverberation power level computation is done at different ranges.

2.2 Reverberation power computation at different ranges

The elevation cut (azimuth angle = 0°) of typical transmission beam pattern is shown in Fig. 2(a). The figure shows the elevation beam pattern applicable for 0° pitch angle of the sonar and 0° elevation beam steering. If the pitch angle of the Sonar and the steering angle are different than 0°, the beam pattern will tilt up or down accordingly.
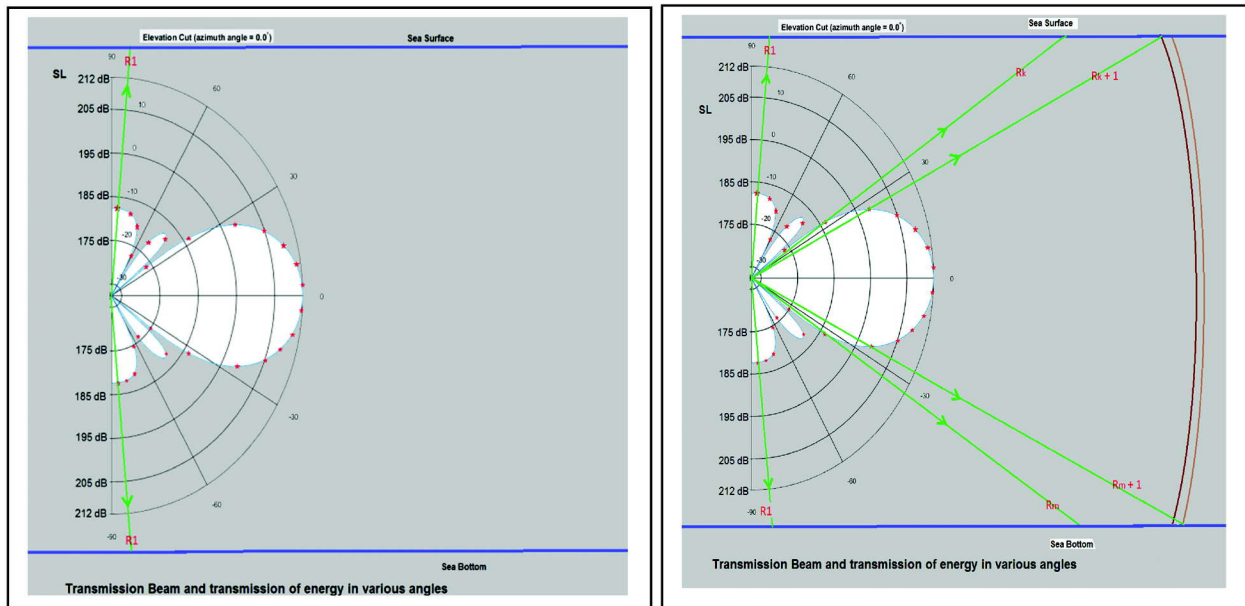

Fig. 2. (a) and 2(b).Transmission of energy in different elevation angles by Transmitter.

The elevation angle span is divided into incremental angular steps (say half a degree). All the angles in the 3D space are excited with different power levels by the sonar transmitter during the active transmission ping as per the beam pattern. Assuming peak Source Level (SL) of Sonar as 212 dB, the distribution of energy in the medium (sea) is shown in Fig. 2(a). The side lobes of the beam pattern in the 3D space are also included in the simulation, as shown in Fig. 2(b). This is because the rays emanating from these side lobes hit the sea boundaries at much less distance than the rays from the main lobe and hence have comparable reverberation power due to less transmission loss as compared to main lobe rays of the beam.

Fig. 2(a) shows the vertical cross-section of the transmitted beam. All the rays emanating from the source at elevation angles between 89.5° to 0.5° (if the angular step = 0.5°) will hit the sea surface at R_s range bins (cells), and will give rise to surface reverberation.

$$R_S = \frac{\text{Sonar depth from surface}}{\text{Sin } (\textit{vertical angle})}$$

Similarly, the rays emanating from the source at elevation angles between -89.5° to -0.5° (if the angular step = 0.5°) will hit the sea bottom at R_b range bins, and will give rise to bottom reverberation as shown in Fig. 2(b).

$$R_b = \frac{\text{Sonar height from bottom}}{\text{Sin } (\textit{vertical angle})}$$

Assuming $R_s = R_1$ and $R_b = R_1$, the transmitted energy is spread in the whole 3-dimensional hemisphere of radius of R_1 according to the transmitter beam pattern. The reflections from these will contribute to the sum total of surface, bottom and volume reverberations at range bin R_1 in the Receiver temporal data, assuming volume reverberation to be distributed uniformly in the medium. Similarly for different angles, different sets of range bins (based on time delays of the rays hitting the surface/bottom and returning back to the Sonar) will occur as shown in Fig. 2(b). The geometry will change for different combinations of channel depth and Sonar running depth and will result in different reverberation profiles. Similarly for typical receiver beam pattern, the elevation cut (azimuth angle = 0°) applicable for 0° pitch angle of the Sonar and for 0° oelevation beam steering is shown in Fig. 3. The beam pattern will tilt up or down according to the pitch angle of the Sonar.
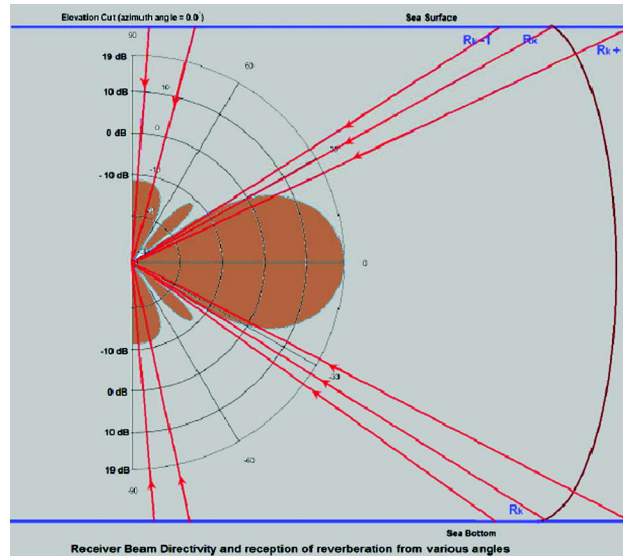

Fig. 3. Reception of reverberation from surface, bottom and volume of sea medium.

Here also, elevation angle span is divided into incremental angular steps (same as that used in transmission case). The combined received reverberation power is calculated for all the range bins as obtained earlier. The Receiver directivity is shown in Fig. 3. The surface, bottom and volume reverberations from different range bins (cells) are received at the receiver at different angles and these are multiplied with the receiver beam pattern (added in logarithm scale) to get the effective reverberation level at the receiver.

2.3 Volume Reverberation

Volume reverberation has been computed by using the relation

$$\text{RLv} = \text{SL} - 2*\text{TL} + S_V + 10 \log V \text{ dB.} \tag{3}$$

where, $V = (c\tau/2)\,\psi r^2$, the reverberating volume, SL : Source Level, TL : One-way Transmission Loss, r : range, S_V : Volume backscattering strength, c : speed of sound in water, τ : pulse width and ψ, is the equivalent 2-way beam width.

The directivity effect of the sonar is taken care by multiplying (adding in dB scale) the beam pattern of the receiver and transmitter beams to the calculated reverberation level, hence we have used $\psi = 4\pi$. The calculated value of volume reverberation level is added to Receiver Sensitivity of the transducers of Sonar and is converted to power levels as shown in equation below:

$$10^{\left(\frac{RL_D + RS}{10}\right)} watts \tag{3}$$

where RS is the Receiver Sensitivity in dB rel 1V/micropascal. It is to be noted that the Volume Reverberation's contribution to the total Reverberation is comparatively very less than Surface or Bottom Reverberation.

2.4 Surface Reverberation

The surface reverberation is computed only for the 3 dimensional elevation beams (rays) which are greater than 0 degree angles since these are the beams which will touch the surface. The range cells for the calculation of surface reverberation are computed using Eq. (1).

The surface reverberation can be calculated as:

$$RLs = SL - 2*TL + S_s + 10 \log A \quad dB \tag{5}$$

where, S_s – Surface scattering strength.

The sea surface scattering strength (S_s) is computed as a function of frequency, f (in kHz), wave height, h (in feet), and the grazing angle, θ [4].

The wave height is computed as a function of wind speed, W_s knots as

$$h = 0.0026 * W_s^{2.5} \tag{6}$$

For the range $\frac{5}{8} < fh \operatorname{Sin}\theta < 100$,

$$S_s = 10 \log(fh \operatorname{Sin}(\theta)^{0.99} - 45.3 \text{ dB.} \tag{7}$$

or,
$$S_s = 10 \log(fh \operatorname{Sin}(\theta)/K)^{0.99} \text{ dB.} \tag{8}$$

where, $K = 3.649 * 10^4$

In the region, $fh \operatorname{Sin}(\theta) < \frac{5}{8}$,

$$S_s = 10 \log(fh \operatorname{Sin}(\theta)/K)^4 \text{ dB.} \tag{9}$$

Again, in the region, $fh \operatorname{Sin}(\theta) > 100$

$$S_s = -26 \quad \text{dB.} \tag{10}$$

In Eqn. (5), A is the area of the surface scattering region in the range cell and is given by

$A = (c\tau/2)\phi r$, where ϕ, is the equivalent 2-way horizontal beam width,

The directivity effect of the sonar is taken care by adding in dB scale (multiplying) the beam pattern of the receiver and transmitter beams to the calculated reverberation level and hence we have taken $\phi = 2\pi$.

The surface reverberation is computed for all the range bins (cells) as computed from Eqn. 1,where the elevation and azimuth angles are incremented in steps of 0.5 degrees for every iteration. The calculated value of surface reverberation level is added to Receiver Sensitivity of the transducers of Sonar and is converted to power levels as shown in equation below:

$$10^{\left(\frac{RL_s + RS}{10}\right)} watts \tag{11}$$

where R_S is the receiver sensitivity dB rel 1V/micropascal.

2.5 Bottom Reverberation

The sea bottom is also an effective reflector and scatterer of sound and acts to redistribute in the ocean a portion of the incident sound. However, the bottom scattering strength, S_b, is a strong function of the bottom type, *e.g.* mud, sand, rock, *etc.* A large number of practical investigations have been carried out with varying degrees of consistency as discussed in literature[5]. We have used the Lambert's Law model[3]. This model gives the maximum expected bottom backscatter strength at normal incidence as -5 dB and is a good approximation for very rough sea bottoms.

The bottom backscattering strength S_b is given by Urick[3].

$$S_b = 10 \log(\mu) + 10 \log(\mathrm{Sin}\theta^2) \tag{12}$$

where $\mu = \dfrac{1}{\pi}$, and, θ is the grazing angle of the sound wave with the sea bottom.

Bottom reverberation will occur for all the elevation beams (rays) which are looking in the less than 0° degree angles for 0° pitch angle of Sonar. If the pitch angle is different from 0°, then the corresponding angles after adding the pitch angle are to be considered. For example, if pitch angle = –5°, bottom scattering will take place for vertical beam pattern angles from + 4.5° to -84.5° (*i.e.* the combined angle of beam pattern angle and pitch angle should less than 0°). The range cells for the calculation of bottom reverberation are computed by the Eq. (2).

Bottom reverberation has been evaluated from the equation below as:

$$RLb = SL - 2 * TL + S_b + 10 \log A \tag{13}$$

All the parameters have same value as in Eq. (4) except S_b.

The bottom reverberation is computed for all the range bins (cells) as computed from Eq. (12), where the elevation and azimuth angles are incremented in steps of 0.5 degrees for each iteration. The calculated value of bottom reverberation level is added to Receiver Sensitivity of the transducers of the Sonar and is converted to power levels.

The bottom reverberation power at sensor output is :

$$10^{\left(\frac{RL_b + RS}{10}\right)} watts \tag{14}$$

where RS is the receiver sensitivity dB rel 1V/micropascal.

2.6 Ambient Noise

The ambient noise is computed using the ambient noise spectrum level and receiver bandwidth. The average value of noise is converted to equivalent power level by using the receiver sensitivity.

$$NL = NSL + 10 \log(BW) \tag{15}$$

The NL is in dB, NSL in dB/Hz and BW in Hz.

The noise power at sensor output is given by

$$10^{\left(\frac{NL + RS}{10}\right)} watts \tag{16}$$

where R_S is the receiver sensitivity dB rel1V/micropascal.

Each of these reverberation powers (surface, volume and bottom) and noise powers for each range bins (cells) are added and this total power level is converted to voltage level. These values are then normalized to get an envelope due to combined reverberation.

2.7 Time Varying Gain (TVG) profile

The reverberation envelope is multiplied by theTVG (Time Varying Gain) profile used in the Sonar to get the final envelope.

2.8 Beam Patterns of Receiver and Transmitter

The 3D beam patterns for the receiver and the transmitter are generated through simulations and used in

the study. Chebyshev weightings are used for the elements in the generation of the beams. In our study, we are projecting the energy in all the 3D space in the channel depending upon the 3D beam pattern.

2.9 Transmission Loss

The transmission loss equation includes a spreading loss component and also an absorption loss component.

$$TL = \text{Spreading Loss} + \alpha * r/1000 \tag{17}$$

where, Spreading Loss $= 20 \log (r)$ for spherical spreading
$$= 10 \log (r) \text{ for cylindrical spreading,}$$

r is range in yards, and α is absorption coefficient in dB/kYd calculated from the expression due to Thorp[3] given as :

$$\alpha = \frac{0.1f^2}{1+f^2} + \frac{40f^2}{4100+f^2} + 2.75*10^{-4}f^2 + 0.003 \tag{18}$$

where f is frequency in kHz.

Because we considered primary path scattering only, spherical spreading loss (20 log r) has been considered in this work. However, envelopes considering cylindrical spreading losses have also been generated in Section 3 for a comparative study.

3. REVERBERATION PROFILES OF SONAR AT DIFFERENT DEPTHS

The envelope profiles have been generated by using the equations and parameters as discussed in the earlier sections. These envelopes are relevant to the particular Sonar, as we have used the Sonar parameters in the envelope generation. Similar envelope profiles can be made for other sonars using their specific parameters.

The simulations were done for different channel depths scenarios with sonar at varying depths. The envelopes so generated with the reflections from surface, volume and bottom surfaces and noise are shown in the plots below. In addition to these, different profiles are also generated with spreading losses forms like 20 log r and 10 log r. These envelopes so generated were then validated with Sonar sea trial data envelopes.

3.1 Envelopes for 400m deep channel for different depths of the Sonar:

These envelopes, as shown in Figs. 4(a)and 4(b),are generated for a 400m deep sea channel with various spreading loss (spherical and cylindrical) and different depths of the Sonar. It was found that 20*log(r)
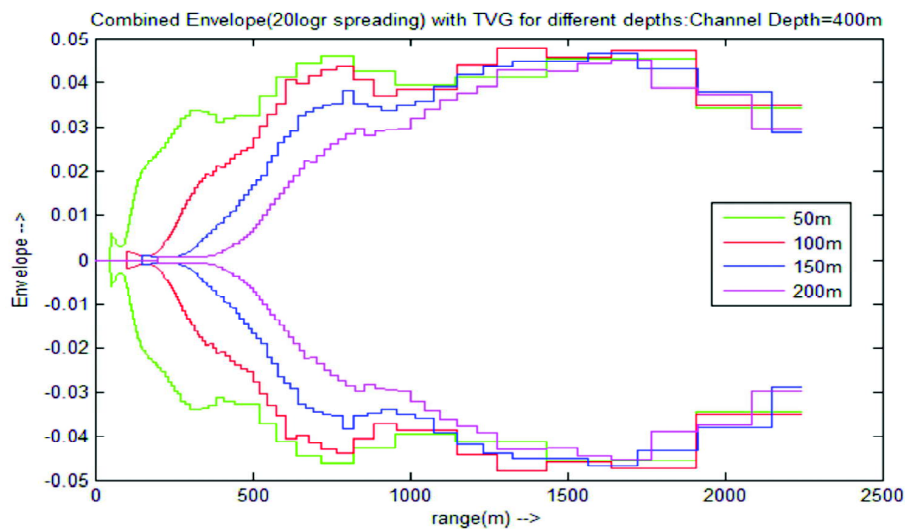

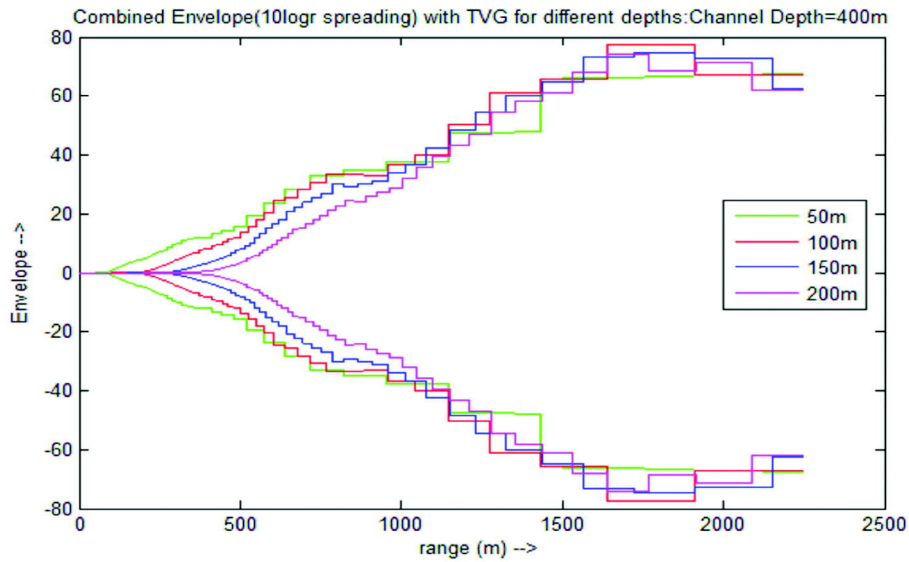Fig. 4(a). Combined Envelopes with Spherical spreading.

Fig. 4(b). Combined Envelopes with Cylindrical spreading.

(spherical spreading loss) was more suitable for our case as seen after comparing with the Sonar sea trials data profile (as discussed in Section 4).This is also true because we considered primary path scattering only. Henceforth, spherical loss has been considered for further envelopes generation.

3.2 Envelopes for 300m and 200m deep channel for different Sonar depths:

The envelopes in Figs. 5(a) and 5(b)are generated for a 300m and 200m deep sea channels respectively with spherical spreading loss and different depths of the Sonar. As can be seen from Figs. 4 and 5, the hump like pattern is more observed when the running depth is near to the sea surface. The hump like pattern in the envelopes is not due to Reverberations alone, but it is due to the combined effect of Reverberation plus TVG profile at shallow depths of operation. It can also be seen from Fig. 4(a), that the hump like pattern is not observed at Sonar running depth of 200m or more. But this can be a cause of concern for Sonar running depths of 150m or less.
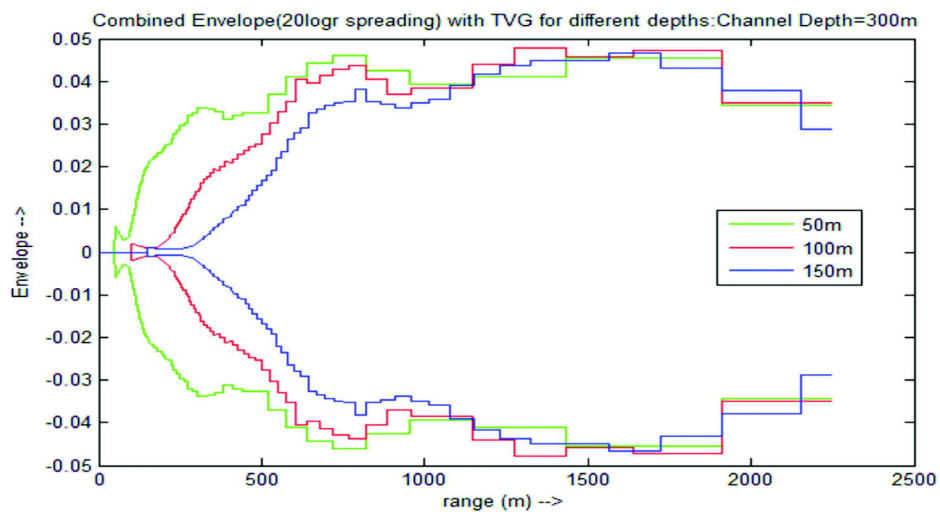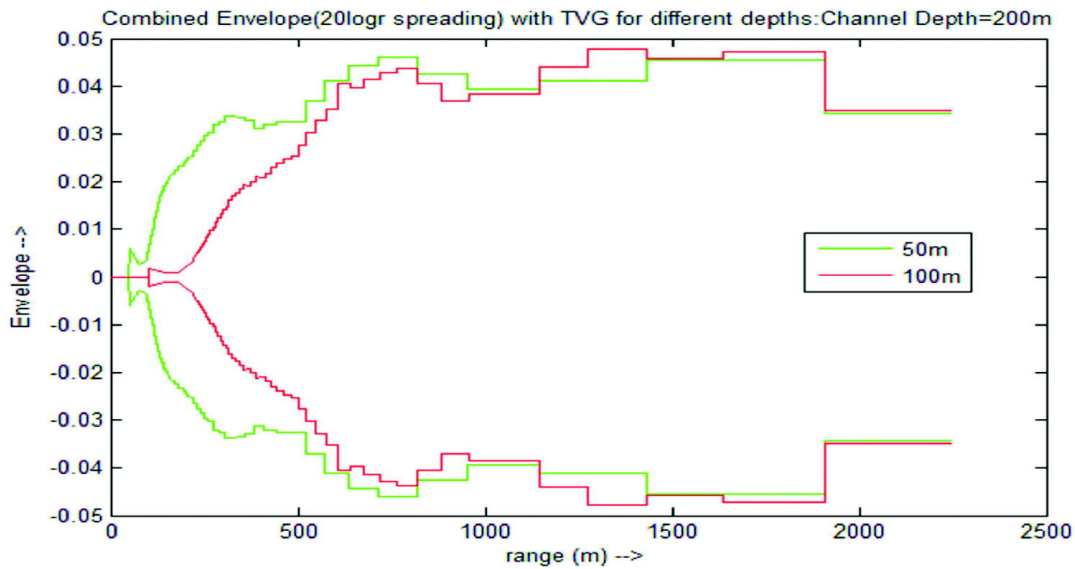

Fig. 5(a). Combined Envelopes for Channel depth = 300m.

Fig. 5(b). Combined Envelopes for Channel depth = 200m.

4. RESULTS EVALUATION WITH SEA TRIAL DATA

4.1 Scenario 1 (Channel 340m, Sonar depth = 140m):

This sea trial was done with Sonar running depth =140m and height of the Sonar from the bottom = 200m, *i.e.* channel depth =340m. Figure 6 shows the combined envelope (normalized) due to Surface, Bottom and Volume Reverberations alongwith the TVG gain profile in red colour. The generated combined profile is then validated with Sonar sea trial data profile. The Y axis in Figs. 6 and 7 represents digitized data of a 12-bit ADC at the Sonar receiver. As observed, the generated profile is in close concurrence with the profile observed in sea trials data.
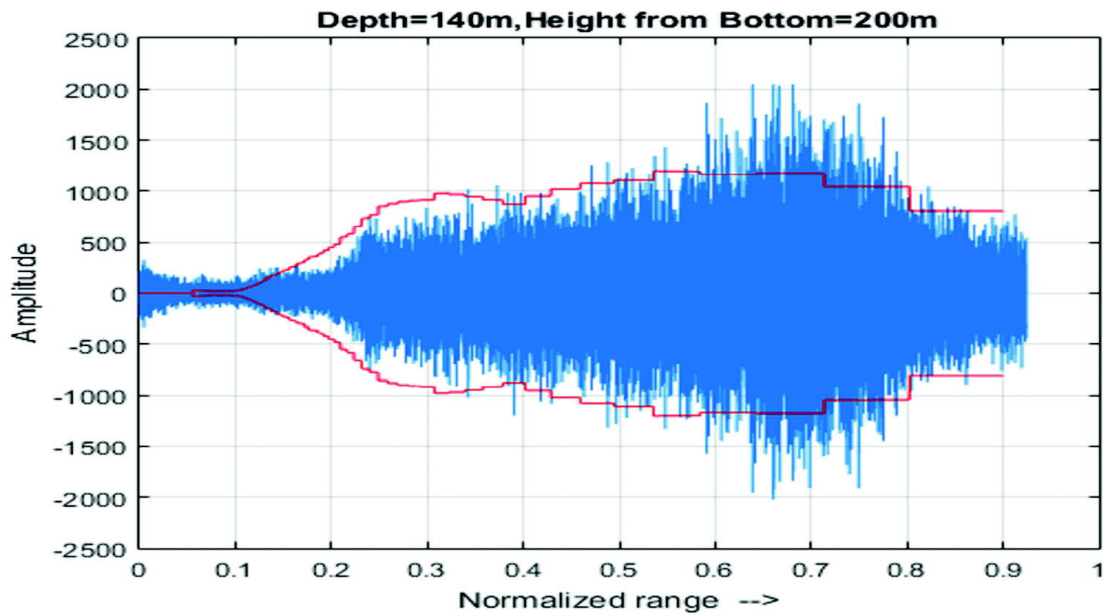

Fig. 6. Comparison with Sonar Sea Trial data.

4.2 Scenario 2 (Channel 340m, Sonar depth = 80m):

This sea trial was done with Sonar running depth =80m and height of the Sonar from the bottom = 260m, *i.e.* channel depth = 340m. Figure 7 shows the combined envelope (normalized) due to Surface, Bottom and Volume Reverberations along with the TVG profile in red colour and validates the combined profile with Sonar sea trial data profile. As observed, the generated profile is in close concurrence with the profile observed in trials data.
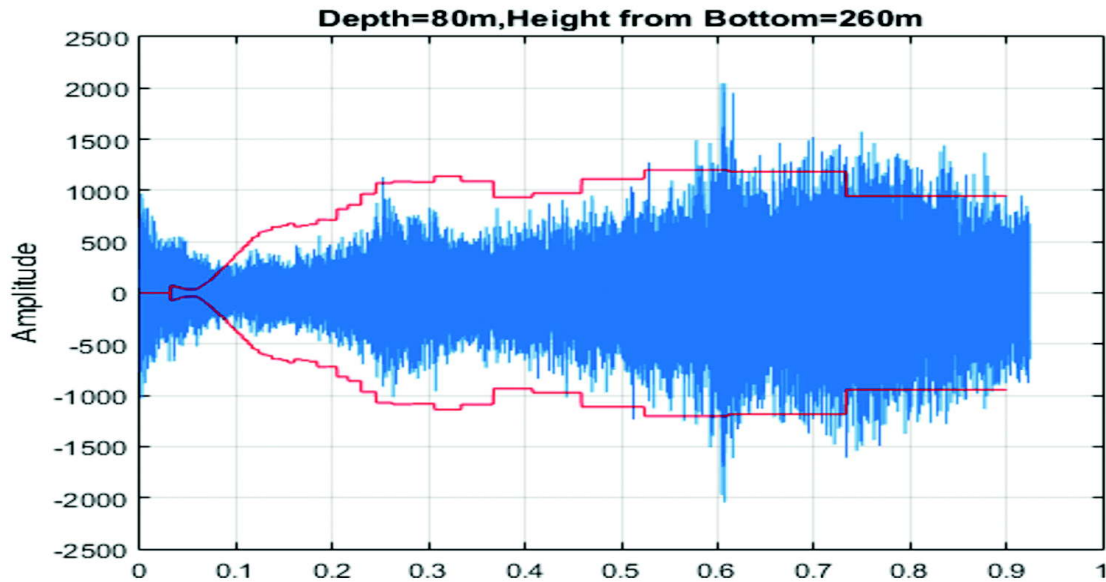

Fig. 7. Comparison with Sonar Sea Trial data.

5. CONCLUSIONS

The power level simulation of Reverberations was done and the time domain envelope profile was generated by multiplying Sonar's TVG profile with Reverberation profile. The output profile is generated by including complete transmitter and receiver beam patterns including the side lobes. The validation of the results was done with the Sonar sea trial data profiles. It was found that the generated envelope profiles were in good concurrence with sea trial data envelopes. Different envelope profiles were formed with different spreading losses and compared. Study was also done by generating envelope profiles with varying channel depths and torpedo running depths.

The developed model can be used for any array beam-patterns, TVG profile, channel depth and torpedo running depths. Comparisons between generated profiles and sea trial data profiles have helped us in direct evaluation of the impact of design assumptions.

This work can be further extended to generate Reverberation time-series generation. Also, Bottom Reverberation generation can be further improved by including dependence of bottom backscattering strength upon bottom type (mud, sand, silt, *etc.*).

6. REFERENCES

[1]   Stanley G. Chamberlain, 1983. A Model for Numerical Simulation of Nonstationary Sonar Reverberation Using Linear Spectral Prediction, *IEEE Journal of Oceanic Engineering*, **8**(1), 21-36.

[2]   Trond Jenserud and Sven Ivansson, 2014. Modeling the power delay profile of underwater acoustic channels-the effects of out-of-plane scattering and reverberation, *IEEE Underwater Communications and Networking(Ucomms)*.

[3]   Robert J. Urick, 1983. Ed., Principles of Underwater Sound, *McGraw -Hill Book Company*.

[4]   M. Schulkin and R. Shaffer, 1964. Backscattering of Sound from the Sea Surface. *J. Acoust. Soc. America*, **36**(9), 1699-1703.

[5]   How-Kin Wong and W.D. Chesterman, 1964. Measurements of Backscattering of Sound from the Ocean Bottom, *J. Acoust. Soc. America*, **36**(1), 158-163.

Performance analysis of acoustical image formation algorithms

Hareesh G., Manju Paul, Arun Kumar K.P. and Vijay Gopal G.
Naval Physical and Oceanographic Laboratory, Thrikkakara, Kochi, India
hareeshg@npol.drdo.in

ABSTRACT

In acoustical imaging, the backscattered signal at the receiver is represented as a sum of delayed and weighed replicas of transmitted signal which is used to insonify the imaging object or the scene. So in the forward problem, received signal is modelled using linear system model with a known transformation matrix and scattering coefficient vector. Estimation of scattering coefficients from the received signals is an inverse problem and the corresponding estimate is the acoustical image of the object or the scene. In this paper, we explore the feasibility of various linear estimation techniques to reconstruct the acoustical images of objects using simulation and also present a qualitative evaluation of their performances using experiment data.

1. INTRODUCTION

Underwater acoustical imaging provides vision under water. It uses sound waves to form images of underwater objects. An array of acoustic transducers sends out a beam of acoustic energy to insonify the imaging area that contains the target of interest and uses the reflections obtained to reconstruct the image. Reflectivity or scattering strength is the parameter that can be used to distinguish underwater objects from its background. Objects that have the ability to scatter most of the acoustic energy falling on it will appear prominent in the image[1-3].

In acoustical imaging, the imaging environment is modelled using a suitable signal model and the imaging problem is posed as an inverse problem. Analytical models are proposed by Freedman[4] and Faran[5] to explain scattering phenomenon of standard volumetric shapes in underwater applications. The scattered pressure in these models satisfies Helmholtz equation and Sommerfeld radiation condition. Inverse solutions of these models are computationally highly expensive due to the nonlinearities involved. Also the use of high frequency acoustic waves in imaging demands for high data rate to meet Nyquist sampling criteria. So in such high data rate acoustical imaging systems, inverting linear model has the advantage of lesser computational complexity. The forward model for underwater acoustical imaging given by George and Bahl[6] treats the imaging object as a collection of densely packed point scatterers or small facets. This approach is used for the signal model formulation as the model reduces to a linear system model.

In this model the received signal is modelled using a linear system model with known array steering matrix and scattering coefficient vector. In the inverse problem, the scattering coefficients are unknown which need to be estimated from the received signal with a given array steering matrix[2,7,8]. The focus of this paper is on the feasibility study and performance evaluation of different linear estimation methods that can be implemented in an imaging Sonar. In order to study the feasibility of these algorithms in real

signals, we conducted imaging experiments in an acoustic tank. The signals collected from these experiments are used for the qualitative evaluation of their relative performances.

2. SIGNAL MODEL

The data model presented in the papers[1,2] for underwater imaging applications is discussed here in the context of plane wave propagation. This model assumes that the imaged scene is composed of Q point scatterers and the ith scatterer is located at an azimuth angle 'θ' and range 'r' with reference to the co-ordinate origin. A point scatterer can be defined as a volume whose dimensions are very small in comparison with the wavelength and that follows Rayleigh's scattering process[2]. The reflectivity or the scattering strength of the ith scatterer

Fig. 1. Geometry of Acoustical Imaging

is c_i. The notation and geometry used in this model are shown in Fig. 1. The pressure scattered from the object is measured using a uniform linear array of transducer with M elements and inter element spacing (d) of half wavelength. Transmitter is a single element transducer with a wide horizontal and vertical beamwidth to insonify the imaging scene and it is placed along with the receiver array. Last sensor element (M) in the receiver array is located at the co-ordinate origin.

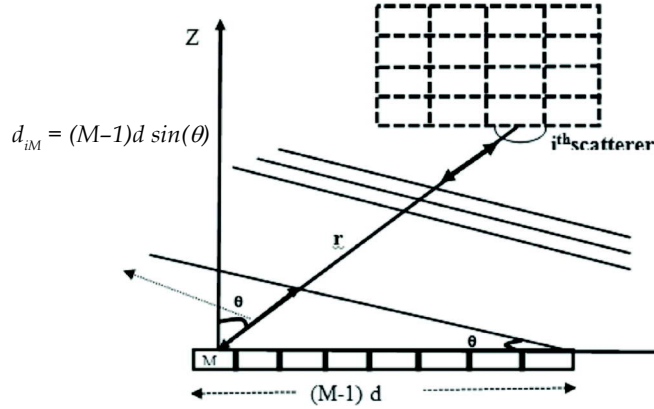The transmitter sends out a signal '$x(t)$' to insonify the imaging scene in the +Z direction. The emitted wave field propagates with velocity 'c' through the medium, experiencing attenuation and diffraction, as well as scattering and reflection. The reflected and scattered wave field propagates back towards the receiver array of elements, where upon reception the measured wave field is converted into electric signals. Received signal at the mth sensor '$S_m(t)$' can be represented as a sum of time-delayed and amplitude-weighted replicas of the transmitted waveform $x(t)$ i.e.,

$$S_m(t) = \sum_{i=1}^{Q} c_i \, x(t - \tau_{im}) \tag{1}$$

where, $\tau_{im} = d_{im}/c$.

τ_{im} and d_{im} are the time delay and path difference in arriving at m^{th} sensor after reflection and scattering from ith point scatterer respectively and c_i is the unknown coefficients of ith point scatterer that represent the scattering strength. From Fig. 1, we can represent Eqn. (1) in frequency domain as,

$$S_m(\omega) = x(\omega) \sum_{i=1}^{Q} c_i e^{(-j\frac{\omega}{c}(m-1)d\sin(\theta_i))} \tag{2}$$

The data model shown above can be represented in matrix form as

$$s(\omega, p) = U(\omega, p)c(\omega) \tag{3}$$

In Eq.(3), $s(\omega,p)$ is the M×1 column vector of the field received by M sensors placed at p = [0, d , …, (M-1)d], $c(\omega)$ is the Q × 1 column vector of scattering strength of each point scatterer contained in the scene to be imaged and $U(\omega,p)$ is an M × Q transfer matrix whose element $u_{im} = x(\omega)e^{(-j\frac{\omega}{c}(m-1)d\sin(\theta_i))}$.

Thus the imaging process reduces to estimating vector '$c(\omega)$' from the knowledge of U and signal vector s. The transformation matrix 'U' is the array steering matrix. This can be constructed a priori for a given

imaging scene and array geometry. Estimation of the unknown parameter 'c(ω)' can be done in different ways and some possible techniques are given in the next Section.

3. ACOUSTIC EXPERIMENT

Upon analysing the model discussed in Section 2, it is clear that the above model reduces to a linear form s = Uc. The measured signal vector 'y' is obtained by adding noise in the model and we get,

$$y = Uc + \varepsilon \tag{4}$$

where, ε is the measurement noise assumed to follow complex Gaussian distribution. Acoustical imaging problem can be formulated as finding the scattering coefficients 'c_i' of each scatterer in the above model. This problem can be viewed as a linear estimation problem. Least square and maximum likelihood estimators are the popular classical estimators for the above problem[8,9]. If we have some *apriori* knowledge about the unknown scattering coefficients, Bayes estimator is preferable[8,9].

Least square estimator (L2 norm minimization) finds the values of c that minimizes $\| y - Uc \|_2$. Least square estimator of c is

$$\hat{c}_{LS} = (U^H U)^{-1} U^H y \tag{5}$$

where, $(.)^H$ is the conjugate transpose operator.

For $\hat{c}_{LS}$ to exist, $U^H U$ must be invertible and U must have full column rank.

Maximum likelihood estimation (MLE) gives those values of scattering coefficients that maximizes the likelihood of getting the given sensor measurements. For noise with Gaussian distribution, MLE is same as least square estimation. So the maximum likelihood estimate of scattering coefficients is same as $\hat{c}_{LS}$ in Eqn. (5). Least square and maximum likelihood estimator are suitable for over determined systems, *i.e.* in cases where the sensor measurements can give adequate information about the scattering coefficients. That is the case, Q<M in Eqn. (3). Acoustical imaging usually deals with underdetermined systems and for such systems the matrix $U^H U$ becomes ill-conditioned. In such cases, least norm (Minimum norm) estimator guarantees a solution and it is the most preferred for underdetermined systems [1,2].

Least norm estimator minimizes L2 norm of the coefficient vector c subject to y = Uc . Solution is obtained by Lagrange multiplier technique, which is given by

$$\hat{c}_{LN} = U^H (UU^H)^+ y \tag{6}$$

where (.)+ is the Moore-Penrose pseudo inverse.

If prior information about the scattering coefficients is available in terms of a probability distribution, then Bayes estimator would be a good choice. This prior information is combined with the likelihood function to get a posterior distribution for the unknown parameter, from which the Bayes estimate is obtained by taking the mean of the posterior distribution, which minimizes the Bayes risk under squared error loss. If the measurement noise follow complex Gaussian distribution and the conditional prior density of the unknown coefficient vector *c* follows *N(0, k_cI)*, then the estimate can be obtained from the posterior density as [8,9,10,11].

$$\hat{c}_{BE} = (U^H U + k_c I)^+ U^H y \tag{7}$$

The term $k_c I$ is the scattering covariance matrix. From Eqn. (7), we can see that the term $k_c I$ in the Bayes estimator resolves the ill-conditioning problem of MLE[8,9]. Choice of a suitable prior is a practical problem in Bayes estimation.

When noise exists in the sensor data, instead of using Eqn. (6), the criteria used is, minimize L2 norm of the coefficient vector c subject to $\| y - Uc \|_2 < \xi$ where ξ is a positive constant[9]. The solution under this criterion is,

$$\hat{c}_{RLN} = U^H(UU^H + \xi I)^+ y \tag{8}$$

The above solution is known as L2 Regularized Minimum Norm (LRMN) solution and ξ is the regularization parameter which needs to be tuned for sensor data. This solution is expected to be less affected by the noise in the sensor data.

Estimators discussed above are computationally expensive due to the matrix inversion. One simple solution to imaging problem is popularly known as beamforming approach; it avoids finding the matrix inversion and is given by[1,2,13].

$$\hat{c}_{BF} = U^H y \tag{9}$$

From these studies, we can see that least norm, Bayes and Beamforming approaches are appropriate for solving underdetermined systems of equations. Estimators in Eqns. (5-9) can be viewed as a linear transformation of the vector y and the transformation matrix differs for different estimators. This matrix can be pre-computed for each steering direction of a given sensor array configuration in the desired range of frequency bins. This offers a great advantage for practical implementation as the pre-computed transformation matrix can be stored for further operations, thereby reducing the computational delay involved in the image formation.

Implementation of the above estimation techniques in an imaging Sonar are carried out using the following steps.

i. The signal received by the sensor array should be arranged into blocks of data with overlap between the blocks. This overlap is chosen so that it matches with the maximum delay.

ii. Discrete Fourier Transform (DFT) is carried out for this block of data and data samples falling in the desired range of frequency bins are selected to form the vector y in Eqn. (4). The number of samples in DFT must ensure that the time bandwidth product is very much less than one.

iii. Steering matrix U in Eq. (4) and corresponding transformation matrices in Eqns. (6-9) can be pre-computed for estimating the unknown scattering coefficients.

iv. Inverse DFT is carried out and exactly overlapping samples are discarded from the start of each block to form the beam output in time domain.

v. The technique of scan conversion is used to form the final display[14].

Performance analysis of the above algorithms is discussed in Section 4.

4. INVERSION METHOD

In order to validate the performance of the image formation algorithms discussed in Section 3, we conducted simulation study and also imaging experiments in the in house acoustic tank facility at NPOL. MATLAB is used for the simulation studies and processing of experimental data[15]. Array and waveform parameters used for the studies are shown in Table 1.

Table 1. Array and waveform parameters

Parameters	Values
Number of elements	32
Waveform	LFM
Centre Frequency (fc)	150 kHz
Bandwidth (BW)	50 kHz
Pulse Length	0.2 ms
PRI	6 ms
Sampling Frequency (Fs)	2 MHz
Imaging Object Range	1 m

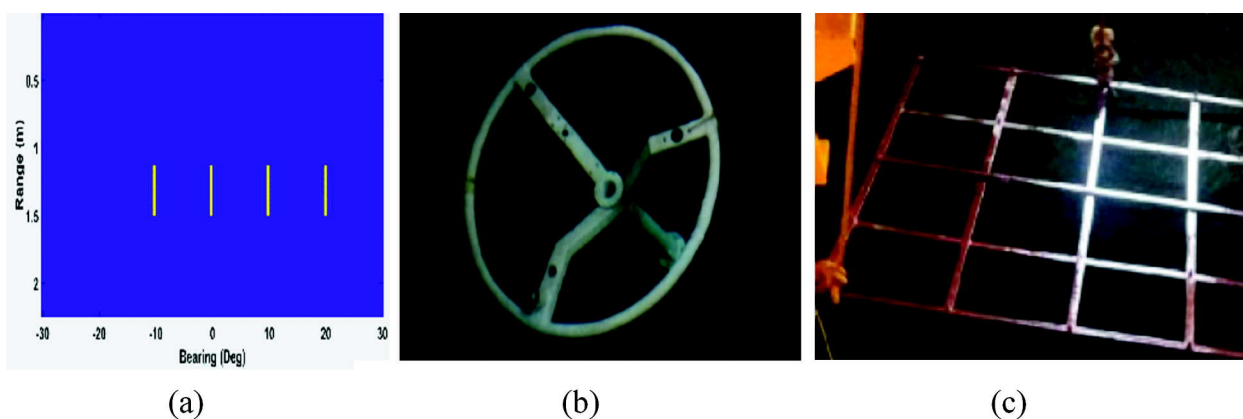(a)   (b)   (c)

Fig. 2. (a) The reference Image used for Simulation (b) & (c) Objects used for imaging Experiment

The test image considered for the simulation study consists of four lines in different bearing and extended in range cells as shown in Fig. 2(a). This test image is chosen for the simulation study as it is similar to the square mesh structure used for experiment. Inverse beamforming approach is used to simulate the frequency domain sensor signal from the image for a given imaging geometry. Zero mean complex Gaussian noise is added to the sensor data to simulate the measured signal. The noise variance is computed for different SNR. To study the performance of the reconstruction techniques, Mean Square Error (MSE) and Structural Similarity Index Measure (SSIM) are considered. Reconstructed images obtained under different estimation schemes and the test image is used for computing MSE and SSIM. From the simulation study it is seen that the Beamformer, Bayes estimator and LRMN perform equally well under different SNR.

The computed values of MSE and SSIM are not significantly different for these three techniques up to 4 decimal places. The corresponding values of MSE and SSIM are respectively 0.0033 and 0.9768 for 10dB SNR. The parameter k_c and ξ and are taken as 1 in the present study. Performance of least norm estimator is very poor in low SNR cases. At 10 dB SNR, MSE and SSIM are respectively 27.03 and -0.001 for least norm estimator. It indicates that the least norm estimators are very sensitive to noise.

A circular object shown in Fig. 2(b) and a 16 square mesh shown in Fig. 2(c) are used as imaging objects for tank experiment. The object is placed in a slanting position at 1m away from an array so that it lies in the vertical and horizontal beam of the array. Images obtained from different processing schemes discussed above are shown in Figs. 3 and 4. From the visual identification we can see that all the algorithms performed well in the experimental data but the conventional beamforming algorithm also perform equally well with minimum computational cost compared to other algorithms.
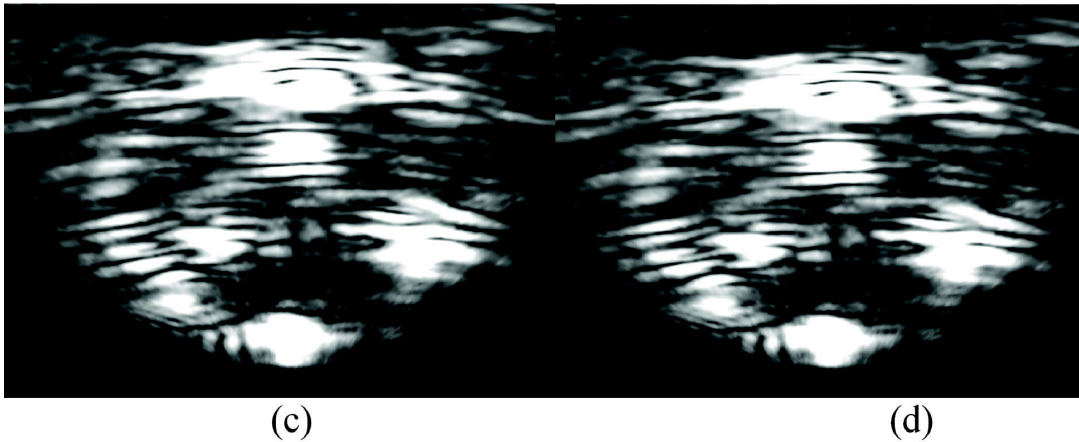

(a)   (b)
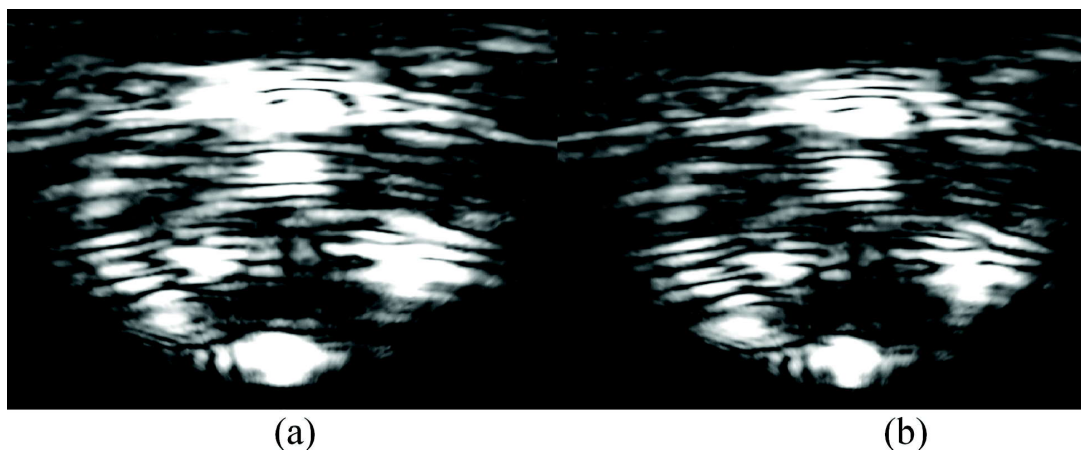
Fig. 3. Image of the circular object obtained using (a) Farfield beamforming (b) Least Norm estimation
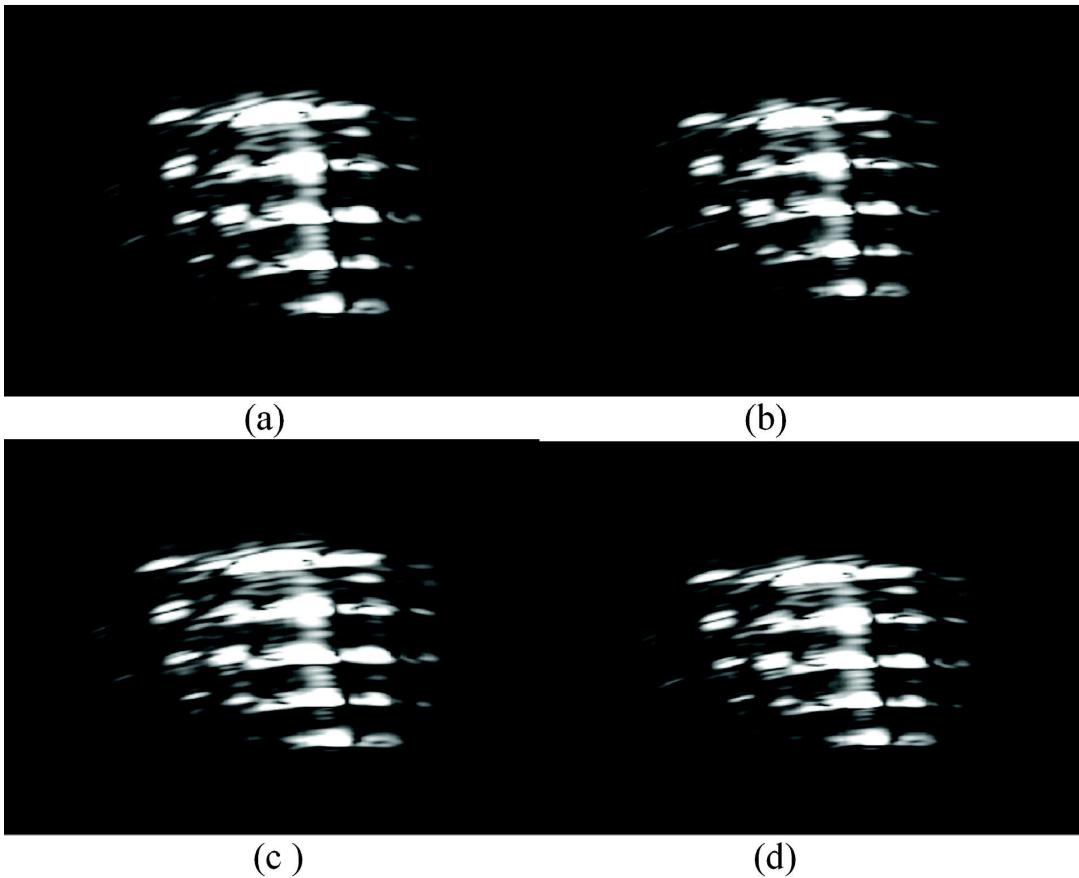(c) Bayes estimation (kc=1) (d) Regularized Least Norm estimation (ξ=1)

Fig. 4. Image of the mesh obtained using (a) Farfield beamforming (b) Least Norm estimation
(c) Bayes estimation (kc=1) (d) Regularized Least Norm estimation (ξ=1)

5. CONCLUSIONS

In this paper we surveyed various acoustical image formation algorithms which can be used for practical systems. Performances of these techniques are evaluated using simulation setup and also the signals collected

from controlled experiments. Conventional beamforming algorithm is computationally efficient among other algorithms under study and also it performs equally well with LRMN and Bayes estimators. Least Norm estimator is not a suitable candidate for image formation under low SNR cases. Sensitivity analysis of the regularization parameter in LRMN and scattering covariance matrix in Bayes estimator are not discussed in this paper. This can be studied along with sparse image reconstruction techniques[7,16] in future studies.

6. ACKNOWLEDGEMENTS

7. REFERENCES

[1] A. Trucco, M. Palmese, A. Fusiello and V. Murino, 2002. Three-dimensional underwater acoustical imaging and processing, Underwater Acoustic Digital Signal Processing and Communication Systems, Springer, Boston, MA, pp. 247-274.

[2] V. Murinoand and A. Trucco, 2000. Three-dimensional image generation and processing in underwater acoustic vision, *Proceedings of IEEE,* **88**(12), 1903-1946.

[3] J.L. Sutton, 1979. Underwater Acoustic Imaging. *Proceedings of IEEE,* **67**(4), 554-566.

[4] A. Freedman, 1962. The high frequency echo structure of some simple body shapes, *Acustica,* **12**, 61-70.

[5] J.J. Faran Jr., 1951. Sound scattering by solid cylinders and spheres, *J. Acoustic. Soc. America,* **23**, 405-418.

[6] O. George and R. Bahl, 1995. Simulation of backscattering of high frequency sound from complex objects and sand sea-bottom, *IEEE J. Oceanic Eng.,* **20**, 119-130.

[7] S. Mulleti, S. Nagesh, R. Langoju, A. Patil and C.S. Seelamantula, 2014. Ultrasound image reconstruction using the finite-rate-of-innovation principle, *Proceedings of the IEEE International Conference on Image Processing (ICIP),* pp. 1728-1732.

[8] J.G. Kelly and R.N. Carpenter, 1989. A Bayesian Approach to Acoustic Imaging and Object Classification by High Frequency Sonar. Technical Report Naval Underwater Systems Center.

[9] G. Kelly, R.N. Carpenter and J.A. Tague, 1992. Object classification and acoustic imaging with active sonar, *J. Acoust. Soc. America,* **91**, 2073-2081.

[10] A. O'Hagan, 1994. Bayesian Inference. Kendall's Advanced Theory of Statistics. 2B (First ed.). Halsted. ISBN 0-340-52922-9.

[11] K. Sekihara and S.S. Nagarajan, 2015. Electromagnetic Brain Imaging: A Bayesian Perspective, *Springer International Publishing.*

[12] J.R. Hald and J. Gomes, 2014. Method for reconstructing an acoustic field, *U.S. Patent,* **8**, 731-851.

[13] R.O. Nielsen, 1991. *Sonar Signal Processing*. Artech House, London.

[14] M. Ali, D. Magee and U. Dasgupta, 2008. *Signal Processing Overview of Ultrasound Systems for Medical Imaging*, SPRAB12-November, Texas Instruments.

[15] *Signal Processing Toolbox*, MATLAB. The Mathworks, Inc.

[16] M.F. Schiffner and G. Schmitz, 2011. Fast Pulse-Echo Ultrasound Imaging Employing Compressive Sensing, *Proceedings of the IEEE International Ultrasonics Symposium (IUS)*, pp. 688-691.

Low-frequency receiving sensitivity measurement of underwater transducers in small acoustic tank

Linthish P., S. Vasantha Kumari, Manoj N. Unni, R. Krishnakumar and R. Ramesh
Naval Physical and Oceanographic Laboratory, Thrikkakara, Kochi, India
linthish@gmail.com

ABSTRACT

Experimental methods developed for low-frequency receiving sensitivity measurement of underwater transducers in a small acoustic tank with real-time signal processing techniques are described in this paper. Low-frequency transducer measurement is not possible using conventional tone burst signals due to merging of reflection from the tank boundaries with direct signal from the transmitter. Short time broadband or transient signals are two good solutions to avoid these merging. High ambient noise and low signal level are the major constraints in the transient signal analysis of low-frequency underwater measurement where Signal to Noise Ratio (SNR) is very critical. Coherence between signals improves SNR. Different methods adopted to improve coherence are presented in this paper.

1. INTRODUCTION

Low-frequency measurements less than 4000 Hz can't be conducted using conventional tone-burst method in small tanks due to tank dimensional limitations and low-frequency projector (Transmitter) requirement. Alternate methods for low-frequency measurements with real-time signal processing technique are developed, which significantly reduce human effort and measurement time compared to conventional measurement techniques. Low-frequency signals usually merge with reflections from the tank boundaries due to small tank dimension compare with the wavelength under considerations. Short time, broadband signal (Transient Signal) is a good solution to avoid merging of these signals1. High ambient noise and low signal level are the major constraints in the transient signal analysis of low-frequency underwater measurements. Signal to Noise Ratio (SNR) can be improved by improving the coherence between signals. The present method improves the coherence between test and standard hydrophones within the limitations of the tank dimensions and available projectors. Also, real-time signal processing techniques in Lab-view are used for data acquisition, processing and display to reduce human effort and measurement time.

2. SIGNAL MODEL

Two experimental setups are described in this paper for low-frequency underwater sensor evaluation in a small tank of dimension 4m × 3m × 3m. The first setup is for the measurement at frequencies 100 Hz and above, and the second setup is for the measurement of ultra-low frequencies from 10 Hz to 100 Hz[2-4,7,8].

---

3. SETUP 1: MEASUREMENTS AT FREQUENCIES > 100 HZ

3.1 Measurement procedure

Receiving sensitivity measurement set up is shown in Figure 1. The projector is positioned at the centre of the tank at a depth of 1.5 m. Test and standard hydrophone are positioned at the same depth on either side of the projector using platforms A and B. Distance between the projector and the hydrophones are 1 m after considering the far field criteria D^2/λ, where D is the maximum dimension of the transducer used. This setup also minimizes the effect of reflections from the tank boundaries[5].
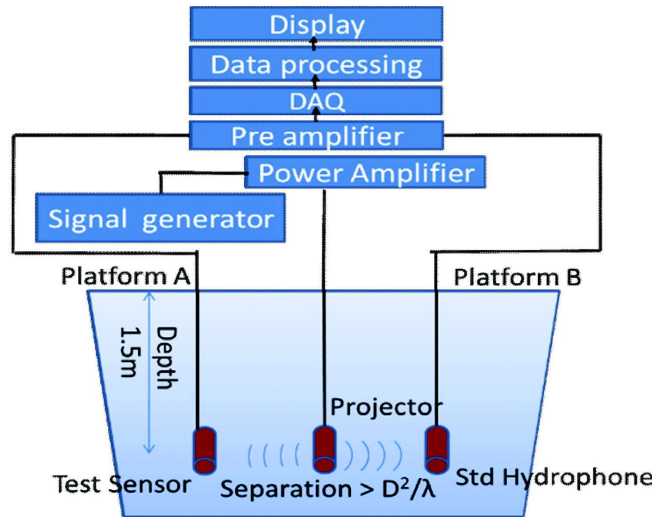

Fig. 1. Receiving Sensitivity measurement setup in the small acoustic tank

Instruments used for measurement are:

1. Standard hydrophone : B&K 8105
2. Test hydrophones : NPOL hydrophone and B&K
3. Transmitter : TR 25 MASSA
4. Signal generator : Agilent 33522A or NI PXI
5. Power amplifier : Instruments Inc. L-6
6. DAQ : Agilent DSA 35670A or NI PXI
7. Data analysis : DSA Analyzer or LabVIEW

Signals generated by the signal generator are first amplified by a power amplifier and transmitted through the projector. Standard and test hydrophones are placed on either side of the projector. The signals received from the standard and test hydrophones are then fed to a preamplifier for signal conditioning, mainly filtering and signal amplification. Amplified signals from the preamplifier are then simultaneously monitored using a DAQ system by applying same window settings for both test and standard hydrophone signals. The frequency response function and coherence between test and standard signals are measured by setting proper signal processing parameters. Window length is applied in such a way that reflections do not appear inside the window selected and the coherence is 1 for frequencies greater than 100 Hz. The receiving sensitivity (RS), is calculated using the relation

$$RS \text{ (dB)} = 20 \log [(V_{tst}/V_{std})(d_{tst}/d_{std}) M_0] \tag{1}$$

Where V_{tst} and V_{std} are the voltages generated by test and std. hydrophones, respectively, d_{tst} and d_{std} are the distance of test hydrophone and std. hydrophone with projector respectively and M_0 is the sensitivity of standard hydrophone[5].

4. MAJOR CONSTRAINTS AND ITS SOLUTIONS FOR LOW-FREQUENCY MEASUREMENT > 100 HZ

Merging of reflection and direct signal and poor SNR are the major constraints of low-frequency receiving sensitivity measurement above 100 Hz. Some means to handle these constraints are given in Table 1.

Table 1. Low-frequency measurement constraints and its optimization

Constraints	Solutions
Merging of reflection with the direct signal	1. Short time signals with broadband characteristics. eg. short time LFM or half sine signals
Low Signal to Noise Ratio (SNR) due to high ambient noise and low signal level	1. Simultaneous acquisition of standard and test hydrophone signals and positioning of these hydrophones in the tank, satisfying far filed criteria.
	2. Increase transmission level by using a proper projector and maximum possible amplitude level without any distortion.
	3. Use low noise DAQ. A system with good MDL (Minimum Detection Level).
	4. Use signal processing techniques to improve signal quality by applying filters, windows and averaging.

5. CONSTRAINTS 1: MERGING OF REFLECTION WITH THE DIRECT SIGNAL

Conventional measurement methods use tone burst signals for underwater transducer evaluation. Tone burst signal is a single frequency pulse, generated using sinusoidal waveforms having a fixed amplitude and pulse length. Typical tone burst signal from a transducer is shown in Figure 4.

A tone burst signals have three important regions; (1) build-up phase, (2) steady-state phase and (3) decay (Ringing) phase (See figure 4). Initial cycles of a transducer signal may not be having constant amplitude and phase. The amplitude will slowly build up and reach a steady state value; this region is known as build-up phase. The steady-state region is a region where the signal follows pure sinusoidal function. Amplitude and phase will be constant in this region and can be used for measuring signal parameters. Transducer signal will not stop suddenly even if we stop the input signal to the transducer. It rings for a few cycles and slowly decays and stops. This region is known as the ringing region or decay phase.

Long wavelength, low-frequency signals will cover the entire tank dimension within its 2-3 initial cycles (build-up phase), and start reflects back from the water surface or tank boundaries. Low-frequency signals, especially less than 4 kHz, these reflections will merge with the direct signal, before its achieving steady state phase. And it is not possible to calculate signal parameters without getting a steady-state region. Therefore, the low-frequency measurement using tone burst signals is limited by tank dimension. Experimental demonstration of signal merging is given in Figures 2 & 3.

Broadband signal: Broadband signals contain multiple frequency components in its frequency domain data, for example, impulse signals and LFM signals. Figure 4 shows the frequency domain data of tone burst signal and a broadband half sine signal (Impulse). Half sine signals contain frequency components from 0- $3f_0$, where f_0 is the fundamental frequency used for half sine generation.

Short pulse and broad frequency spectrum are the advantages of half sine signal. Because of its short length, merging of reflection and the direct signal can be easily avoided, as shown in Figure 5. Similarly, LFM signal also contains many frequency components in the frequency domain. Pulse length can also be controlled such that the direct signal can be well separated from the reflected signal. Typical LFM signal
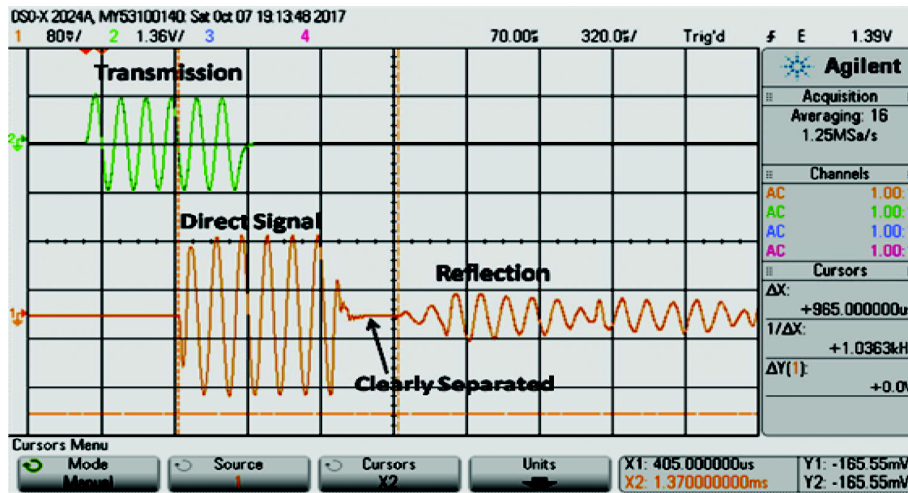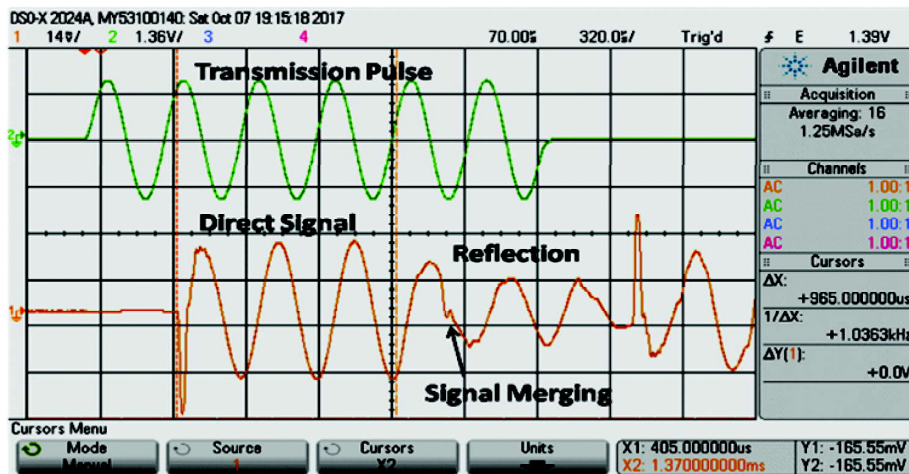
Fig. 2. Six cycles of 9 kHz signal
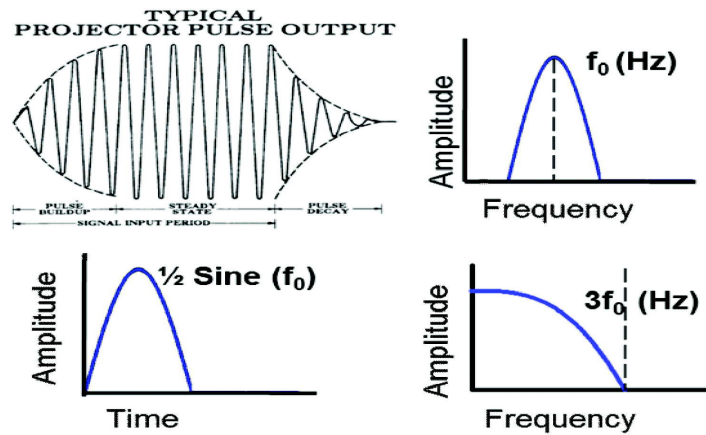

Fig. 3. Six cycles of 3 kHz signal

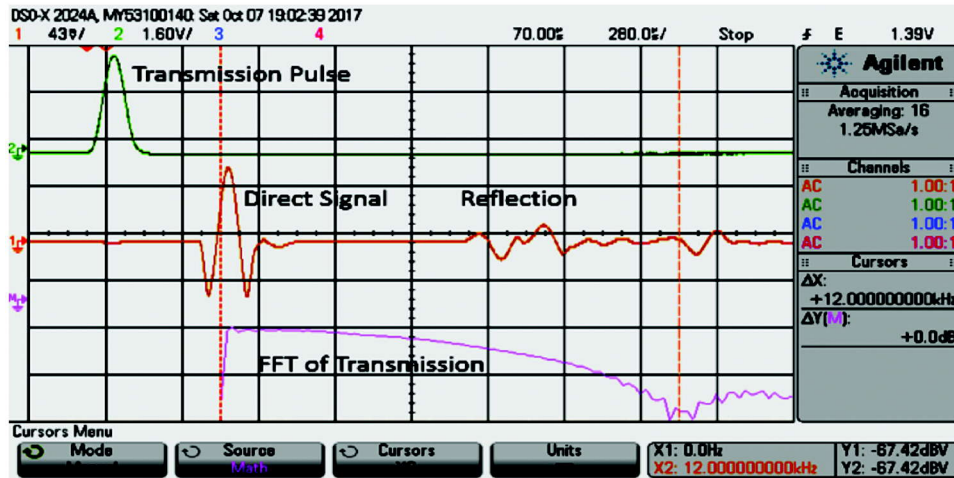Fig. 4. Signals and its frequency domain data

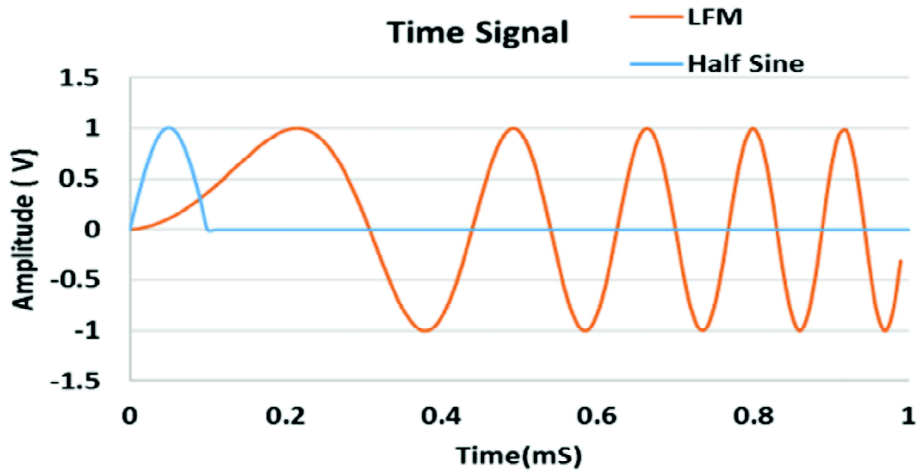Fig. 5. Four kHz half Sine signal and its FFT
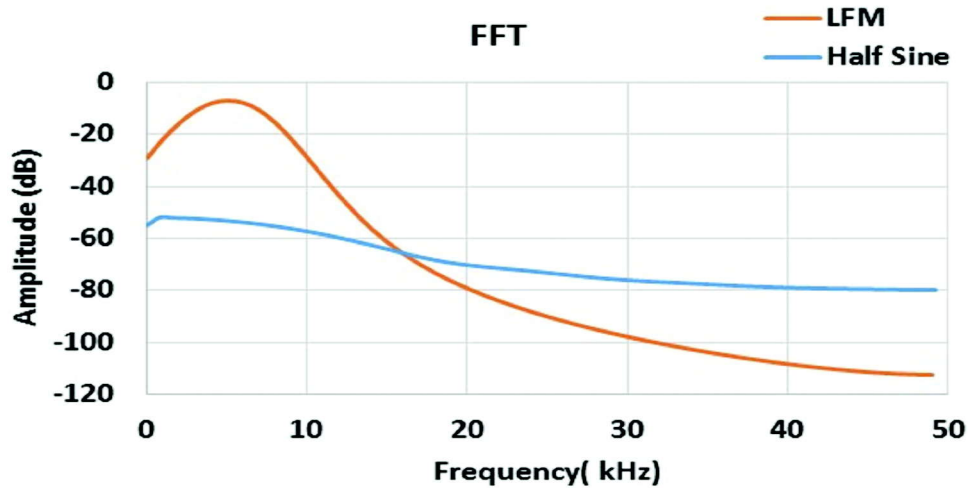

Fig. 6. LFM Signal and half Sine signal

Fig. 7. FFT of LFM and half Sine Signal

and its frequency components are given in Figures 6 & 7. The advantage of LFM signal is that its amplitude values of the frequency components are much higher than that of half sine signal. Therefore, SNR will be slightly improved in LFM signal compared to half sine method.

The broadband signal also helps to calculate receiving sensitivity at different frequencies in a single pulse. Using instrument controlled LabVIEW programs, these signals can be acquired and process in real time. This will also reduce the measurement time considerably compared to single frequency (tone burst) sweeping technique [6,11].

6. CONSTRAINT 2 : LOW SNR DUE TO HIGH AMBIENT NOISE AND LOW SIGNAL LEVEL

Coherence is a measure of the degree of linear dependency of two signals at all frequency components. If two signals correspond to each other perfectly at a given frequency, the magnitude of coherence is 1. If they are totally unrelated coherence will be 0. SNR and coherence are related by the Eqn. (2)[7].

$$\text{SNR= Coherence / (1-Coherence)} \tag{2}$$

Therefore, improving the coherence will improve the SNR. High levels of low-frequency ambient noise will alter the linear dependency of signals from standard and test hydrophone. Therefore, the coherence will be poor especially in low-frequency region.

Simultaneous acquisition of standard and test hydrophone signals will improve the correlation between signals. Thus the coherence also will improve between signals. The positioning of these hydrophones in the tank on either side of the projector at the same depth, satisfying far filed criteria (D^2/λ), plays a key role to improve coherence between test and standard hydrophone signals.

SNR also improves with the amplitude level of the transmitted signal. Transmission level depends on the TVR value of the projector. TVR values decrease by 12 dB /octave at frequencies below the fundamental resonance. Therefore, it is necessary to use a projector which resonates at low-frequency in order to improve SNR. Size of the transducer increases significantly for achieving resonance at very low frequencies. This will increase the far field distance. Though the size of the transducer and the transmission level are to be optimized.

The received signal can be acquired by a data acquisition system using instrument control LabView programs[6,11]. The amplitude of low-frequency components in the received signal will normally be very low and comparable with the ambient noise level. Therefore, the noise floor of the data acquisition system and capability of minimum detection level are important for achieving meaningful SNR. Minimum detection level of the instrument is dependent upon the bit resolution and input range of the instrument. The minimum measurable voltage level of the instrument can be calculated by the equation,

$$\text{Minimum detection level (MDL) = Input Voltage Range/}(2^{\text{Bit resolution}} -1) \tag{3}$$

SNR of the acquired data can be improved using different signal processing techniques. Some of the important signal processing techniques are (1) Averaging, (2) Filtering, (3) Windowing, (4) Zero padding and (5) FFT analysis.

Averaging in the time domain will reduce random noises and improve the signal to noise ratio. This also provides information about standard deviation and means value, which is useful in error calculation, while displaying results. Filters are used for eliminating unwanted frequency components from the measured data, which also improves SNR considerably. Windowing is an essential part of signal processing technique to avoid spectral leakages. Common windows which are used for measurements are rectangular, hanning, hamming, flat top etc. Every window has its own side lob level and main lob width. Generally, main lobe width and side lobe levels are inversely connected with each other. Therefore, selection of windows is a compromise between side lobe level and main lobe width. In our experiments, we have selected rectangular window for avoiding reflection and used zero padding of the data for better frequency resolution in FFT analysis. Basic flowchart of low-frequency measurement is given in Figure 8.
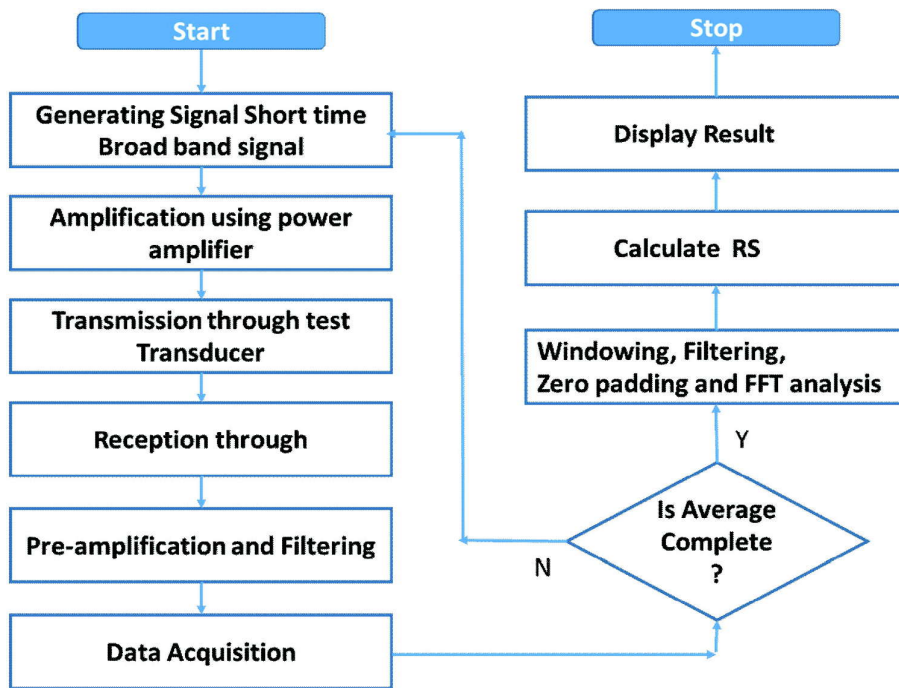
Fig. 8. Flowchart of Setup 1

7. VALIDATION OF MEASUREMENTS

This method is validated by comparing receiving sensitivity value of present method and the calibrated result of a NABL accredited Laboratory. A comparison of the results is shown in Figure 9. The results are in good agreement with each other, indicating the validity of the present method. Bruel & Kaejr (B&K) reference hydrophones are evaluated using the present method and the results are compared with the calibrated values of Original Equipment Manufacturer (OEM), evaluated at National Physical Laboratory (NPL), London. The details of comparison are given in Table 2. Maximum discrepancy observed is 0.7 dB within the frequency range of 100-4000 Hz.
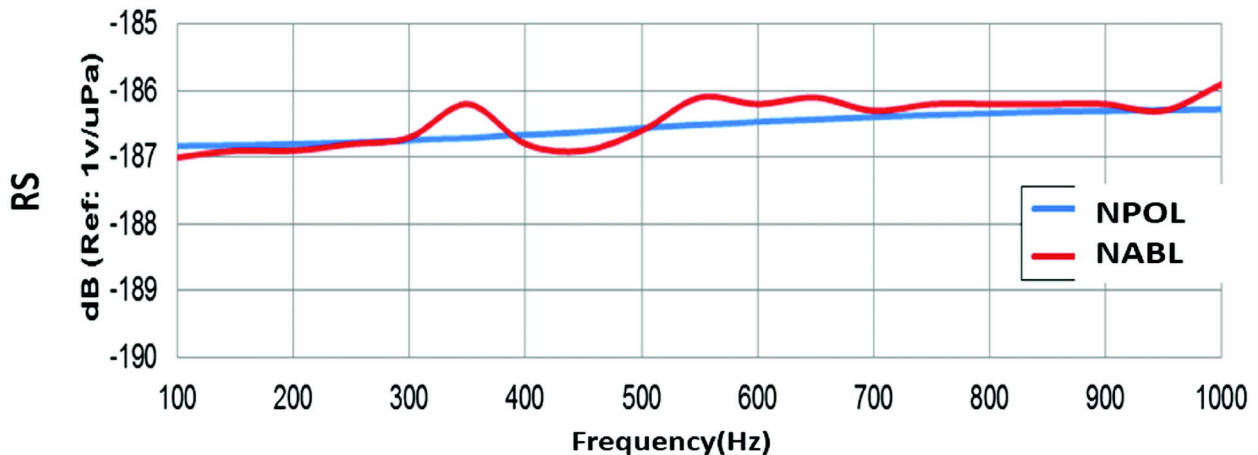

Fig. 9. Comparison of results obtained in the present method with that measured at NABL accredited Lab

Table 2. Comparison of RS measurement using the present method with the OEM calibration chart.

Hydrophone model and Serial No.	RS (dB)			
	Present method		OEM calibration chart	
	1 kHz	4 kHz	1 kHz	4 kHz
B&K 8100	-205.7	-205.7	-205.0	-205.0
B&K 8104_1	-206.9	-206.4	-207.6	-207.6
B&K 8105	-207.6	-207.4	-207.7	-207.7
B&K 8104_2	-208.8	-208.1	-208.3	-208.3
B&K 8105	-206.6	-206.6	-206.8	-206.8

8. UNCERTAINTY ANALYSIS

Type A and Type B uncertainties are calculated from the potential sources of uncertainty in the measurement procedure. Which are, reproducibility of the transducer positions, signal to noise variations between measurement sets, amplitude resolution of ADC, preamplifier and uncertainty exist in the calibration of the reference hydrophone. Type A uncertainty was calculated from nineteen independent measurement results. Type B uncertainty was calculated from the calibration chart of the hydrophone, and the instruments used. Expanded uncertainty was calculated by combining Type A and Type B uncertainty in quadrature with a coverage factor of 2 (95% confidence level) is +/- 1.3 dB[8-10].

9. SETUP 2 LOW-FREQUENCY MEASUREMENTS 10-100 HZ

Low-frequency measurement 10-100 Hz is not possible using setup 1 due to very high ambient noise and very low transmitted signal in the desired frequency range. An effective way of utilizing this high ambient noise for the evaluation of hydrophone is discussed here. Coherence between standard and test hydrophone can be improved by adopting good noise correlation techniques.

9.1 Measurement procedure

Test hydrophone and standard hydrophone are lowered side by side at a depth of 1.5 m from the water level in the middle of the acoustic tank. The experimental setup used for this measurement is shown in Figure 10.

Instruments used for the measurement are same as setup1. High-level ambient noise is used as the signal for evaluating the standard and test hydrophones (see Figure 11). The signals received from the standard and test hydrophones are feed to a preamplifier for signal conditioning, mainly filtering and signal amplification. Amplified signals from the preamplifier are then simultaneously monitored using a DAQ system by applying same window settings for both test and standard

Fig. 10. Receiving Sensitivity measurement setup for 10-100 Hz in the small acoustic tank

hydrophone signals. The frequency response function and coherence between test and standard signal are measured by setting proper signal processing parameters. It is ensured that the coherence between 10-100 Hz is greater than 0.9 so that signal correlation between standard and test hydrophone is high. The receiving sensitivity is calculated using, the relation,
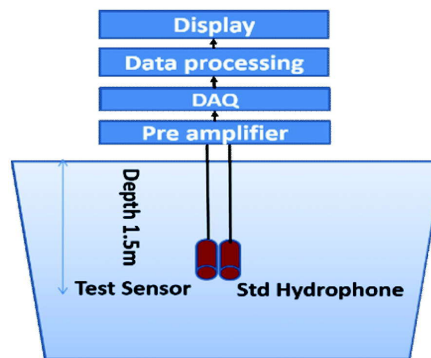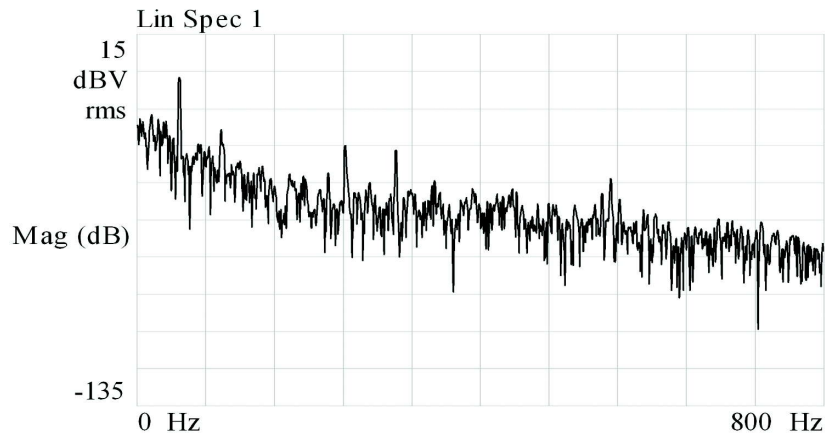
Fig. 11. Ambient noise level in the small acoustic tank

$$RS\ (dB) = 20 \log\ [(V_{tst}/V_{std})\ M_0] \qquad\qquad (4)$$

where V_{tst} & V_{std} are the voltages generated by test and std. transducer respectively and M_0 is standard hydrophone sensitivity value.

10. MAJOR CONSTRAINTS AND SOLUTIONS

Standard and test hydrophones need to experience the same pressure field for comparative calibration of hydrophones. Getting good correlation between standard and test hydrophone and detecting this very low amplitude signals by a data acquisition system with sufficient amplitude resolution are the major constraints in low-frequency measurement from 10 Hz to 100 Hz. The details are given in Table 3. The basic flow chart of this measurement procedure is given in Figure 12.

Table 3. Low-frequency measurement constraints and its optimization.

| Constraints	Solutions
Correlation between std. test hydrophones	1. Noise correlation can be increased between standard and test hydrophones by placing them side by side in the middle of the acoustic tank
SNR improvement	1. The noise floor of the Data acquisition system required to be minimal as compared to the ambient noise level. Typical ambient noise level is given in Figure 11.
	2. MDL of the data acquisition system is very critical to detect the low ambient noise level. Need to choose instrument range and bit resolution accordingly so that the MDL of the instrument is minimal.
	3. Averaging is required to be very high, of the order of hundreds so that the uncorrelated noise components are minimized.
	4. Filtering of High-frequency components also improves the SNR
Frequency resolution	1. Frequency resolution needs to be very high for low-frequency measurement. Therefore, the memory capacity of the instrument is required to be high, so that it can record the data for a long time.
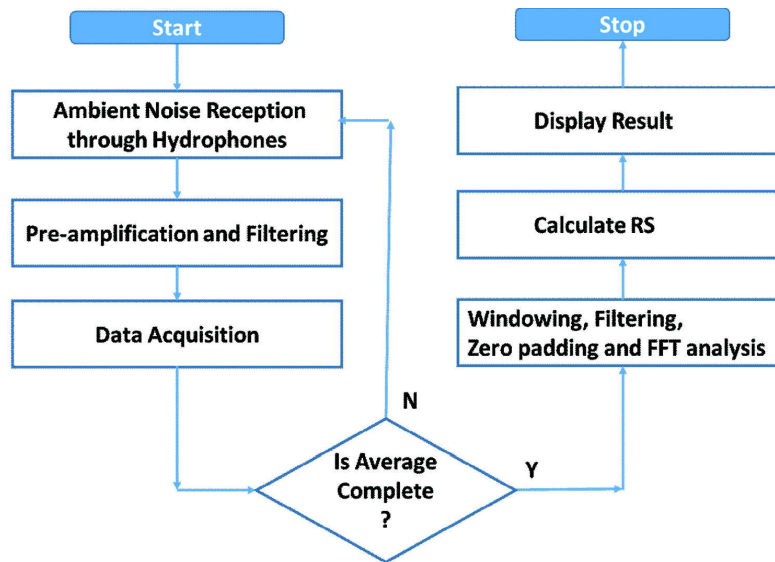
Fig. 12. Flowchart of Low-frequency measurement from 10 Hz to 100Hz

11. VALIDATION OF MEASUREMENTS

Receiving sensitivity of test hydrophone measured using current technology is given in Figure 13. Coherence, nearly equal to unity is a good indication of high SNR. The measured value of test hydrophone gives good agreement with OEM calibrated sensitivity.
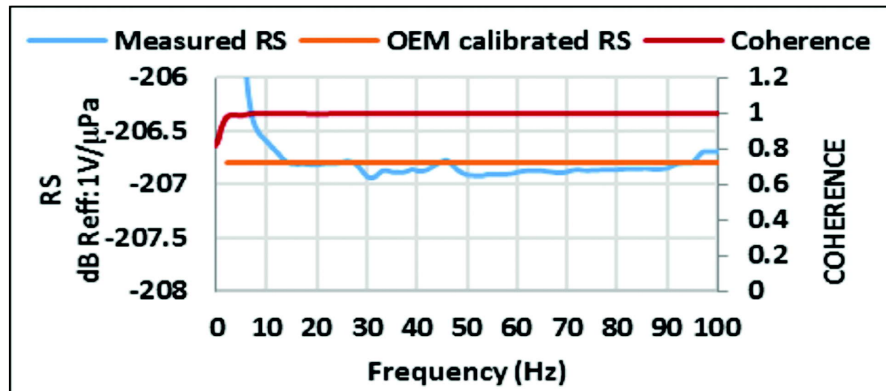

Fig. 13. Receiving Sensitivity and coherence

12. UNCERTAINTY ANALYSIS

Type A and Type B uncertainties are calculated from repeated measurements, calibration chart of standard hydrophone and instrument data sheets. Expanded uncertainty with coverage factor 2 is +/- 1.2 dB[8-10].

13. SUMMARY

Two measurement methods for low-frequency receiving sensitivity in a small acoustic tank are presented in this paper. First one is for the low-frequency measurement at frequencies higher than 100 Hz. The second method is for the frequency band of 10 Hz -100 Hz. Poor SNR is the critical constraint in both the measurement

methods. In the first method is improved by improving the coherence between standard and test hydrophones using simultaneous acquisition and other signal processing techniques. The second method uses high ambient noise as a signal and evaluates the hydrophone using noise correlation technique. The noise floor of the data acquisition system and proper positioning of the hydrophones are critical for controlling the SNR in the second method. Minimum detection level of the data acquisition system is very much important in both methods especially in 10 Hz to 100 Hz measurement. Both the methods are validated by comparing the results with calibrated values.

14. ACKNOWLEDGEMENTS

15. REFERENCES

[1]   Jin Xiaofeng and Yuan Wenjun, 1998. Transient calibration of underwater acoustic transducers. *J. Meas. Sci. Technol*. **9**, 1847-1851

[2]   IEC 60565: 2007. Underwater Acoustics. Hydrophones calibration in the frequency range 0.01 Hz to 1 MHz.

[3]   ANSI/ASA S1.20-2012 - Procedures for Calibration of underwater electroacoustic transducers

[4]   Van Buren A.L. and J.E. Blue, 1990. Calibration of underwater transducers at NRL/USRD. *Proc. Int. Workshop (Toulon, France)* June 12-13 1990 *(Berlin: Springer)*, pp. 221-41.

[5]   Robert J. Bobber, 1990. Underwater Electro Acoustic Measurements. *Peninsula publications*, ISBN 10:0932146198.

[6]   Linthish P. and R. Krishnakumar, 2016. LabVIEW Based Underwater Transducer Measurement Techniques. *Proc. International Symposium on Acoustics & Engineering Applications (NSA, India)*.

[7]   Gary Hayman, Graham Wells, Philip Boys and Clive Chambers, 2007. Free-field calibration of hydrophones at frequencies from 250 Hz to 1 kHz. NPL report DQL-AC 019.

[8]   Guide to the evaluation of measurement uncertainty for quantitative test results, Euro lab technical report No: 1/2006.

[9]   Stephanie Bell, 2001. A beginner's guide to the uncertainty of measurement. Measurement good practice guide no:11, National Physical Laboratory, UK ISSN1368-6550.

[10]   John R. Taylor, 1996. An introduction to error analysis. The study of uncertainties' in physical measurements. 2nd *Ed. University Science Books*. ISBN 0-935702-42

[11]   LabVIEW user manual 2013.

A computationally efficient implementation of adaptive beam forming in deep ocean scenario using circular array

Pratik Jain[1] and M. Rema Devi[2]
[1]Centre for High Energy Systems and Sciences, Hyderabad, India
[2]Naval Physical and Oceanographic Laboratory, Thrikkakara, Kochi, India
pjr23423@gmail.com

ABSTRACT

In this paper, the problem of direction of arrival estimation of unknown sources in deep water scenario, using a computationally efficient scheme of MVDR beam forming is investigated. The scheme is based on MVDR, a popular spatial filtering technique in array processing, which provides better resolution of targets, yet is computationally intensive, especially in the case of larger arrays. The target data as received by a circular array of acoustic sensors is simulated and adaptive beam forming is achieved using an efficient scheme, where the correlation matrix formation is optimized leading to high computational and memory gains. This algorithm is realized in an Intel i7 based board achieving real time performance with a single board, while catering to high input data rates.

1. INTRODUCTION

Estimating the direction-of-arrival (DOA) of propagating waves is an active research area in undersea warfare and peacetime naval applications. Source localization of underwater targets is a difficult task due to the complex and time varying dynamics of ocean medium. Multiple sensors distributed in space, spatially samples the signal received from the source, is generally used for target detection.

Beam forming[1] is employed on the array output for the estimation of target bearing. MVDR is the optimum beam former which gives narrow beam width and hence better discrimination even in the presence of strong interferences when the signal to noise ratio is in general not very low. The beam former weights are computed adaptively, which entails computation of the inverse of auto covariance matrix of the received data. Hence this method is computationally intensive, especially in the broad band case, for large arrays, due to the huge size of the matrix to be inverted. Memory and computational resources poses a challenge in real time implementation. This work focuses on the realization of a computationally efficient MVDR scheme. This method is suitable for deep water scenario, where the submarines generally operate, predominantly in passive reception mode.

2. DATA MODELS

Passive Acoustic source localization is the process of finding location of acoustic sources from the direction

of arrival of noise produced by them. A circular array with element spacing $\lambda/2$, is used for spatial sampling of the data, where λ is the wavelength corresponding to the highest frequency of interest. The array configuration is shown in Figure 1.
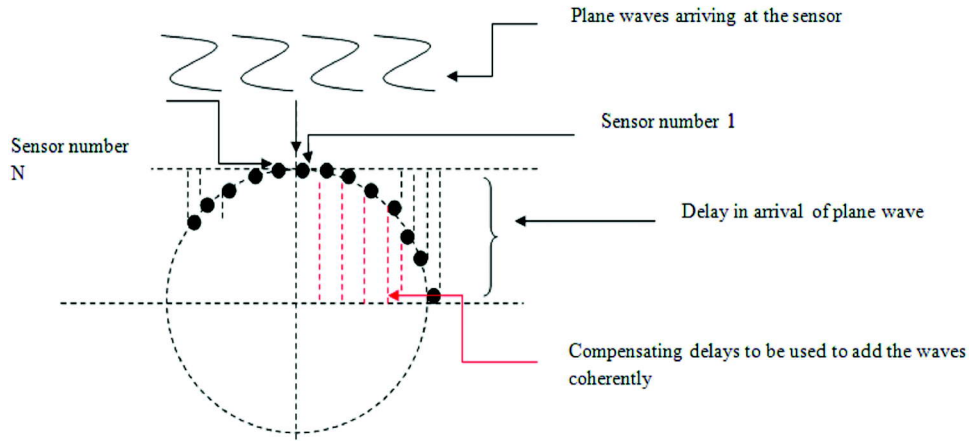

Fig. 1. Geometry of Circular array

Parameter	Specification
Array geometry	A uniform circular array with N sensors spaced (N/360) degrees apart.
Number of sensors to be used for forming a single beam	M sensors ($M \approx N/3$)
Radius of the array	R meters
Sampling frequency	fs

The delay in arrival of the plane wave is:

$$\text{Delay (n)} = R\,(1- \cos(n*\theta))/c; \quad n= 1 \text{ to } M/2 \tag{1}$$

Where, n is the sensor no. which is assumed an even number

R = radius of the array;

θ : Angle subtended between adjacent sensors

c = speed of sound in water

The delays will be symmetric on either side of the centre. The compensating delays to add the signals in phase are obtained by subtracting the maximum of the actual delays from the individual delays at the respective sensors.

The received signal at the sensor array at time t can be expressed as an N × 1 vector $f(t)$ of the form [2]

$$f(t) = A\eta(t) + w(t) \tag{2}$$

Where A, $\eta(x)$, $w(t)$ are given by

$$A = [a(\theta_1)a(\theta_2)\,.....a(\theta_j)] \tag{3}$$

$a(\theta_j)$ is the steering vector corresponding to the source direction θ_j.

$$a(\theta_j) = [1, e^{i\omega\tau1},..., e^{i\omega\tau M-1}]^T \tag{4}$$

Where τ_i is the propagation delay and ω is the angular frequency of the source signal.

$$\eta(t) = [\eta_1(t),\ \eta_2(t),\ ...,\ \eta_j(t)] \tag{5}$$

where $\eta_j(t)$ is the slowly varying complex amplitude of the signal from the jth source at time t, modelled as jointly stationary and uncorrelated circular complex narrowband Gaussian random processes with mean zero and variance, $\sigma_j^2 = E\left[\left|\eta_j(t)\right|^2\right]$.

$$w(t) = [w_1(t), w_2(t), ..., w_k(t)] \tag{6}$$

Where $w_1(t), w_2(t), ..., w_k(t)$ are noise corresponding to the sea state 4 of the wenz curve[2] shown in Figure 2.

The deep sea noise is mainly caused by natural sources, such as surface noise, molecular motion, storms, seismic activity *etc.* and also artificial manmade sources such as distance shipping, turbulence etc. The average representative ambient noise spectra[2] for different conditions are shown in Figure 2 for different conditions of shipping and wind speeds[2].
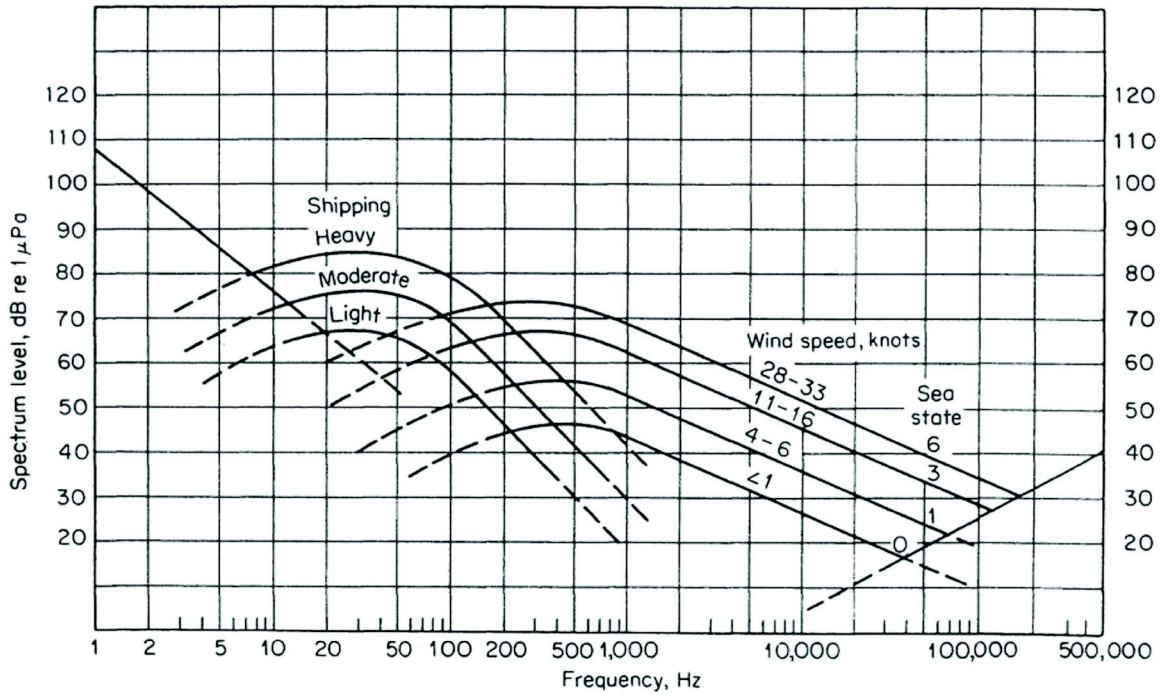

Fig. 2. Ambient noise spectrum in deep sea adapted[2]

The spatial correlation matrix of the array data vector $f(t) \ \varepsilon \ C^{N \times N}$ is defined as[3]

$$R_N = E[f(t)f^H(t)] \tag{7}$$

In practical calculations, for finite data conditions, the correlation matrix can be estimated as follows

$$\hat{R}_N = \frac{1}{L}\sum_{t=1}^{L}f(t)f^H(t) \tag{8}$$

Where L is the number of snapshots.

3. SIMULATION AND IMPLEMENTATION OF MVDR ALGORITHM

3.1 MVDR algorithm for broadband signals

H beams are formed to cover the full panoramic range. MVDR is an adaptive beam former where the weights are adapted to changes in acoustic field, thus improving the detection performance in deep ocean

scenario. It is the optimum beam former which gives narrow beam width and hence better discrimination. The beam former weights are computed adaptively with a constraint of keeping the output power in a given direction to be unity while the power output in all other directions are minimized[3]. Weight computation is done for all the bins in the frequency bandwidth of B Hz. The beam power is computed for all bins and summed to find the beam power in one bearing.

The M sensors corresponding to an arc of 120 deg are combined to form a beam. The time series from the sensors are converted into frequency domain using FFT. The FFT length is decided by narrow band approximation criteria3. The cross-spectral density matrix (CSM), R_k corresponding to each frequency bin is computed in the frequency band of interest. The inverse of the CSM, $R_k{}^{-1}$ is used to compute the MVDR weights using (9).

The MVDR weight is computed[4] as :

$$W_k(\theta) = \frac{R_k^{-1} S_K(\theta)}{S_k(\theta)^H R_k^{-1} S_k(\theta)} \tag{9}$$

where θ- the steering direction, k - frequency bin, $S_k(\theta)$, the steering vector

$$S_k(\theta) = \left\{ e^{(j\omega\tau_i)} \right\}_{i \to 0:M-1}, \ \tau_i \text{ is the time delay vector for the } i^{th} \text{ sensor}$$

R_k- cross spectral density matrix of the array snapshot for k^{th} frequency bin.

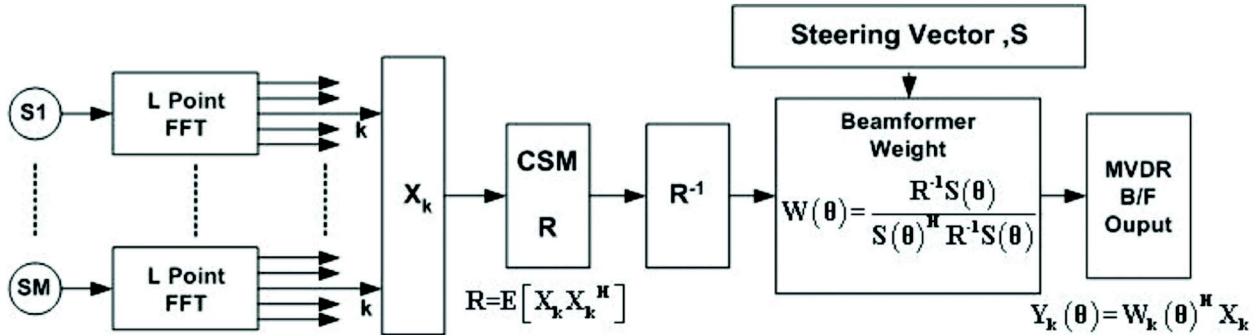$$R_k = E\left\{ x_k x_k{}^H \right\} \tag{10}$$

Fig. 3. Broadband frequency domain implementation of MVDR

MVDR is implementation requires two stages, in stage one we compute CSM and average it for integration time T[5]. Post integration the CSM is pushed to second stage was CSM inverse is computed and new MVDR weights are calculated.

4. RESULTS & DISCUSSIONS

4.1 Computational requirement for standard MVDR implementation

Let us take N sensor circular array, where M sensors are combined for beam forming; there will be N sectors each consisting of M sensor with M-1 sensors overlapped. Each sector and frequency bin combination will require one CSM matrix. There will be NxK matrices of size MxM. The cross spectral density matrix will be integrated over time for every snap shot. For a broadband beam former, this is to be done for all the frequency bins. Though matrix inversion is highly computationally demanding function, in this case the major computational and memory requirements comes from the formation of CSM R_{avg}, because it needs to be computed for every snapshot[6].

Let us take a circular array with following specifications

N	100
M	33
K	128
FFT size	256
T	1 sec
Snapshot	50 per sec
fs	12800 Hz

Function	Computational load	Memory requirement
R_{avg}	33 x 33 x 100 x 128 x 50 = 697 Mflops	33 x 33 x 100 x 128 x 2 =27MB
R_{avg}^{-1}	33 x 33 x 33 x 100 x 128 = 457 Mflops	33 x 33 x 100 x 128= 14MB

4.2 Computationally efficient implementation

In the MVDR implementation for N sectors, there are M-1 sensor overlaps across sectors. So instead of creating M x M CSM for N sectors, we create one N x N CSM for the entire array. Averaging across snapshots is done using this full matrix. Before computing inverse, we will extract N no. of M x M matrices from the bigger N x N matrix.

Function	Computational load	Memory requirement
R_{avg}(modified)	100 x 100 x 128 x 50 = 64 Mflops	100 x 100 x 128 x 2 =2.5MB
R_{avg}^{-1}	33 x 33 x 33 x 100 x 128 = 457 Mflops	33 x 33 x 100 x 128 = 14MB

There is about 56% reduction in computation and 59% reduction in memory requirements owing to this new scheme.

4.3 Implementation in hardware

A real time MVDR beam former for massive cylindrical array was implemented in a single COTs board based on Intel i7. The noisy data simulated for array hydrophone signals were converted to Digital format and broadcasted over Ethernet network. The application running in Intel i7 based board receive data over Gigabit Ethernet and compute the MVDR output for under water target detection and bearing estimation. The MVDR processing program is written in C and optimized using Intel's IPP and MKL libraries. This program is split in three parallel threads, all working simultaneously. The result corresponding to direction of arrival estimation of two targets at 40 & 47 deg in azimuth, for sea state 4, is shown in Figure 4. For data rates of 800Mbps, new data is coming as a burst every 8 m/s. It takes 3ms for R matrix computation and 1.2 ms for beamforming.

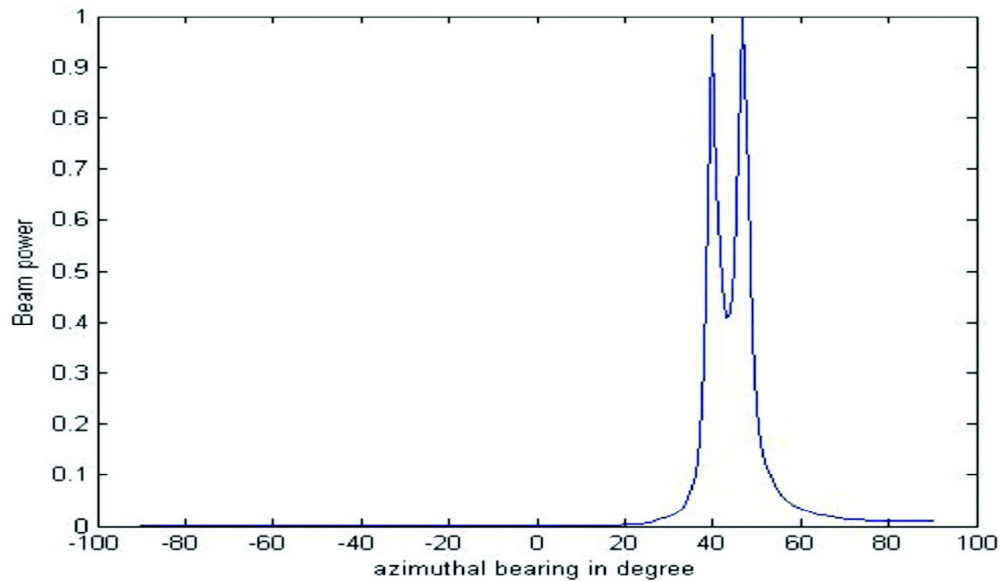|	
Processing Platform	Intel i7 based SBC
Operating System	Ubuntu 16.04 64bit
Programing Language	C
Integrated Development Environment	Eclipse Mars 2
Intel Libraries	MKL, IPP
Compiler	Intel C / GCC
Threads	P thread
Communication protocol	UDP Socket

Fig. 4. Estimated DOAs using MVDR beam former for targets at 40° & 47°

5. CONCLUSION

We examined the problem of direction of arrival estimation of unknown sources in deep water scenario, using a computationally efficient scheme of adaptive beam forming. The scheme is based on MVDR, which provides better resolution of targets, but is computationally intensive, especially in the case of larger arrays. The target data as received by a circular array of acoustic sensors was simulated. The MVDR realization scheme is improvised to bring in a large reduction in computational and memory requirements. The scheme was realized and tested in Intel i7 based COTs board and real time performance was achieved. Demonstrated the DOA estimation of two targets in deep water scenario using the method.

6. REFERENCES

[1]   Barry D. Van Veen and Kevin M. Buckley, 1998. Beamforming: A versatile approach to spatial filtering, *IEEE ASSCP Magazine* April 1998.

[2]   R.J. Urick, 1983. Principles of Underwater Sound. *McGraw-Hill, Inc.*, 3rd Edition.

[3]   Harry L. Van Trees, 2002. Optimum Array Processing, John Wiley & Sons Inc.

[4]   Priyabratha Sinha, Alan D. George and Keonwook Kim. 2002. Parallel algorithm for Robust Broadband MVDR beamforming. J. Computational Acoustics, 10 (1), 69-96.

[5]   Chao Pan and Jingdong Chen, 2015. A multistage minimum variance distortion less response beamformer for noise reduction. *J. Acoust. Soc. America,* **137**(3), 1377-1388

[6]   S.M. Kogon, 2004. Eigenvectors, diagonal loading and white noise gain constraints for robust adaptive beamforming. *In Proc. the Thirty-Seventh Asilomar Conference on Signals,* Systems and Computers, **2**, 1853-1857

[7]   H.O. Bugge, 2009. An evaluation of Intel's core i7 architecture using a comparative approach Comp. *Sci. Res. Dev.* **23**, 203. https://doi.org/10.1007/s00450-009-0076-6

[8]   Current Intel® Product Information http://ark.intel.com

[9]   Intel Developers Centershttp://developer.intel.com/design/index.htm

Improved active sonar detection technique for fast fading channels

Thasneem E.S.[1], Sinchu P.[2] and Meena V.[3]
[1]Signal Processing, Rajagiri School of Engineering and technology
[2]Naval Physical and Oceanographic Laboratory
[3]Rajagiri School of Engineering and technology
thasneem66@gmail.com

ABSTRACT

Detection of target in underwater environment is a very challenging task due to reverberation and fast fading nature of the channel. In this paper, a new detection technique viz. segmented replica correlation using Fractional Fourier transform (FrFT) is introduced. We compare the results of different detection techniques such as replica correlation using Fast Fourier Transform (FFT), replica correlation using FrFT, Segmented replica correlation using FFT and Segmented replica correlation using FrFT. These detection techniques were tested with both simulated data and real data. It has been observed that RC using FrFT performs the best in an ideal channel and SRC using FrFT performs the best in fast fading channel.

1. INTRODUCTION

In the simplest active sonar system, an acoustic pulse of short duration of the order of a few milliseconds is transmitted. When the acoustic waves hit the target, a part of the total energy of the transmitted wave will be reflected back as echo. The echo is then processed to get the parameters of the target like range, bearing and Doppler of the target[3]. The transmitted signal can be a continuous wave (CW) or a linear frequency modulated signal (LFM)[4]. The method of detection most commonly used in active sonar is matched filtering[4]. The digital equivalent of this matched filtering is called replica correlation (RC)[5]. RC can be implemented by using Fast Fourier transform (FFT) in order to reduce the computational complexity. This type of detector is known as heterodyne correlator[4].

When the transmission channel is an ideal channel *i.e.* the signal is only affected by the Gaussian noise, RC using FFT provides better detection. However, when the transmitted channel is not an ideal channel, then signal fading occurs. In the case of fast fading channel, segmented RC gives better performance.

Non-stationary signals like LFM, have the same behavior as chirp signals. Hence, a transform with chirp as basis can give better performance than FFT. Chirps are signals which exhibit a change in frequency with time. Fractional Fourier transform (FrFT) is a time frequency method (TFM)[6]. So for non-stationary signals we propose for RC using FrFT. In order to combat fading effects in non-stationary signals at lower SNR we propose SRC using FrFT.

The following sections of this paper are described as follows. In section 2, an overview of the Fractional Fourier transform is given. In section 3, the detection techniques discussed above are studied and analyzed. These were evaluated in both ideal and fading channel for the synthetic data. A real echo data was also analyzed by using these detection techniques. In section 4, results and discussions based on both synthetic and real data is given. And in section 5, results are concluded.

2. OVERVIEW OF FRACTIONAL FOURIER TRANSFORM

FrFT is the generalization of ordinary Fourier transform. It is a time frequency distribution with an order parameter α. This order parameter α provides an additional degree of freedom to FrFT compared to classical Fourier transform which results in improvement of performance with non-stationary signals. Choice of α = 1 results in classical Fourier transform and α = -1 results in inverse Fourier transform. All the properties of FFT are merely special cases of properties of FrFT[7][9].

α^{th} order fractional Fourier transform of a function $f(x)$ can be mathematically described as follows[9].

$$F_\alpha[f(x)] = \int_{-\infty}^{\infty} B_\alpha(x,x')f(x')dx' \tag{1}$$

$$B_\alpha(x,x') = A_\varnothing \exp[i\pi(x^2 \cot\varnothing - 2xx'\csc\varnothing + x'^2 \cot\varnothing]f(x')dx' \tag{2}$$

$$A_\varnothing = \frac{\exp\dfrac{-i\pi\,\mathrm{sgn}(\sin\varnothing)}{4} + \dfrac{i\varnothing}{2}}{\left|\sin\varnothing\right|^{\frac{1}{2}}} \tag{3}$$

Where, $\varnothing = \alpha\pi / 2$ and $0 < |\alpha| < 2$

Therefore, FrFT computation can be carried out in a sequence of steps. The equation consists of four parts: a multiplication by a chirp in one domain followed by a Fourier transform, then multiplication by a chirp in the transform domain and finally a complex scaling. Chirps therefore form the basis functions in this transform. They appear as inclined lines in the T-F plane. So, FrFT can be used where chirp's signals are involved. Ozaktas *et al*.[7] has introduced a discrete implementation of FrFT that computes FrFT in O (Nlog(N)) with similar complexity as Cooley-Turkeys FFT. Hence FrFT can be done with no additional cost.

3. DETECTION TECHNIQUES

3.1 Replica correlation using FFT

The digital equivalent of matched filter operation is known as Replica Correlation (RC). Here overlapping segments of the received signal is cross correlated with time compressed replicas of the transmitted pulse which are stored as references. The references are known as replicas and hence the name replica correlation. The correlation points that correspond to maximum value are given to a threshold detector. The number of computations involved in direct correlation method for wide band signals is large. Hence we go for FFT based fast implementation technique using narrow band assumption proposed by Glisson *et al*.[4][5].

If $s(n)$ is the received signal and $r_l*(n)$ is the time compressed replica of the transmitted, here * represents complex conjugate. Then the operation of RC can be mathematically stated as follows[6].

$$Y(p,l) = \frac{1}{N} \sum_{k=0}^{N-1} s(k+p)r_l*(k)p = 0,1 \tag{4}$$

Replicas are stored in such a way that it covers the entire range of Doppler that a target can possess. Here l denotes which replica and N is the length of replica. Length of each replica stored as the reference is same as that of the transmitted pulse and moving lag window in (4) has the same length as that of replica. p denotes the different time delays and can vary from zero to length of the received signal.

The operation described in (4) can be done by N-point DFT as follows[5].

$$Y(p,l) = DFT\{s(k+p)r_l*(k)\} k = 0,1 \ldots N-1 \qquad (5)$$

The discrete Fourier transform (DFT) operation in (5) is done by using FFT for each window and the maximum value in each window contributes the output of RC. Block diagram of RC is given in Figure 1.
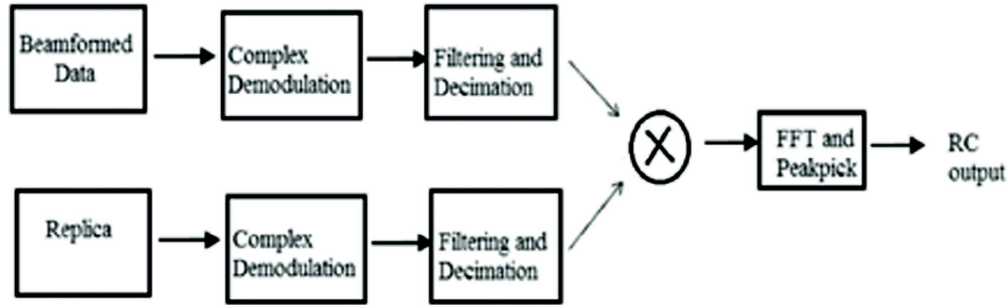

Fig. 1. Block diagram of RC using FFT

The received signal usually has a center frequency which is several times higher than the bandwidth, *i.e.,* the signal is a narrow band signal. The signal is base-band converted by performing complex demodulation followed by low pass filtering and decimation. Filtering operation removes all spectral components outside the band of analysis[6]. These operations are done both on stored references and the received signal.

3.2 Segmented Replica correlation using FFT

Fast fading distortion can occur as a result of the nature of transmitted channel i.e., underwater environment. The multiple propagation paths in the transmitted channel causes the coherence time of the channel to be less than the pulse duration of the signal. Thus, the signal gets distorted and deteriorates RC performance. Quan *et al.*[1] proposes a segmentation of the received signal before performing RC. This is technique is termed segmented RC (SRC). SRC can be implemented by performing FFT on segments of the windowed received signal. As in (5) the received signal s(n) is windowed and multiplied with conjugate of the replica $r_l*(n)$ and then FFT is performed on the resultant by dividing it in to M segments. Let the sampling frequency be f_s and $N = Tf_s$ be the total number of samples in the replica. Then SRC is given as follows[6],[2].

$$Y(p,l) = \sum_{k=0}^{M-1} \sqrt{\frac{2M}{N}} \sum_{i=0}^{\left(\frac{N}{M}\right)-1} s(p+i+kN/M)r_l*(i+kNM) \qquad (6)$$

SRC can be implemented using FFT for reducing computational complexity as follows

$$Y(p,l) = \sum_{k=0}^{M-1} \left\{ DFT\left\{ s\left(p+i+\frac{kN}{M}\right)r_l*(i+kNM) \right\} \right\} \qquad (7)$$

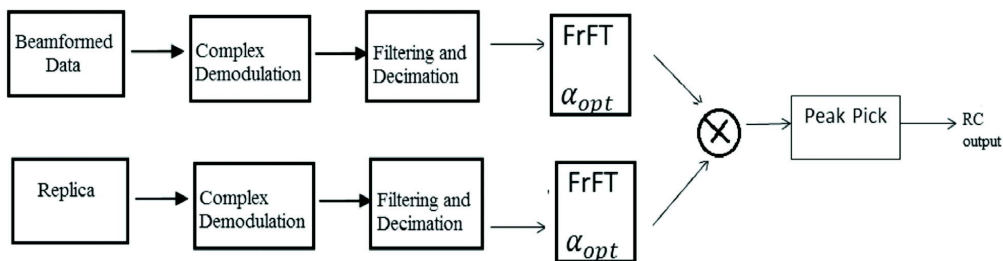where, $i = 0$ to $\left(\dfrac{N}{M}\right)-1$ and *p*=0, 1, ...

Fig. 2. Block diagram of RC using FrFT

3.3 Replica correlation using FrFT

Further improvement in detection performance in lower SNR can be achieved if we make use of FrFT instead of FFT in RC implementation. The basis function of FrFT are chirps[7]. Hence FrFT is a better choice when LFM signals are involved. The correlator receiver using FrFT in matched filtering is implemented as shown is Figure 2. FrFT of overlapping received signal data blocks is multiplied with FrFT of the replica signal. The peak of this process is then passed through the threshold detector to detect the target[3].

The optimum $\alpha(\alpha_{opt})$ used is pre-computed as follows, where α is the chirp rate of the transmitted signal and is given by

$$\alpha = \frac{band\ width}{2 * pulse\ width} \tag{8}$$

$$\alpha_{opt} = \frac{2}{\pi}\tan^{-1}\left\{\frac{\frac{f_s^2}{N}}{2\alpha}\right\} \tag{9}$$

Here N is the number of samples in the replica. RC using FrFT can be summarized as follows

$$Y(p,l) = \left\{F_{\alpha_{opt}}[s(k+p)]F_{\alpha_{opt}}[r_l * (k)]\right\} \tag{10}$$

where, $F_{\alpha_{opt}}$ is the FrFT for optimum alpha and k = 0,1.... N-1 and p=0,1.....

3.4 Segmented Replica correlation using FrFT

If the channel used for transmission is not an ideal channel, then it may result in distortion of the transmitted signal. Hence we propose segmentation in FrFT domain also. This may improve the detection performance of LFM signals. Here, we compute the FrFT of segments of the windowed received signal and also the FrFT of M subdivided segments of the replica and multiply these two and sum up over M segments. Then peak value is taken. The above described SRC can be implemented by using FrFT as follows

$$Y(p,l) = \sum_{k=0}^{(M)-1}\left\{F_{\alpha_{opt}}[s(p+i+kN\ /\ M)]F_{\alpha_{opt}}[r_l * kNM)]\right\} \tag{11}$$

where, i = 0,1,.....(N/M)-1 and p = 0,1,2....

4. RESULTS AND DISCUSSION

4.1 Simulation Setup

Computer simulations are done in Matlab 2013. For generating simulated data, an LFM signal with pulse width of 240 ms is created and Gaussian noise is added to it to bring the effect of ideal channel on the LFM signal. The LFM signal under consideration has a center frequency of 2000 Hz, bandwidth of 300 Hz and pulse width of 240 ms. A sampling frequency of 12000 Hz is assumed throughout the simulation. For performing RC on the received signal five references were stored corresponding to the following relative speeds of the target: 5 knots (kn), 10 kn, 0 kn, -5 kn and -10 kn. In order to simulate fading effect, the LFM signal is passed through rician channel. The parameters of rician channel were varied in such a way that there are three multi paths. Delays and attenuation for each path was also defined.

4.2 Results

In this paper we have considered two detection techniques, RC using FFT and RC using FrFT. These were tested on the simulated data. The output of RC with the maximum peak gives the range and Doppler of the target. The output of RC detectors for SNR= -10 dB using FFT and FrFT are shown in Figure 3. The output of both the detection techniques are normalized and compared in terms of SNR.
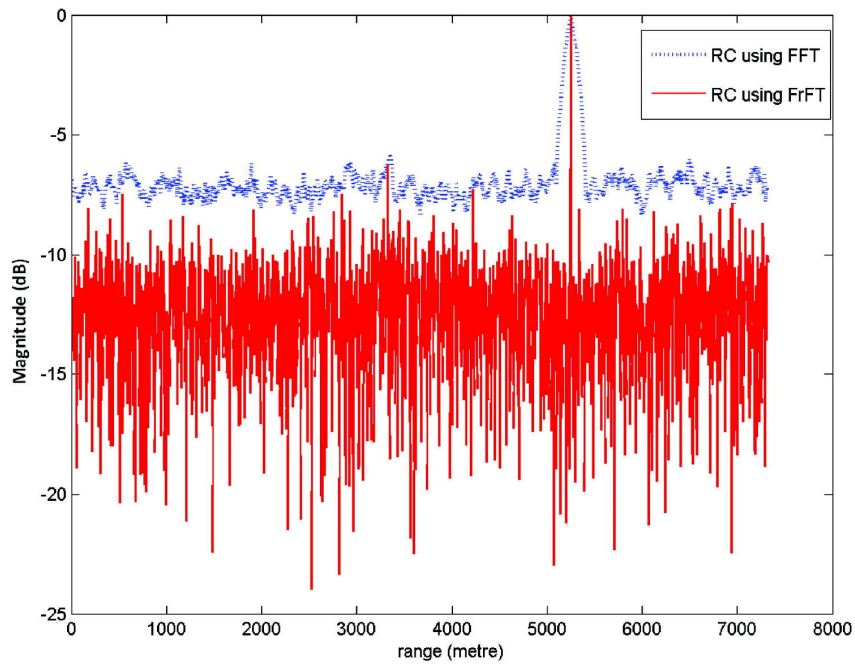
Fig. 3. RC Output

We can see from Figure 3 that there is a better detection of the order of 3 dB for RC using FrFT than RC using FFT by looking at the noise levels. The performance of these two detection techniques was analyzed using Receiver Operating Characteristic (ROC) curves. ROC curves probability of detection (Pd) versus probability of false alarm (Pfa) plots of a detector. The area under these curves is a measure of the performance of a detector[8].
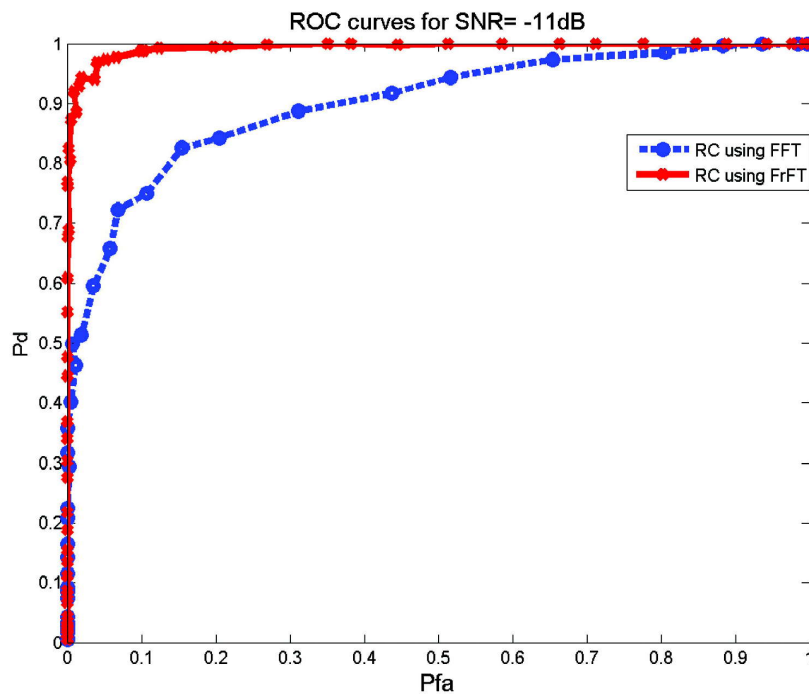

Fig. 4. ROC curves

ROC curves are shown in Figure 4 from which it is clear that the area under RC using FrFT is greater than area under RC using FFT. Number of segments in SRC is taken in such a way that duration of each segment is less than or equal channel coherence time[2][1]. The performance of each detection technique is shown in Figure 5. SRC using FrFT performs better than all other detection techniques. This is evident from background noise level. RC using FFT and RC using FrFT were also tested on field data and the result is as in Figure 6.
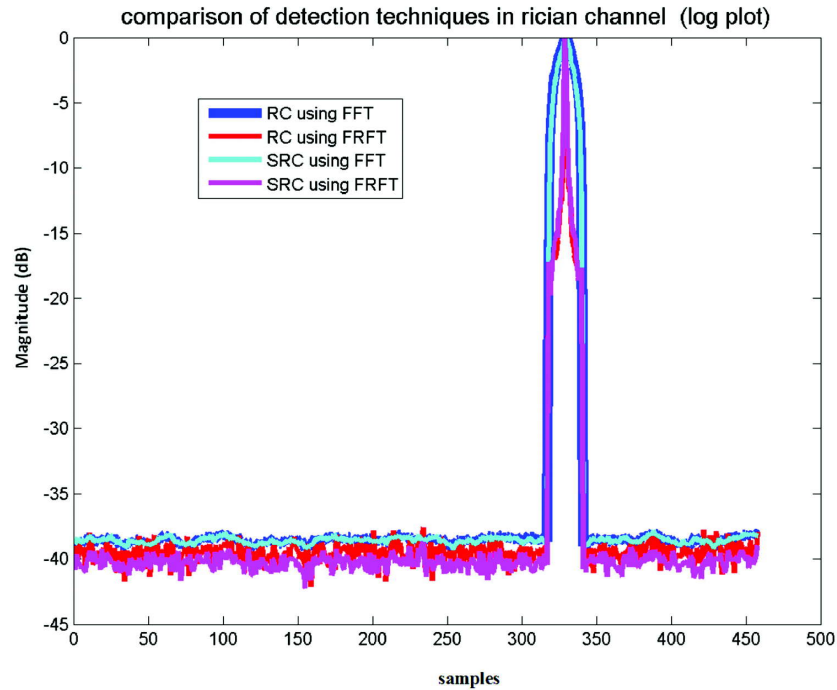
Fig. 5. Comparison of different detection techniques on fast fading
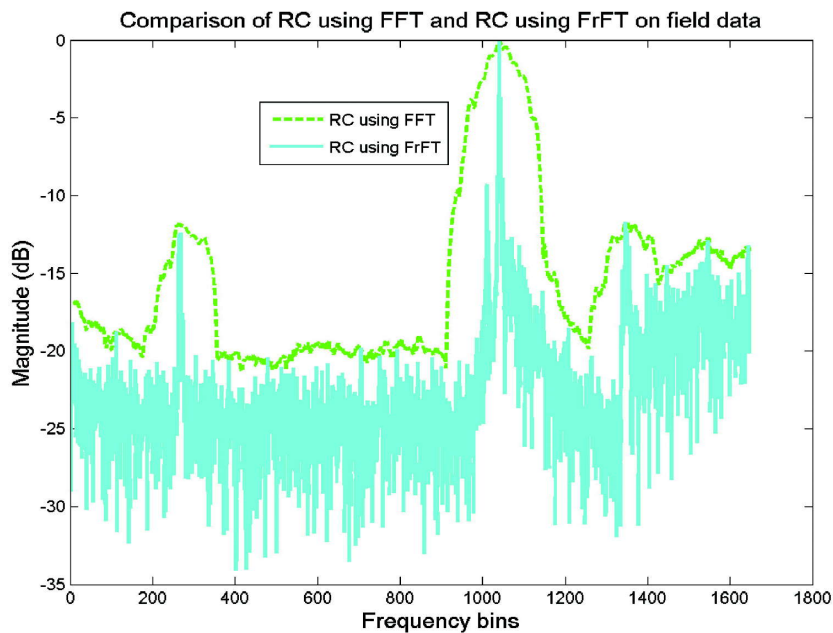
Fig. 6. Comparison of RC using FFT and RC using FRFFT on field echo

From Figure 6, it is clear that there is an improvement of 3 dB for RC using FrFT than RC using FFT. All these detection techniques were evaluated on field data also. As shown in Figure 7, RC using FrFT performs better than all other detection techniques.
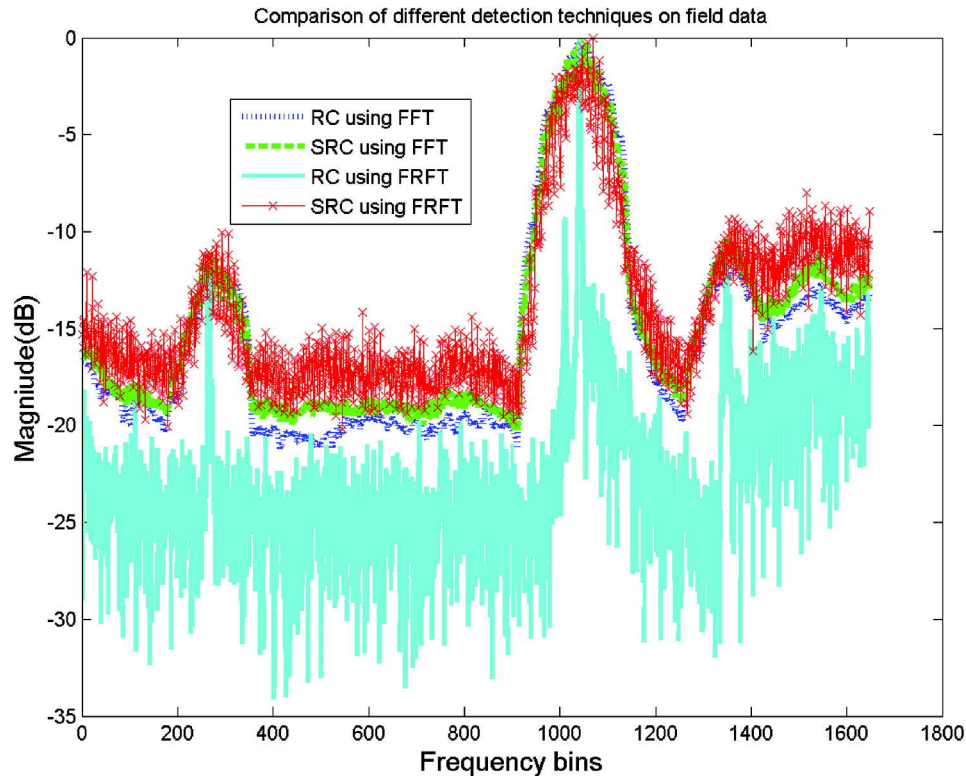

Fig. 7. Comparison of different detection techniques on field data

5. CONCLUSION

In this paper, a novel detection technique which uses segmented RC along with FrFT is proposed. The performance of various detection techniques was analysed. Better performance is observed when FrFT is used to implemented RC and SRC instead of FFT. RC using FrFT provides 3 dB improvement in detection compared to RC using FFT in ideal channel. And SRC using FrFT performs better than all other detectors in fast fading channel. Fractional Fourier transform can be used as a basic tool for detection techniques in active sonar in places where we use classical Fourier transform.

6. ACKNOWLEDGEMENT

We would like to thank the Director, Naval Physical and Oceanographic Laboratory (NPOL) for giving us the opportunity to carry out the project at NPOL. We also thank Mr. Unnikrishnan N, scientist 'C', NPOL for the guidance towards completing the work.

7. REFERENCES

[1]   Z. Quan, Z. Liu, L. Luo and G. Hu, 2015. Detection Performance and Robustness of Segmented Replica Correlator Processors in Fast Fading Distortion Channels, in 12th International Conference on Fuzzy Systems and Knowledge Discovery.

[2]   S. Stergiopoulos, 2000. Advanced Signal Processing Handbook: Theory and Implementation for Radar, Sonar and Medical Imaging Real-Time Systems, CRC Press, 2nd ed., pp. 728-735.

[3]   Roshan Jacob, 2010. Development of Time-Frequency Techniques for Sonar Applications, Ph.D. dissertation. *Naval Physical and Oceanographic Laboratory,* pp. 179.

[4]   T.H. Glisson, C. Black, and A.P. Sage, 1970. On sonar signal analysis,*IEEE Trans. Aerospace and Electronic Systems,* **6**(1), 37-49.

[5]   T.H. Glisson, C.I. Black and A.P. Sage, 1969. On digital replica correlation algorithms with application to active sonar, *IEEE Tr. Audio Electroacoustics,* **17**(1), 190-197.

[6]   P.M. Baggenstoss, 1994. On detecting linear frequency-modulated waveforms in frequency-and time-dispersive channels: Alternatives to segmented replica correlation, *IEEE J. Oceanic Engineering,* **19**(4), 591-598.

[7]   H. Ozaktas, O. Arikan, A. Kutay and G. Bozdagi, 1996. Digital Computation of the Fractional Fourier Transform, *IEEE Tr. on Signal Processing,* **44**(9), 2141-2150.

[8]   S.M. Kay, 2008. Fundamentals of Statistical Signal Processing: Estimation theory, PTR Prentice-Hall.

[9]   H. Ozaktas, Zeev Zalevsky and A. Kutay, 2001. FrFT with applications in optics and signal processing (John Wiley and Sons).

INFORMATION FOR AUTHORS

ARTICLES

The Journal of Acoustical Society of India (JASI) is a refereed publication published quarterly by the Acoustical Society of India (ASI). JASI includes refereed articles, technical notes, letters-to-the-editor, book review and announcements of general interest to readers.

Articles may be theoretical or experimental in nature. But those which combine theoretical and experimental approaches to solve acoustics problems are particularly welcome. Technical notes, letters-to-the-editor and announcements may also be submitted. Articles must not have been published previously in other engineering or scientific journals. Articles in the following are particularly encouraged: applied acoustics, acoustical materials, active noise & vibration control, bioacoustics, communication acoustics including speech, computational acoustics, electro-acoustics and audio engineering, environmental acoustics, musical acoustics, non-linear acoustics, noise, physical acoustics, physiological and psychological acoustics, quieter technologies, room and building acoustics, structural acoustics and vibration, ultrasonics, underwater acoustics.

Authors whose articles are accepted for publication must transfer copyright of their articles to the ASI. This transfer involves publication only and does not in any way alter the author's traditional right regarding his/her articles.

PREPARATION OF MANUSCRIPTS

All manuscripts are refereed by at least two referees and are reviewed by the Publication Committee (all editors) before acceptance. Manuscripts of articles and technical notes should be submitted for review electronically to the Chief Editor by e-mail or by express mail on a disc. JASI maintains a high standard in the reviewing process and only accept papers of high quality. On acceptance, revised articles of all authors should be submitted to the Chief Editor by e-mail or by express mail.

Text of the manuscript should be double-spaced on A4 size paper, subdivided by main headings-typed in upper and lower case flush centre, with one line of space above and below and sub-headings within a section-typed in upper and lower case understood, flush left, followed by a period. Sub-sub headings should be italic. Articles should be written so that readers in different fields of acoustics can understand them easily. Manuscripts are only published if not normally exceeding twenty double-spaced text pages. If figures and illustrations are included then normally they should be restricted to no more than twelve-fifteen.

The first page of manuscripts should include on separate lines, the title of article, the names, of authors, affiliations and mailing addresses of authors in upper and lowers case. Do not include the author's title, position or degrees. Give an adequate post office address including pin or other postal code and the name of the city. An abstract of not more than 200 words should be included with each article. References should be numbered consecutively throughout the article with the number appearing as a superscript at the end of the sentence unless such placement causes ambiguity. The references should be grouped together, double spaced at the end of the article on a separate page. Footnotes are discouraged. Abbreviations and special terms must be defined if used.

EQUATIONS

Mathematical expressions should be typewritten as completely as possible. Equation should be numbered consecutively throughout the body of the article at the right hand margin in parentheses. Use letters and numbers for any equations in an appendix: Appendix A: (A1, (A2), etc. Equation numbers in the running text should be enclosed in parentheses, i.e., Eq. (1), Eqs. (1a) and (2a). Figures should be referred to as Fig. 1, Fig. 2, etc. Reference to table is in full: Table 1, Table 2, etc. Metric units should be used: the preferred from of metric unit is the System International (SI).

REFERENCES

The order and style of information differs slightly between periodical and book references and between published and unpublished references, depending on the available publication entries. A few examples are shown below.

Periodicals:
[1]   S.R. Pride and M.W. Haartsen, 1996. Electroseismic wave properties, *J. Acoust. Soc. Am.*, **100** (3), 1301-1315.
[2]   S.-H. Kim and I. Lee, 1996. Aeroelastic analysis of a flexible airfoil with free play non-linearity, *J. Sound Vib.*, **193** (4), 823-846.

Books:
[1]   E.S. Skudzryk, 1968. *Simple and Comlex Vibratory Systems*, the Pennsylvania State University Press, London.
[2]   E.H. Dowell, 1975. *Aeroelasticity of plates and shells*, Nordhoff, Leyden.

Others:
[1]   J.N. Yang and A. Akbarpour, 1987. Technical Report NCEER-87-0007, Instantaneous Optimal Control Law For Tall Buildings Under Seismic Excitations.

SUMISSIONS

All materials from authors should be submitted in electronic form to the JASI Chief Editor: B. Chakraborty, CSIR - National Institute of Oceanography, Dona Paula, Goa-403 004, Tel: +91.832.2450.318, Fax: +91.832.2450.602,(e-mail: bishwajit@nio.org) For the item to be published in a given issue of a journal, the manuscript must reach the Chief Editor at least twelve week before the publication date.

SUMISSION OF ACCEPTED MANUSCRIPT

On acceptance, revised articles should be submitted in electronic form to the JASI Chief Editor (bishwajit@nio.org)